DEVELOPMENT OF AN OPTIMAL DRAGONFLY-LIKE FLAPPING WING STRUCTURE FOR USE IN BIOMIMETIC MICRO AIR VEHICLES

PRAVEENA NAIR SIVASANKARAN

THESIS SUBMITTED IN FULFILMENT OF THE REQUIREMENTS FOR THE DEGREE OF DOCTOR OF PHILOSOPHY

FACULTY OF ENGINEERING

UNIVERSITY OF MALAYA

KUALA LUMPUR

2015

UNIVERSITY OF MALAYA

ORIGINAL LITERARY WORK DECLARATION

Name of Candidate: (I.C/Passport No:)

Registration/Matric No:

Name of Degree:

Title of Project Paper/Research Report/Dissertation/Thesis ("this Work"):

Field of Study:

I do solemnly and sincerely declare that:

(1) I am the sole author/writer of this Work;
(2) This Work is original;
(3) Any use of any work in which copyright exists was done by way of fair dealing and for permitted purposes and any excerpt or extract from, or reference to or reproduction of any copyright work has been disclosed expressly and sufficiently and the title of the Work and its authorship have been acknowledged in this Work;
(4) I do not have any actual knowledge nor do I ought reasonably to know that the making of this work constitutes an infringement of any copyright work;
(5) I hereby assign all and every rights in the copyright to this Work to the University of Malaya ("UM"), who henceforth shall be owner of the copyright in this Work and that any reproduction or use in any form or by any means whatsoever is prohibited without the written consent of UM having been first had and obtained;
(6) I am fully aware that if in the course of making this Work I have infringed any copyright whether intentionally or otherwise, I may be subject to legal action or any other action as may be determined by UM.

Candidate's Signature Date:

Subscribed and solemnly declared before,

Witness's Signature Date:

Name:

Designation:

ABSTRACT

Biomimetic Micro Air Vehicles (BMAV) are unmanned, micro-scaled aircrafts that are bioinspired from flying organisms to achieve lift and thrust by flapping their wings. Micro Air Vehicles (MAV) are a relatively new and rapidly growing area of aerospace research. They were first defined by the US Defense Advanced Research Projects Agency (DARPA) in 1997 as unmanned aircraft that are less than 15 cm in any dimension. This allows BMAV to potentially be smaller and more lightweight than the other two types. These characteristics make BMAV ideally suited for flight missions in confined areas (e.g. around power lines, narrow streets, indoors, etc.). Therefore, BMAV structural components must be ultra-lightweight, compact, and flexible. Most past MAV research has focused on fixed wings, which are essentially scaled-down versions of wings on conventional fixed wing aircraft. These wings are unsuitable for BMAV due to their lack of flexibility. So a new type of structural wing design is required for BMAV. In this work, a dragonfly wing structure is mimicked to construct a new BMAV wing design. A dragonfly (*Odonata*) was selected for biomimicry, because they are highly maneuverable flyers, capable of hovering, rapid forward flight, or reverse flight. Therefore, structurally analyzing these wings could yield results that inspire the design of more effective wings for BMAVs. The overall objective of this research is to develop a simplified wing model for a BMAV, bioinspired from actual dragonfly wings. A simplified model was created using spatial network analysis, a topological optimization method. These simplified wing frame models were then fabricated using seven different types of materials. Stainless steel type 321, balsa wood, red pre-impregnated fiberglass, black graphite carbon fiber, polyvinyl acid, acrylic and acrylo-nitirile butadiene styrene. These wing frame structures were fabricated using laser cutting machine and a 3D printer. These wing frames were then immersed in a chitin-chitosan membrane by a casting method. These wing frames were subjected to

mechanical testing’s such as bending and tensile to study its suitability for use in a BMAV. A flapping mechanism was also created and used to produce flapping motion on these BMAV wings and an actual dragonfly wing (for comparison). The aero elastic properties of both the BMAV and actual dragonfly wings were examined using two high speed frame camera. The bending angle, displaced distance or deflection, wing tip angle, and the wing tip rotational twist speed were analyzed at the flapping frequencies of 10,20, 30 Hz, 60 Hz and 120 Hz.

ABSTRAK

Kenderaan udara mikro biomimetic merupakan sebuah jentera yang tidak memerlukan pemandu dan bersaiz mikro. Inspirasi untuk mereka bentuk kenderaan seperti ini diperoleh dari melihat serangga yang boleh terbang. Kenderaan udara mikro ini merupakan teknologi yang baharu dan sedang berkembang di dalam bidang aeroangkasa. Kenderaan mikro ini memporeleh definisi daripada US Defense Advanced Research Projects Agency (DARPA) pada tahun 1997. Mereka mengkategorikan kenderaan tanpa pemanudu ini haruslah mempunyai ukuran dimensi yang kurang daripada 15 cm. Ini menjadikan BMAV kecil dan ringan berbanding kenderaan udara yang lain. Ini juga membolehkan BMAV sesuai digunakan di kawasan yang kecil dan sukar dilalui manusia (kawasan yang dikelilingi kabel voltan tinggi serta lorong yang sempit). Maka, komponene struktur BMAV mestilah ultra-ringan, padat dan fleksibel. Kajian terdahulu memberi tumpuan kepada sayap yang statik yakni mengurangkan skala kapal terbang yang sedia ada. Sayap seperti ini tidak sesuai bagi kenderaan udara mikro disebabkan kurangnya fleksibiliti. Jadi, struktur sayap yang baharu direka untuk BMAV ini. Di dalam penyelidikan ini, sayap pepatung telah dimimik untuk merekabentuk sayap baru bagi BMAV ini. Spesis pepatung (*Odonata*) telah dipilih untuk dimimik keranapepatung merupakan serangag terbang yang sangat efisien. Pepatung boleh melakukan pelbagai aksi sewaktu terbang seperti terbang tanpa mengibas sayapnya untuk waktu yang lama, terbang sambil menukar arah, atau terbang songsang. Objektif penyelidikan ini adalah untuk merekabentuk sayap model sayap yang telah disimplifikasikan untuk BMAV. Sayap pepatung menjadi model inspirasi kami. Sayap pepatung ini disimplifikasikan menggunakan kaedah optimasi yang dinamakan “ spatial network analysis’. Tujuh jenis bahan digunakan untuk menghasilkan model sayap ini. Keluli tahan karat jenis 321, kayu balsa, fiberglass merah, carbon fiber, polyvinyl acid, acrylic and acrylo-nitrile butadiene styrene. Sayap ini dihasilkan menggunakan mesin

laser dan printer 3D. Sayap ini kemudiannya disalut dengan membran chitin-chitosan. Ujian tegangan dan lenturan dijalankan ke atas sayap ini. Sebuah mekanisme yang memiliki kebolehan mengimbas disediakan bagi menguji kebolehan sayap-sayap yang dihasilkan ini. Bagi membandingkan kebolehan sayap-sayap ini, sayap pepatung yang sebenar juga diuji di atas mekanisme ini. Kebolehan aero-elastik sayap sayap ini diukur dan dibandingkan dengan sayap pepatung yang asal menggunakan dua kamera halaju tinggi. Ukuran seperti sudut lenturan, jarak imbasan, sudut hujung sayap, sudut putaran hujung sayap dan halaju putaran hujung sayap diuji pada frekuensi 10, 20, 30, 60 dan 120 Hz.

DEDICATIONS

this thesis is dedicated especially

to my beloved father, mother, and husband

Mr. Sivasankaran Nair, Mrs. Santhakumari and Mr. Rajendra Nath

The caring ones,

Kishan Nair Sivasankaran, Rubentheren Viyapuri

Respected supervisors,

Dr. Thomas Arthur Ward

Associate Professor Dr. Mohd Rafie Johan

Thanks for all the support.

My love for you all remains forever.

ACKNOWLEDGEMENT

I take this opportunity to express my profound gratitude to my supervisor Dr. Thomas Arthur Ward for his exemplary guidance, monitoring, patience and constant encouragement throughout the duration of my studies. I would also like to acknowledge with much appreciation the supportive role of my co-supervisor Associate Professor Dr. Mohd Rafie Johan for guiding me professionally throughout the candidature.

I would like to express the deepest appreciation to all my lab members Mr. Rubentheren Viyapuri, Mr. Christopher Fearday and Mr. Erfan Salami. I'm thankful for being blessed with a friendly and cheerful group. They were always there to lend me a helping hand under many situations. I wish to take this opportunity to express my heartfelt gratitude to all of them. I also take this opportunity to express a deep sense of appreciation to lab assistants Mr. Fauzi who have helped me during my lab experiments. Special thanks to University Malaya for sourcing me a quality workstation.

Of course no acknowledgments would be complete without giving thanks to my family. I would like to thank my family for their unconditional support. In particular, the motivation and encouragement given by my husband has helped me pull through many critical situations throughout my candidature. Also, the absolute love and blessings showered by my mum, dad, and brother. A special thanks to Rubentheren Viyapuri for being a good friend in need.

Above all, I thank God for his grace, wisdom, favor and protection. I could never have done this without the faith I have in you, Baba.

There are so many others whom I may have inadvertently left out and I sincerely thank all of them for their help.

TABLE OF CONTENTS

LIST OF FIGURES

LIST OF TABLES

LIST OF SYMBOLS AND ABBREVIATIONS

Symbols and Abbreviations	Full name
UAV	Unmanned aerial vehicle
MAV	Micro air vehicle
BMAV	Biomimetic micro air vehicle
Hz	Hertz
PLA	Polylactic acid
ABS	Acrylonitrile-butadiene styrene
dpi	Dots per inch
m	Meter
μ	Micro
FEA	Finite element analysis
ω	circular frequency
θ	Bending angle
d	Displaced distance or deflection
α	Wing tip angle
CAD	Computer aided design
3D	three dimensional
mm	millimeter

MPa	Mega Pascal
GPa	Giga Pascal

LIST OF APPENDICES

CHAPTER 1: INTRODUCTION

1.1 Biomimetics

Biomimetics or biomimicry is a concept of imitating elements of nature to solve or to ease complex human tasks. The terms biomimetics and biomimicry come from Ancient Greek: *biosmimesis* or *biosmios* which means imitating life (Julian et al. 2006). The development of biomimetics has created new bio-technological solutions at macro and nanoscales. The application of biomimetics can be seen in many fields from cars to computers. Optimization methods such as swarm intelligence and artificial neural networks were inspired by biomimetics. There are three areas in where biotechnological solutions can be applied (Rhett Butler, 2015): Replicating natural production methods (chemical compounds from plants), Mimicking mechanisms found in nature (dragonfly, Velcro) and finally observation of social behavior of organisms (ants and bees).

1.2 Unmanned aerial vehicles (UAVs)

The Unmanned Aerial Vehicle or commonly known as UAV, is an aircraft with no pilot on board. UAVs can be controlled by a ground control station, routed by pre-programmed flight plan or fitted with a complex automation system. UAVs are currently used for a number of missions, including reconnaissance and attack roles.

Micro air vehicles (MAV) are a new type of unmanned air vehicle which is significantly smaller than a UAV. Defense Advanced Research Projects Agency defines a MAV as an aircraft which has a size less than 15 cm in length, width or height. This puts MAV smaller than any UAV developed to date. MAVs should be thought of as aerial robots, whose mobility will allow them to be deployed to remote or hazardous locations to perform a variety of missions which includes surveillance, targeting and even rescue missions. (Michelson et al, 2002). There are different types of MAVs such as fixed wing models, (FMAVs) rotary wing models (RMAVs) and insect-like (flapping wing) models, (BMAVs). FMAVs are micro-scaled air vehicles with fixed (stationary) wings that generates lift but not thrust. There is a separate system attached (propulsion) to generate thrust. They are used in non-confined spaces because they should maintain a continuous forward velocity in order to generate lift (wings). Rotors are used to achieve lift and thrust for RMAVs. Since they are able to hover they are much efficient than FMAV. However, the size is their limitation. RMAVs are generally larger than FMAVs or BMAVs. BMAVs are micro or nano-scaled aerial vehicles biomimicked from a biological organism. BMAVs are the smallest MAVs designed and they have flexible flapping wings. Due to their small-size range, the BMAVs are able to travel in confined spaces. According to James and Michael (1997) the system components in a MAV should be integrated and possess multifunctional characteristics to be able to overcome the challenge faced in designing an aircraft with constrained dimensions. A MAV may only weigh about 50 grams yet; MAVs must be capable of hovering as long as 20 to 60 minutes while carrying a load of 20 grams a distance of approximately 10 km. It is essential to find the suitable materials and the optimum structural balance for a MAV (James and Michael, 1997).

1.3 Problem statement

The study of biomimetics as mentioned earlier has motivated research into a new class of micro-sized unmanned aircraft called Biomimetic Micro Air Vehicles (BMAVs). Due to their small size and weight, BMAVs would be ideal for flying indoors or in enclosed spaces. The primary payloads envisioned for a BMAV are ultra-lightweight, compact electronic and surveillance detection equipment. Their miniature size makes them difficult to detect, easy to quickly deploy by a single operator and relatively inexpensive to fabricate, and allows the potential to fly them inside buildings or compact spaces. BMAVs are envisioned for use on civil and military missions that are of a limited duration, such as: remote sensing of hazard sites (e.g. chemical spill, radiation, high voltage power lines etc.), indoor video mapping, and police or military surveillance.

Some research has been conducted to biomimic the wing structure of dragonflies. TU Delft researchers have developed the DelFly Explorer, a low weight (20 grams) MAV which flaps and avoid obstacles autonomously (Michelson et al, 2002). Festo created BionicOpter, a fully functional robotic dragonfly which is able to perform the aerial acrobats of an actual dragonfly. BionicOpter is much larger than an actual dragonfly with a weight of 175grams (TA Ward et al, 2015). Dragonflies (*Odonata*) have a highly corrugated wing structure that consists of complex, wing membrane patterns (e.g. quadrilaterals, pentagons and hexagons). Each pattern contributes to the wing's flexibility and stiffness, which determine its ability to withstand deformations. Although some research has been conducted to biomimic the wing structure of dragonflies. (Tu Delft, 2013 and Yirka, 2013), none of these works biomimicked the actual wing structures of dragonfly. Although other insect wings (e.g. cicada, beetle, etc.) have been replicated, dragonfly wing structures are very complex making this difficult. Dragonfly wings are highly corrugated in pattern, with differing thickness and tubular structures. Replicating an exact copy is not a practical approach, due to limitations in fabrication methods. So a simplified model is needed that takes these limitations into consideration. Like the wings of a flying insect, the artificial wings of a BMAV not only must be flexible but also strong enough to endure the aerodynamic forces produced by flapping motion. During flight, the wings undergo significant bending and twisting deformations that can alter the direction and magnitude of the aerodynamic forces generated (Combes S, 2003, 2010, Shang J.K et al, 2009)

Several fabrication methods for small insect-scale artificial wings have been proposed. Combes and Daniel (2010) measured the wing flexibility of several insects and found that the spanwise flexural stiffness was one to two orders of magnitude larger than the chordwise flexural stiffness. The scope of their investigation was limited due to the diversity in venation as well as the complex cross-sectional and planform geometries of the insect wings. In contrast, the morphology and materials of artificial wings can be manipulated to understand the effect of these properties on wing flexibility. Tanaka and Wood (2010) investigated the effects of flexural and torsional wing flexibilities on lift generation in hoverfly flight using an insect-scaled mechanical model of an artificial wing. There are several past research studies that focus on insects such as hoverfly, beetle and humming (Tanaka et al. 2010, Nguyen et al. 2010 and David et al. 2014). Also, most past literature involves wing membrane materials (Bao, 2011, Ko, 2012, Joong, 2013). Very little has been written about the BMAV wing frame structures that encase the membrane. Several past research publications have been conducted on flying insect wing structures to understand their aeroelastic properties. Ward et al. (2015) conducted a review on the percentage of flying organisms studied; hawkmoth (44%), dragonfly (23%), beetle (10%), butterfly and humming bird (7%), bat (4%), fruit fly (3%), honey bee (2%) and damselfly (1%). Herbert et al. (2000) conducted numerical investigations on a tethered desert locust (*Schistocerca gregaria*). They concluded that the wings must undergo an appropriate aeroelastic wing deformation (through the course of a wing beat) in order to achieve an efficient aerodynamic flow suitable for lift and thrust generation. Several studies showed that flexible wings, capable of changing their camber, generate higher peak lift forces than rigid wings (Mountcastle and Young, 2009).

Wing flexibility also prevents small tears or warping from occurring. Newman et al (1986) suggested that dragonfly wings appear to be adapted for reversible failure in response to excess loads, enabling them to avoid permanent structural damage. Most past research examined the effects of wing flexibility on aerodynamic performance by either using numerical models or experimentation. However, very few researchers have attempted to mimic the detailed structure of an actual insect wing. Hence, the overall objective of this research would be to create a simplified dragonfly wing model for use in a BMAV. This wing model is envisioned to be able to match the performance of an actual dragonfly wing.

1.4 Objectives

The overall objective of this research is to model a simplified dragonfly wing that matches the performance and capabilities of an actual dragonfly wing. Firstly, a simplified model of the complex corrugated dragonfly wing is created. As previously stated, this model has a simplified design to suit appropriate machining tolerances. A mode analysis and static bend-twist coupling studies were made on computer simulations of these models. Secondly, these simplified models were fabricated using different materials. Simulations and tensile and bending experimental tests were done to determine the most suitable material. Thirdly, the most promising materials were attached onto a flapping mechanism and their aero-elastic properties were measured. These were compared with an actual dragonfly wing for comparison purposes. Listed below is a summary of the objectives performed: analysis of dragonfly-inspired BMAV wing structures (e.g. patterns, veins, and tubules of dragonfly wings) includes designing a simplified wing structure optimized using spatial network analysis, conducting finite element analysis including modal analysis and other mechanical simulation testing on the simplified design (static bend-twist coupling), fabricating simplified wings using different materials (e.g. steel, balsa wood, carbon fiber, red fiberglass, acrylic, ABS, and PLA), conducting mechanical testing on fabricated wings to ensure it matches the capability of an actual dragonfly wing and finally to test the fabricated wings (chosen material) on a flapping mechanism to assess the performance of each design.

1.5 Procedures

Figure 1.1 below shows the summary of the procedures involved in the fabrication of these wings.

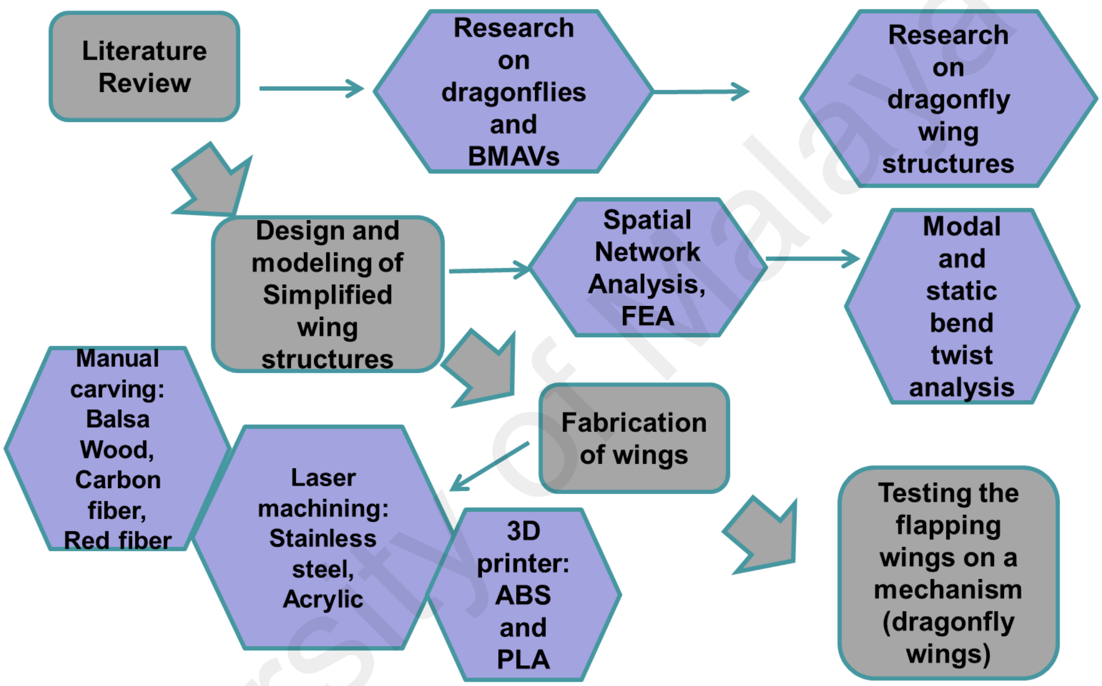

Figure 1.1: Illustration of the overall procedures in developing a BMAV wing frame

Figure 1.1 describes the overall steps involved in this research. It starts with a comprehensive literature review which includes a research of dragonflies and BMAV in general and research of dragonfly wing structures specifically. The second step involves design and modeling of simplified wing structures using spatial network analysis, FEA (finite element analysis), modal analysis, and static bend twist analysis. The third step involves fabrication of the wings using different method (manual carving, laser machining and 3D printer) and finally testing these fabricated wings on a flapping mechanism.

1.6 Outline of thesis

There are five chapters in this thesis, and a list summarizing them is as stated. The first chapter introduces BMAV and their potential applications. It provides an overview of this research and lists the primary objectives. It also lists layout of the procedure for accomplishing these objectives, the second chapter reviews past researches done with a similar objective. It gives a brief review of past research done on dragonflies and other related topics that subsequently contributes to this research. Other review on related topics include mechanism of insect flight, simulation of insect flights, flapping mechanism created by other researchers, finite element analysis studies done on insect flight, fabrication of artificial wing frame and membranes of insect and the high speed camera imaging technique. In the third chapter, experiments are discussed extensively. Sufficient details are given so that future readers can replicate this work. It discusses the topological optimization method used which is spatial network analysis, the finite element analysis options chosen and the mode analysis study made for both detailed and simplified wings, the mode shape comparison, the static bend-twist study conducted, the materials used for the fabrication of the simplified wing models, the simulation and experimental tests done on the fabricated wing frames and, finally, the high speed camera technique used to capture the parameters necessary for an aero-elastic study, The fourth chapter discuss and assesses all the data acquired from the experiments. Where possible, these results are compared with data collected by other researchers, and the last chapter summarizes and concludes this research. It lists the experience and challenges faced while performing these studies and also suggest improvements that can be done in future studies.

CHAPTER 2: LITERATURE REVIEW`

2.1 Introduction

This chapter highlights several subtopics that were studied to support this research. The chapter introduces insect flight concepts, the wing structure of dragonflies, the spatial network analysis, the type of artificial wings fabricated in previous insect studies, testing conducted in previous studies, types of flapping mechanisms, and data collected from previous high frame rate imaging system studies.

2.2 Insect flight

The size of insect wings is not an indication of the insects' ability to fly. Flies and certain types of ants (Dobsonflies and Antlions) with large wings are poor fliers when compared to wasps and bees that have smaller wings (Smithsonian, 2010). Flight in insects enabled them to protect themselves from danger, as a means of survival (food hunting), reproduction, and to search for new habitats (Monarch Butterflies) (Rose, n.d)

Wing flapping patterns of insects can vary significantly from one species to another. The African Grasshopper, has the ability to fly hundreds of miles in search of food. This is mainly attributed to their complex wing structure ("Smithsonian", 2010). Wings typically make up approximately 1%-2% of an insect's total body mass. In dragonflies, they must flap a million times in an average lifespan of an insect but not without enduring collisions, torsional loads and other various forms of deformation (Kutsch, 2002).

2.3 Dragonflies

Separate muscles control the fore and hind wings, making the phase relation between the 2 parts as a distinctive feature of the dragonfly's wing movement. For an example, both parts tend to beat closer in phase during takeoff but out of phase when hovering. A reduction in oscillation is the main reason the dragonfly varies the phase for different maneuvers. The relatively close distance between the fore and hind wings, about a wings width apart, allows both parts to interact aerodynamically (Jane, 2004).

Dragonflies have shown different flight styles. The four different flight styles observed in dragonflies are (Norberg, 1975): Counter stroking (fore and hind wings move up and down about 180 degrees non-symmetrically), phase stroking (hind wings cycle about 90 degrees before the fore-wings), synchronized stroking (fore and hind wings move in unison) and gliding

Figure 2.1: Dragonfly species used in this study

Of the 4 different styles, the counter stroking is the most used when they are either hovering or flying very slowly. This is both a powerful and efficient way of flying and generates a lot of lift (Rüppell, 1989).

When flying at average speeds, phase stoking is the preferred style. This method generates more thrust but provides less lift when compared to the counter stroke. In order to maximize thrust or to change directions fast, the synchronized stroke is employed by the dragonfly. Finally, gliding where three different types of gliding have been recognized (Reavis et al, 1988); free gliding ; where the insect stops stroking and glides slowly down, updraft gliding at hill crests ; where the insect adjusts its wing position to float in the air without the need to beat its wings, gliding in towed females ; where the female insect in the wheel position holds her wings out and glides while the male provides the motion force. (This is during the mating position). The muscles used to flap the wings are attached to the wing base. Elevated muscle temperature increases flapping efficiency. For this reason the dragonfly spends a lot of time and energy to maintain their flight muscles at elevated temperatures (Reavis et al. 1988, Saharon et al. 1987). The dragonfly thorax appears skewed when at rest, but at flight, the head is held low and the stroke of the wings are parallel to the long axis of the flight muscles. This is done to improve mechanical efficiency. During each stroke, smaller controller muscles (operating at the base of the wings) adjust the wing shape and angle of attack. Four different thrust generating mechanics may be employed by the dragonfly (Sun, 2002). The four different mechanisms used by the dragonfly are: classical lift, supercritical lift, vortices and vortex shedding.

When the attack angle of the wing passes a critical value, supercritical lift occurs. Similar to hovering, a high lift is generated over a short distance after which the wing stalls. Dragonflies can maintain this position continuously by using short wing strokes. The use of vortices and shed vortices in insect flight by Usherwood et al. (2002) was explored. Both the movement of the wings through the air and the twisting of the wings at the end of each stroke to generate thrust.

Dragonfly wings are not simple planar objects but complex dynamic structures. The corrugations in the wings holding an aero-foil of air around the wings have the following effects: Lower friction, wings are able to flex around several axes, and being able to respond to both muscle actions and to inertia effects. The pterostigma on the leading edge near the tip of the wings are weights that improve the aerodynamic efficiency by causing the wing tip to flex during a wing stroke. Dragonflies can fly with asymmetrical wing stokes. This is achieved by varying what their wings are doing in a coordinated fashion. They have to master to adjust wing shape, stroke length, angle of attack, stopping either wings independent of the other and adjusting the relationship between any two wings on either side of the body are among a few of the many subtle adjustments made in order to maintain their flight style (Ellington, 1984 (a),(b) and 1985).

Dragonflies have a natural frequency range of 120-200 Hz and a wingbeat frequency of around 30Hz. The flapping of the wings creates a whirlwind surrounding the wing area. A dragonfly uses a rowing motion along an inclined stroke plane. When hovering, the body lies almost horizontal while the wings push backward and downward with the addition of the feathers slicing upwards and downwards at the end of each stroke (Grodnitsky, 1999). In contrast to the dragonflies asymmetrical rowing motion, many other insects use symmetrical back and forth strokes near a horizontal stroke plane. This type of motion also allows a dragonfly to support much of its weight by the upward drag created during the down-stroke. The flapping motion of an actual dragonfly is shown in Figure 2.2.

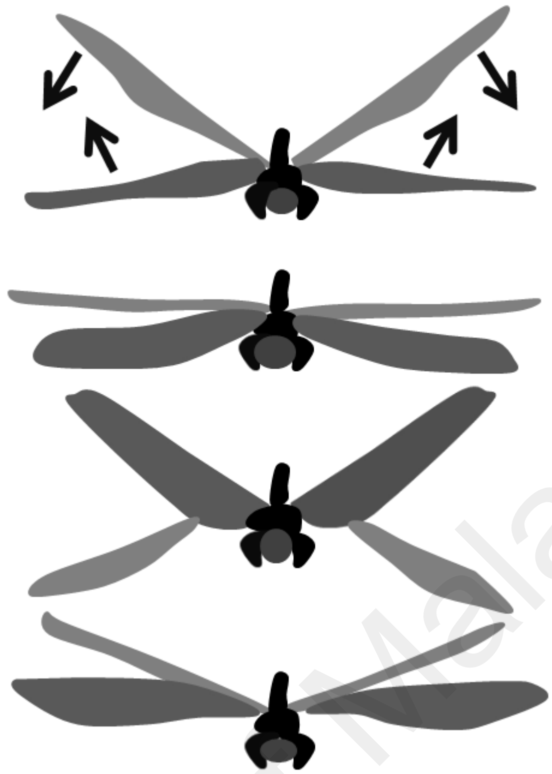

Figure 2.2: The front view of a dragonfly in flight.

From observation and inspection on high speed films, dragonfly wings are found to have plastic like features. Observations from high speed films show that the torsional wave propagates from the wing tip to the root during pitch reversal. This would be in the opposite direction if the muscles were actively pitching the wing, as one would expect the propagation to start from the root. Aerodynamic forces and wing inertia are responsible for pitching the wing in this tip-to-root direction (Ellington, 1999). The aerodynamic torque and inertial force associated with the observed wing motions can be computed and confirmed that they are sufficient to pitch the wings of dragonflies and other observed hovering wing motions. In order to simplify control and save energy, insects can take advantage of the natural swinging motion near the end of its wing stroke (Lehman et al, 2005).

Dragonflies have a very respectable power to weight ratio. (The dragonfly has a mass of less than 0.028 kg and can reach a speed of 1.6 km/h). This allows them to accelerate up to 4g in a straight line and up to 9g in turns. This has been documented in high speed videotapes of free-flying dragonflies as they pursue prospective prey or when trying to break off attacks. The agility of a dragonfly is the reason it gets much interest from BMAV researchers (Luttgess, 1989).

A dragonfly achieves efficient structural performance because of the variations on its wing pattern. Its ability to withstand deformation can be attributed to the wings flexibility and stiffness. The highly corrugated wing pattern structure is made up of quadrilateral, pentagonal, and hexagonal shapes. Studies have shown that these wing patterns promote rigidity and flexibility along the span of the wing allowing for efficient use of energy required for flight. Conclusions generated by Maybury et al. (2004) are: The wing patterns in general follow the tensile forces exhibited on the wing and the variation in shape determines the amount of flexibility and stiffness in that specific area of the wing

For an example, the more rigid and stiff portions of the wing are the quadrilateral shaped areas, while the more compartmentalized hexagonal areas are regions where bending and swaying take place (Figure 3.1). Also, the degrees at which cells are free to bend are determined by the connections between the cells. Two main types of joints occur in the dragonfly wings, mobile and immobile. Some longitudinal veins are elastically joined with cross veins, whereas other longitudinal veins are firmly joined with cross veins. Scanning electron microscopy reveals a range of flexible cross-vein and main-vein junctions in the wing, which allows local deformations to occur (Miller et al. 2004). The occurrence of resilin, a rubber-like protein, in mobile joints enables the automatic twisting mechanism of the leading edge (Akira et al. 1988).

2.4 Biomimetic Micro Aerial Vehicles (BMAVs)

BMAV are micro or nano-scaled aerial vehicles. These vehicles are biologically-inspired from flying insects, birds and bats to achieve lift and thrust by flapping their wings. BMAV are lightweight and highly maneuverable. They are capable of flying in confined areas, rubbles and even indoors. The flapping wings are able to produce a much larger lift compared to a fixed wing. There are many technical challenges involved with designing BMAV such as modelling and unsteady aerodynamics, compact flapping mechanisms, ultra-lightweight materials and structures and importantly an ultra-lightweight power supply. Because of all these factors, there are currently no operational BMAVs but only research based prototypes. Researchers from Delft University of Technology have published numerous articles on their BMAV called Delfly (Tu Delft, 2009). This BMAV only weighs 3 g, and a wing span of 10 cm.

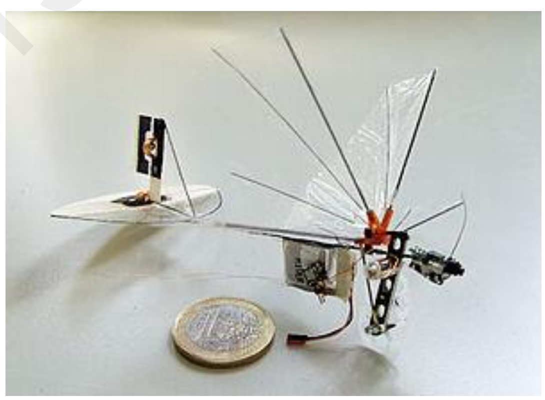

Figure 2.3. Delfly from TuDelft

There are numerous articles published on BMAVs. Various categories are studied under the BMAV field which includes aerodynamics (47%), propulsion and mechanisms

(22%), system design and guidance and control contributes 11% and the studies of structures and materials which is 9% of the total. An ultra-light weight, micro-sized mechanism and power supply to enable free flight is the most challenging task in developing a BMAV. Madangopal et al. (2005) analyzed the energetics of a BMAV design with a four-bar flapping mechanism. Conn et al. (2007) created a parallel crank-rocker mechanism that allows unconstrained, integrated flapping and pitching motion. Bolsman et al. (2009) created an actuation mechanism that reduces energy expenditure and amplifies flapping amplitude. Guo et al. (2012) created an actuated flapping wing rotor model using an piezoelectric actuator and did a comparison with their numerical model simulation.

The structures and materials of BMAV are often inspired from flying organisms, such as insects or birds or even bats. Song et al. (2004) made a comprehensive analysis on the mechanical properties of the forewing of the cicada. This serves as a baseline for BMAV materials. Dirks and Taylor (2012) showed that the cross veins of a locust wing provides a barrier against crack propagations. A simplified insect wing model (inspired by a dragonfly) was modeled by Sivasankaran and Ward (2015) based on spatial networking analysis. Rubentheren et al. (2015) produced a chitosan membrane to biomimic a dragonfly wing membrane and applied them to simplified wing frame structures.

2.5 Fabrication of artificial insect wings

Hisayoshi et al. (2014) measured the first natural frequency and the passive deformation of a dragonfly wing. An artificial wing that exhibited the same characteristic was fabricated and the first natural frequency was found to be 120 Hz. This proves that the dragonfly wing does not flap at its natural frequency to avoid resonance effect. Previously, researchers concluded that dragonfly wings flap at their natural frequency to conserve energy (Seiichi et al. 2008). The wing beat frequency of a flapping dragonfly is 30 Hz.

There is a twist at the nodus of the natural wing which increasingly deforms from the base to tip. A carbon rod was used to replicate the leading edge. By this, the artificial wing was able to produce a natural frequency similar to an actual dragonfly wing. The aerodynamic power created was five times higher in magnitude than a carbon wing. Tanaka (2010) demonstrated a method to fabricate corrugated artificial insect wings using a hoverfly as a model. The wing, made of a thermosetting resin, contained veins on a corrugated membrane. This mimics the wing structure of an actual hoverfly wing. The veins and membranes are created by a single 3D mold. The molds were created using a layered UV-laser micro machine.

The surface profile of the fabricated artificial hoverfly wing matched the original mold. The spanwise stiffness of the artificial wing was $2.2 \times 10{-}7$ Nm−2, which is the same magnitude of a natural hoverfly wing. This research has managed to produce an artificial 3D insect wing with micron order precision. Shang (2009) fabricated an artificial wing with defined static properties that were comparable to a natural wing (first approximation). The method described by Shang can be modified to accommodate camber or corrugated profiles. The polydimethylsiloxane (PDMS) mold can be shaped according to the wing pattern and then cured. Spin-coating can be used to allow free flow of the mold onto the venation pattern (although other methods are allowed as well). PDMS or another appropriate polymer can be chosen as a membrane. Etching will further aid in the distribution in a confined area. This can also aid in introducing complex folds and flexion lines just like a biological wing. Dynamic bending and stiffness will be greatly affected by wing mass disproportionality. Since the venation pattern correlates with mass distribution, it is likely that biologically inspired artificial wings can be optimized to exhibit the dynamic properties found in real dragonfly wings. Francis et al. (2001) have fabricated a MEMS polymer structure which integrates the thorax, two wings, and a tergum. These parts were connected with a non-integrated actuator. Based on the experimental results and observation, it was shown that this structure is able to adequately mimic the flexures and twist of real wing motion.

2.6 Frequencies of insect wings

Several studies have been done to find the flapping and natural frequencies of flying insects. Ngoc et al. (2013) conducted experiments to compare the natural frequencies of an actual beetle hind-wing and an artificial wing which biomimics it. Both of these wings were subjected to dynamic vibrations to measure resonance frequencies. The wing mass was measured by an electronic balance. A total of 29 points on an actual beetle hind-wing and 25 points on the fabricated artificial wing were painted to aid the laser sensor in measuring the deflection of the wing. The recorded frequencies of beetle hind wing were 47.5 Hz, 88 Hz, and 176 Hz, respectively. Since the flapping frequency of a beetle ranges from 35 to 40 Hz, it was assumed that the higher mode shape would have little effect on the shape of the wing (deformation). Additionally, Ngoc et al. 2013, studied the relationship of eight different insect species. The wingbeat frequency of these flying insects was measured using a high-speed camera (imaging technique) while the natural frequency was determined using a laser displacement sensor. Ngoc found that there is a prominent ratio between wingbeat frequency and natural frequency. This ratio is 0.12-0.67 for insects flapping less than 100 Hz and 1.22 for those with higher wingbeat frequencies. These findings suggest that these frequencies do correlate with each other.

2.7 Static test conducted on real and artificial insect wings

Rajabi et al. (2011) performed a detailed study on dragonfly wings using SEM. These images are used to study the morphology and microstructure of an actual dragonfly wing. A micro tensile tester was used to study the mechanical behaviors of the wing. An overall observation shows that the wings have a highly corrugated structure. This is believed to increase the overall stiffness of the wing and possibly prevent initial crack and tear. This indirectly provides a tough barrier to the wing (preventing crack propagation by closing the crack tip). The critical region of the wing is the nodus. The corrugations also provide a high load bearing capacity and flexibility. The hollow shaped tubules can be assumed to provide a high fatigue resistance especially when the wings are subjected to dynamic loadings (flapping motion). They also increase the flexibility of the wing structure, thereby affecting its fatigue resistance. Rajabi presents the fracture strains obtained as a percentage value whereby the forewing and hindwing values are 5.65% and 5.58%, respectively.

Song et al. (2004) tested longitudinal veins (costa and radius) extracted from four damselflies and tested in a micro-tensile machine. The specimens were held with a special paper frame. The specimens were classified into two categories: fresh and dry. The average tensile strength of the actual (fresh) and dry costa are 251 MPa, and 232 MPa. The average modulus value for the actual (fresh) and dry costa are 14.37 GPa, and 14.43 GPa, respectively. These values are found to be essentially the same which shows that aging does not give any significant impact on tensile properties (costa was left to dry for a year). The average tensile strength of fresh (actual) and dry radius are 285 MPa and 278 MPa. The modulus of an actual (fresh) radius and dry radius are 16.87 GPa, and 14.89 GPa, respectively.

2.8 Flapping mechanism

Francis et al (2001) proposes a novel micro flying machine concept based on MEMS technologies, which could potentially perform ascending, linear movement and rotation. The principal advantage of using such technologies is that the solutions proposed in the design process can be easily scaled down. The first step involves studying the feasibility of design and machining a type of stainless steel artificial wing. Few flying insects (weighing 1 gram) are able to flap their wings which have dimensions in the range of 10mm to 30 mm. These insects flap with a frequency of 20 Hz to 150Hz. Secondly, a linear electromagnetic actuator was proposed to excite the wings. Usage of the actuator has proven advantageous as the excitation frequency can be adapted to the wing resonance frequency. In the near future as proposed by the authors, a simple control mechanism can be integrated to control the mechanism by having different oscillations on both sides (right and left) without modifying the original mechanism. There should be more research done focusing on the improvisation of the flapping mechanism.

CHAPTER 3: RESEARCH METHODOLOGY

3.1 Introduction

This chapter introduces the methods employed to conduct the experiments and simulations in this research project. It is ordered as follows: wing model overview, topological optimization, method and types of analysis used, wing frame fabrication process, static stress experiments, the flapping mechanism and the high speed imaging technique set up.

3.2 Wing model overview

The dragonfly species used in this study is called Diplacodes Bipunctata. This species has a distinct red discoloration with a wing span and body length of approximately 0.055 m and 0.035 m, respectively. A digital image (resolution 1600 dpi) was taken of this dragonfly using a Nikon D7000 camera (Figure 3.1). Both the fore and hind wings were modeled from this digital image.

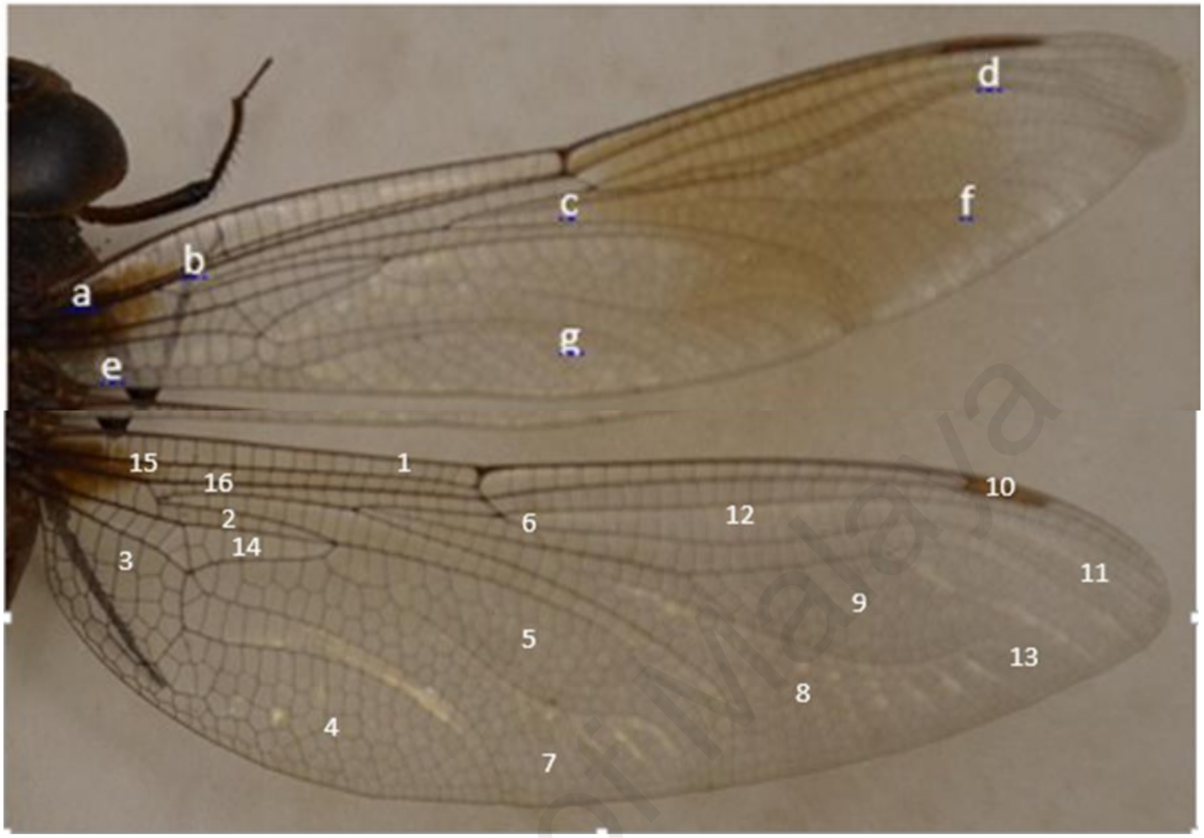

Figure. 3.1 Main parts of a dragonfly wing

a) Radial ; b) Costa- leading edge (rectangular pattern throughout) the stiffest pattern of all parts; c) Nodus (part of the vein which is much thicker than the others, plays a pivotal role in the dissipation and storage of mechanical energy); d) Pterostigma (behaves as a dampener);

e) Anal margin and supercosta; f) Small hexagonal patterns which are compactly arranged ranging from 0.0001 to 0.0002 m in size; g) Large quadrilateral and hexagonal patterns ranging from 0.0002 to 0.0004 m in size. 1-15) Dragonfly wing patterns that are divided into several regions for further study.

3.3 Spatial network analysis

Spatial network analysis as mentioned in Chapter 2 is a graphical topological optimization method that is used in various fields involved with geographical maps. A spatial network (sometimes also called geometric graph) is a graph in which the vertices or edges define spatial elements associated with geometric objects, which means the nodes are located in a space within a specified unit (e.g. radius or distance). There are various methods of conducting spatial network analysis. Geographical Information Systems used this method to explore geographic spatial patterns (Angel, 2010). Our methodology is similar, but we are applying this algorithm (based on shape, angle and density) to a biological structure (a dragonfly wing). The idea of simplifying a dragonfly wing based on spatial network analysis was inspired by observing its compactly arranged geometrical patterns. Although there are a variety of methods available to conduct a spatial network analysis, the proximity proposition method was chosen for this analysis because of its conformity of use to a wing structure. The proximity proposition states that among all shapes available, the circle has the shortest average distance to its center (Angel, 2010). Since there are many possible centers for a known shape, it is essential to define at least one appropriate center of a shape before defining a Proximity Index: The Proximate Centre is defined as the center of gravity of a shape. The Proximity Index: ratio of the average distance from all points in the equal-area circle center: average distance to the Proximate Centre from all points in the shape.

Frolov (1975) computed that the mean distance to the centre of a circle is equal to two thirds of its radius and suggested that it would be quite accurate to be used as a measure of compactness. The Proximity Index therefore uses Frolov’s equation. In our case, this new approach is initiated due to the fact that after close observations, it could be noted that the

3.3.1 Canny edge detection algorithm

The image was imported into Matlab and segmented using the Canny edge detection algorithm, resulting in a logical image illustrated with point clouds. This grayscale image was then smoothed with a Gaussian filter to suppress noise. The main vein structures were manually traced out and divided into sections using splines and polygons. An edge detection algorithm was required to define the different regions separated by veins in the image of the wing. The Canny edge detection algorithm is one of the most popular algorithms, because of its detection of edge at a low error rate. The algorithm runs in five steps which are:

1) Using Gaussian filter to smooth the image and remove noise;

All camera digital images will possess some amount of noise (blurry lines or edges, dots, etc). Noise must be reduced to avoid errors caused by wrongly assuming the noise as a part of the edge. This is an essential first step for Canny edge detection algorithm. The image must then be smoothed using a Gaussian filter. The filter is applied using a matrix quadrant as shown in (1) below:

$$\frac{1}{x}\begin{vmatrix} a & b & c & b & a \\ b & d & e & d & b \\ c & e & f & e & c \\ b & d & e & d & b \\ a & b & c & b & a \end{vmatrix} \tag{3.1}$$

2) Edges are detected where the computed intensity gradients are the largest;

The Canny algorithm finds edges where the grayscale intensity of the image changes the most. These areas are found by determining pixel gradients in the image. Sobel-operator (feature detection filter in Matlab) is applied to determine the pixel gradients in the smoothed image. Gradients are approximated in the x- and y-directions by applying the kernels shown in (3.2) and (3.3). In these equations KGX and KGY represent the kernel matrices and *a* and *b* are unknowns;

$$K_{GX} = \begin{vmatrix} -a & 0 & a \\ -b & 0 & b \\ -a & 0 & a \end{vmatrix} \tag{3.2}$$

$$K_{GY} = \begin{vmatrix} a & b & a \\ 0 & 0 & 0 \\ -a & -b & -a \end{vmatrix} \tag{3.3}$$

The strongest edges can then be assumed as an Euclidean distance. This can be measured by applying the law of Pythagoras. It can also be simplified by applying Manhattan distance formula as shown in Equation 3.2. The Euclidean distance value is then applied to the image. The computed edge stresss are then compared to the smoothed image;

$$|G| = \sqrt{G_x^2 + G_y^2} \tag{3.4}$$

where Gx and Gy are the gradients in the x- and y-directions respectively.

Equation 3.5 shows the method to determine the direction of the edges.

$$\theta = \arctan\left(\frac{|G_y|}{|G_x|}\right) \tag{3.5}$$

3) Local maxima are marked as edges;

The blurred edges are converted to sharp edges in this step. The highest value (maximum) gradient is preserved and the others are deleted. The algorithm for each pixel in the gradient image is outlined below:

1. Convert or round all the nearest θ (gradient) to the nearest 45°.

2. The edge stress of the current pixel in both positive and negative directions are compared. For example, if the gradient direction is north (90°), compare with the pixels to the north and south.

3. Check to see that the edge stress of the current pixel is the largest. If not, remove the value.

4) Use double threshold to detect potential edges;

The non-maximum values of the gradients may be the true edges of the image but they were not strong due to the large effect of noise or color variation. The simplest way to distinguish them is to use a threshold. The Canny edge detection algorithm uses a double thresholding method (Matlab)

5) Track edges via hysterisis whereby final edges are determined by suppressing all non-connected edges to a prominent edge.

Strong edges can immediately be included in the final edge image. Even if there is a lot of noise interference, this noise will not be strong enough to mask strong edges. (for threshold levels that are properly adjusted). Weak edges are included if they are deemed to be a part of the true image and only if they are connected to strong edges. BLOB-analysis (Binary Large Object) was used for edge tracking. This preserves strong edges are preserved while suppressing weak edges.

3.3.2 Proximity index

The smaller vein structures were then modeled, in a similar way, to match the detailed patterns and densities shown in the logical image. The spatial network analysis method (proximity index) was employed to perform the segmentations. Although there are a variety of methods available to conduct a spatial nework analysis, the proximity proposition method was chosen for this analysis because of its conformity of use to a wing structure. A circle is the most compact geometric shape possible, so this was selected as a reference defining the specified unit (radius) (de Smith et al. 2007). The proximity proposition is defined as the shortest average distance of a circle in a given area of symmetrical shapes. The proximity index is the ratio of the proximate center from all points in the shape. Where (x_i, y_i) are the coordinates of a particular node (i), n is the total number of nodes, and (x_c, y_c) are the fixed coordinates of b_{ref} (point of reference).

The mean distance (d_{CA}) of any point bounded by the circle (of radius R_A) to its center is given in Eq. 7(de Smith et al. 2007):

$$d_{CA} = \frac{1}{\pi R^2}\int_0^{R_A} 2\pi r^2\, dr = \frac{2}{3}R_A \tag{3.7}$$

Since

$$R_A = \sqrt{A/\pi} \tag{3.8}$$

Where A is the area of the proximity circle

Therefore:

$$d_{CA} = \frac{2\sqrt{(A/\pi)}}{3} \tag{3.9}$$

The proximity index (I_y) is the ratio of the proximate center from all points in the shape. The d_{CS} is the radius of the circle. The equation for calculating the proximity index can be written as:

$$I_y = \frac{d_{CA}}{d_{CS}} = \frac{2\sqrt{(A/\pi)}}{3d_{CS}} \tag{3.10}$$

Nodes were manually placed at the vein structure intersections on the dragonfly wing model selected for biomimicry (Figure 3.2). The nodes were only placed on intersections of veins that are 3.0 x 10^{-7} μm thick or lesser. Each circle was manually sized to be the minimum radius required to encompass all of the minor vein patterns (thickness less than

3.0 x 10^{-7} μm) surrounding a single node. In this manner, all of the minor vein patterns were encompassed in one of the many proximity circles inserted.

A fixed wing reference point (bref) is defined as the midpoint of the maximum spanwise length of a single wing (from root to tip). The averaged distance to the fixed reference point (bref) from all nodes is defined by (de Smith et al. 2007):

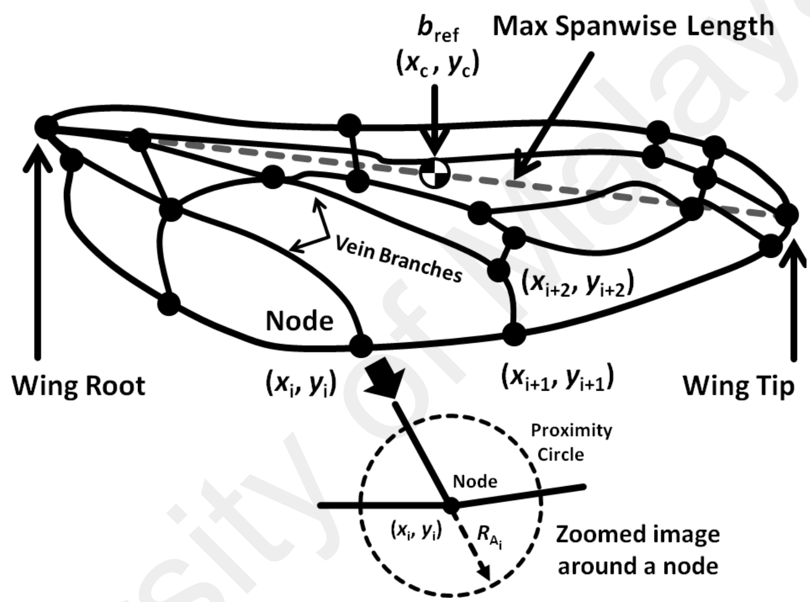

Figure 3.2: Spatial Network Model

[Note: nodes are widely spaced in an exaggerated manner for figure clarity]

3.3.3 CAD model

An initial wire frame, two-dimensional scaled model was constructed using a CAD software Rhinoceros 5.0. This was then exported into AutoCad 2015 to create a three dimensional solid model (Figure 3.3 (a) and (b)). Although there is a difference in thickness across the wing, it is small. For example, the vein at the base and the tip of the wing differ by only 2×10^{-6} m (Li et al, 2009). Therefore in order to simplify the model, average vein and membrane thicknesses of 2.5×10^{-6} m and 3.0×10^{-7} m were used, respectively (Maria, 2011, S. Combes 2010, Jerzy, 2008).

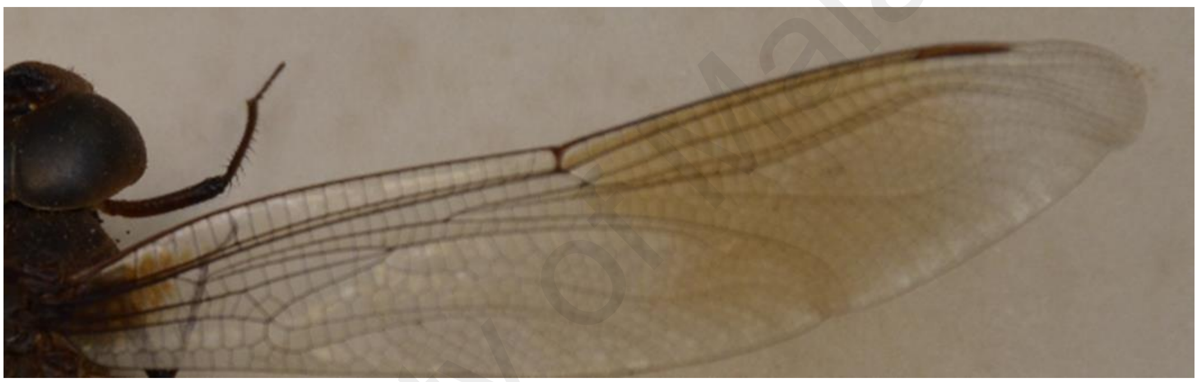

(a)

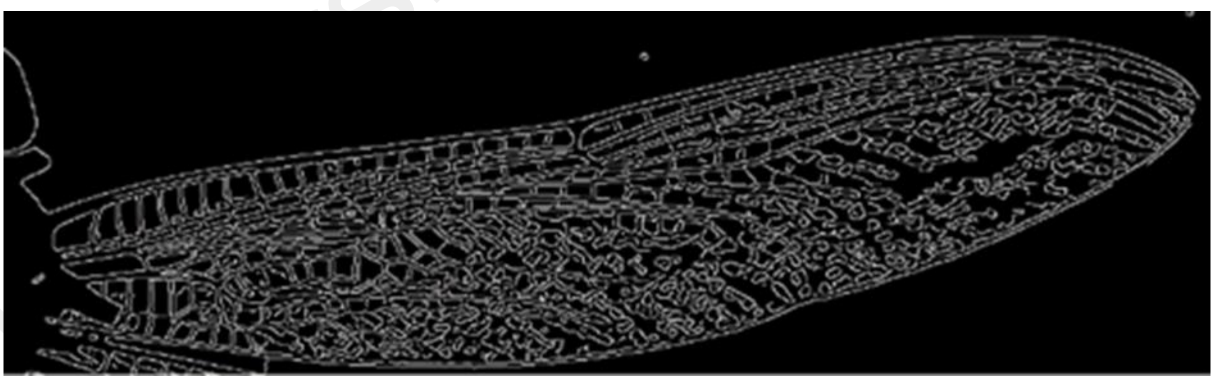

(b)

Figure 3.3: (a) Digital image of the forewing of a dragonfly; b) Forewing created by Canny edge algorithm; c) Canny edge forewing created after noise minimization and main pattern identification; d) Forewing CAD model

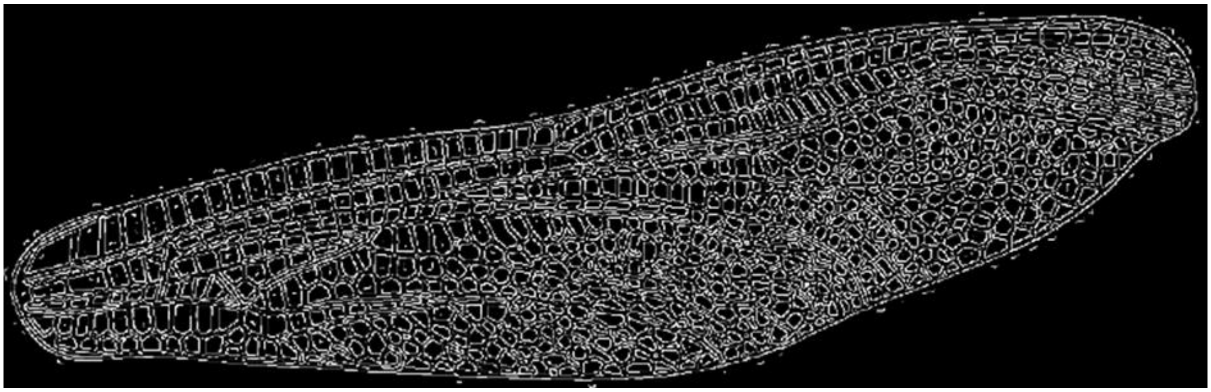

(c)

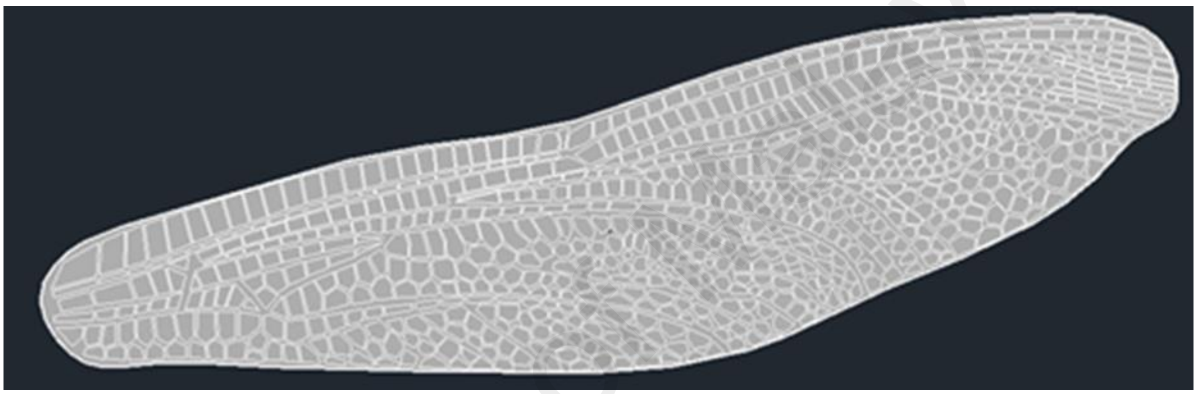

(d)

Figure 3.3: (continued) a) digital image of the forewing of a dragonfly; b) forewing created by Canny edge algorithm; c) Canny edge forewing created after noise minimization and main pattern identification; d) forewing CAD model

3.4 Finite element analysis (FEA)

FEA or more commonly known finite element analysis modeling follows three general rules: pre-processing, analysis and post processing. Equation (3.11) is a general structural equation (Bucalem, 1997):

$$|M|\ddot{U} + |C|u + |K|u = F\cos(At + r) \tag{3.11}$$

Where $|M|$ is the mass matrix, $\ddot{U}$ is the acceleration, C is the damping matrix, K is the stiffness matrix and F is the force vector. The software shall assemble the matrix equation of the structure. The first part would be to solve the matrix equation below:

$$|M|\ddot{U} + |K|u = 0 \tag{3.12}$$

This equation was used to solve the free vibrations of structure. The solution to the equation above gives the natural frequencies (eigenvalues) and the undamped mode shapes (eigenvectors). These are the parameters needed to define the basic dynamical properties of a structure. Since, the main focus is natural frequency, which is a dynamic response, these values are needed in subsequent analysis for dynamic displacements and stresses. For harmonic motions:

$$\ddot{U} = -\omega^{2} u \tag{3.13}$$

In this equation ω is circular frequency. Substituting equation (3.14) into equation (3.13) gives the matrix eigenvalue expression of:

$$|K|-1 = |M| u = |I| u \tag{3.14}$$

In this equation $|I|$ is the identity matrix. The back substitution method is used to obtain the corresponding matrix of eigenvectors $|\Phi|$. The matrix equation of motion for the structure contains off-diagonal terms. The matrix equation may be deduced by introducing the following transformation:

$$u = |\Phi| x \tag{3.15}$$

and writing the following expressions:

$$|\mathbb{0}|T\ |M||\mathbb{0}| = |M^*| \quad (3.16)$$

$$|\mathbb{0}|T\ |K||\mathbb{0}| = |K^*| \quad (3.17)$$

$$|\mathbb{0}|T\ |C||\mathbb{0}| = |C^*| \quad (3.18)$$

In these equations $\mathbb{0}$ is modal displacement matrix, M* is modal mass matrix, K* is modal stiffness matrix and C* is modal damping matrix. The expressions contain only diagonal terms. The damping matrix may be uncoupled on the condition that the damping terms are proportional to either the corresponding stiffness matrix terms or the corresponding mass matrix terms. The uncoupled matrix expressions are:

$$|M^*|x + |C^*|x + |K^*|x = |\mathbb{0}|T\ F \cos(At + r) \quad (3.19)$$

Each equation in this expression then has the form:

$$M_r x_r + C_r x_r + k_r x_r = d_r \cos(At + r_r) \quad (3.20)$$

to which the solution is:

$$n_r = \frac{d_r \cos(At + x_r)}{\sqrt{k_r - m_r X^2)}^2 + (c_r X)^2} \quad (3.21)$$

where c is modal damping coefficient, k is modal stiffness, and m is modal mass. The dynamic displacements, u at frequency ω may then be obtained from the transformation.

$$u = |\mathbb{0}|\eta \quad (3.22)$$

where ŋ is modal displacement.

3.4.1 Element and mesh

The purpose of building an Autodesk model was to calculate the natural frequency and displacement of the wing under a load. The mesh sizes of the elements were viewed visually to ensure the mesh distribution was fine throughout the structure. The mesh was chosen based on the results of a grid study. A grid study was performed to determine the mesh size required for accurate results. The program was run with both coarse and fine grids, with mesh sizes of 0.001 m and 0.0001 m respectively. The difference in results between the coarse mesh and a fine mesh was found to be less than 2%. However, a comparison of the run times of these mesh sizes was 70 % faster for the detailed model and 50% faster for the simplified models. (4 hours for detailed and 2 hours for simplified in the former mesh size). Therefore a mesh size of 0.001 m was used for all subsequent runs.

Shell based elements are often used in finite element analysis models to calculate the displacement. Each element in this model was specified as a shell, in order to simulate the highly efficient load bearing capabilities of an insect wing (Jiyu et al, 2012, Combes, 2010, Tu Delft, 2013, Du Mont, 2009). Teflon was specified as the material for each shell. This is because past research has identified Teflon as possessing similar characteristics to a real dragonfly wing (made up of chitin and chitosan) (Antonia et al, 1998). The model is assumed to have identical material properties in all directions with a single modulus of elasticity and Poisson Ratio value. The properties are summarized in Table 3.1.

Table 3.1: Properties of Teflon

Density	1260 kg/m^3
Modulus of elasticity	6.0 GN/m^2
Poisson's ratio	0.25

Autodesk's Algebraic Iterative Multi-Grid Scheme, with a third order Newton Raphson integration method, was used as the finite element solver. A general element formulation was selected, because this provides a robust solution for thin and thick elements. This was necessary because the wing model is designed with two different type of thickness (vein and membrane). The analysis formulation is set to nonlinear for natural frequency analysis and linear for static stress analysis. The shell element model is set to be isotropic, as it is assumed that the parts will only experience deflection in the elastic region of the material.

3.4.2 Modal analysis: Mode shapes and MAC

A fixed constraint was placed at the base of the wing. This mimics a real dragonfly which flaps with a fixed joint at the base. The modal analysis computes the natural frequencies, mode shapes, the |M|, |C| and the response analysis matrices. Ten modes of interest were computed in this experiment. The cut-off frequency was set to 100Hz as a constraint for the simulation results. A lumped mass representation is used with an allocated ratio of 0.2 percentage of data storage (S. Combes, 2003).

Correlation analysis of the similar mode shapes between the detailed and simplified model were carried out. MAC (Modal assurance criterion) requires mode shape data from two similar modes of the structure. Due to the large size of the finite element models in terms of their number of nodes, it is not practically possible to include all the nodes into analysis. Therefore 30 nodes were chosen, along the center of the wing span, at an interval of 0.0002 m (distance between each node) were chosen as the representative of the mode shape. The modal assurance criterion was calculated based on the mode shapes obtained from the simulation results which will be discussed in Chapter 3. Mode was calculated using MathCAD Prime Express 3.0 (Parametric Technology Corporation, 2013) based on this formula:

$$MAC_n = \frac{(U_n{}^T . D_n{}^T)^2}{(U_n{}^T . U_n).(D_n{}^T . D_n)} \tag{3.23}$$

where U_n stands for detailed mode shape matrix of the n^{th} similar mode, D_n stands for the simplified mode shape matrix of the n^{th} similar mode, $U_n{}^T$ and $D_n{}^T$ is the transpose of the detailed and simplified mode shape matrices respectively and MAC_n is the value for the n^{th} similar mode shape (the dots represent multiplying these variables).

3.5 Artificial wing frames and nano-composite chitosan membrane

Several geometrically identical wings were fabricated based on the simplified model created. The frames were fabricated from seven different materials: stainless steel (Type 321), balsa wood, black graphite carbon fiber laminates, red prepreg fiberglass laminates, polylactic acid (PLA), acrylic sheet and acrylonitrile butadiene-styrene (ABS). Three samples of each wing type were tested to determine their tensile stress and bending performance. The same nano-composite was used as a membrane for each wing frame (which will be discussed in section 3.5.8). The mechanical properties of these materials are as stated in Table 3.2. The compromise between minimizing the weight and maintaining adequate tensile and bending stresss are critical for BMAV wings.

Table 3.2: Mechanical properties of frame structure materials (David 2014, D. Akin et al 2014, Arcy, 1961, Shyy, 2010, Rahman, 2012, Marcin, 2011, Boeing, 2003 and 2004, Borrega, 2015, Da Silva, 2007, Leban, 2013, and Osei, 2014)

Material	Density (kg/m^3)	Modulus of Elasticity (N/m^2)	Poisson Ratio	Shear Modulus of Elasticity (N/m^2)	Thickness (m)
Stainless steel (Type 321)	7920.0	1.90×10^{11}	0.3	7.7×10^{10}	0.01
Balsa wood	130.0	3.00×10^{9}	0.5	1.5×10^{8}	0.02
Black graphite carbon fiber	1750.0	2.00×10^{11}	0.5	2.4×10^{11}	4×10^{-4}
Red prepreg fiberglass	1522.4	2.00×10^{11}	0.5	3.0×10^{10}	3×10^{-4}
Polylactic acid (PLA)	1190.0	3.50×10^{9}	0.36	3.37×10^{9}	2×10^{-4}
Acrylic	1180.0	3.32×10^{9}	0.35	6.20×10^{7}	2×10^{-4}
ABS	1050.0	2.80×10^{9}	0.35	1.03×10^{9}	2×10^{-4}

3.5.1 Fabrication of stainless steel (Type 321) wing frames

(a) (b)

Figure 3.4: Stainless steel type 321 wing frames; a) forewing, b) hindwing

Stainless steel (Type 321) is in the high carbon grade category, meaning that it contains a minimum and maximum of 0.04% and 0.10% carbon, respectively. Higher carbon helps the material retain stress at extreme temperatures. Type 321 is commonly used in aircraft applications; because it is low in density (e.g. relative light weight) and high temperature resistance. In our experiment, the stainless steel was subjected to solution annealing. This is a common process done to ensure the smoothness of the grain structure. This means only the carbides which may have precipitated to the grain boundaries are dispersed into the metal matrix by the annealing process. Type 321 stainless steel offer higher creep and stress rupture properties.

The stainless steel wing frames were laser cut from sheet metal. These frames were then coated with an anti-rust layer and spray painted using an acrylic lacquer spray. This was necessary because the nano-composite film membrane will expose the wing frame to oxidation. This is because the film contains concentrated glacial acetic acid and tannic acid as a cross-linker. The anti-rust layer and acrylic lacquer spray hinder the oxidation due to the presence of the acids. Oxidation is visibly indicated by purple blotches appearing on the frame. After these processes, the frames were then immersed in the nano-composite suspension which formed a film membrane coating the entire wing, as previously described. Figure 3.4 shows the finished stainless steel wings.

3.5.2 Fabrication of balsa wood wing frames

Balsa wood is the most widely-used material used in hobby remote-controlled aircraft. This is because of its extremely low density (making it very lightweight) and high mechanical stress. Balsa wood was chosen for this study because it represents a minimum weight solution. The balsa wood wing frames were cut manually with wood carving knives and then immersed into the nano-composite solution. Figure 3.5 shows the finished balsa wood wings.

(a)

(b)

Figure 3.5: Balsa wood wing frames; a) forewing, b) hindwing

3.5.3 Fabrication of black graphite carbon fiber wing frames

Black graphite carbon fiber sheets were purchased and visually inspected to make certain they were uniform in appearance and free from foreign material. The specifications are listed in Table 3.3.

Table 3.3: Specifications of black graphite carbon fiber

Thickness	0.04 mm
Carbon yarn spacing	Four per 0.45 kilograms per strand
Warp tracer weave spacing	0.3 ± 1 m across the fabric width
Fill tracer weave spacing	0.6 ± 1 m apart
Length to diameter ratio (L/D) (See Figure 3.6)	> 10

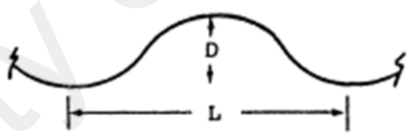

Figure 3.6: Waviness of carbon fiber yarns

The woven laminate was hardened using an epoxy resin with a hardener (Araldite rapid kit). Both epoxy resin and hardener were mixed with a ratio of 1:1 and then applied evenly to the laminate in a thin layer. The laminate was then left to cure in a Memmert UNB 300 convection oven for about two hours at a constant temperature of 45°C. The forewing and hindwing shapes were then carved out of the hardened laminates manually with a knife, using the stainless steel wings as a reference. The only difference between the black graphite wings and the others, were that the inner gap regions were not carved out according to the simplified model. Attempts to do so proved impossible, because it resulted in delamination of the material. However, the overall size and shape of these wings are the

(a) (b)

Figure 3.7: Black graphite carbon fiber wing frames; a) forewing, b) hindwing

same as the others. Figure 3.7 shows the finished black graphite carbon fiber wings.

3.5.4 Fabrication of red prepreg fiberglass wing frames

Red prepreg fiberglass plies with a thickness of 0.03mm were purchased and visually inspected. After curing, the red prepreg fiberglass exhibits a plastic-like characteristic unlike carbon fiber which will retain its strand-like properties. This increases the chance of delamination if a resin and hardener is not applied. The red prepreg fiberglass (after curing) does not require an extra application of resin or hardener. In order to create the wing frame structure, the material was warmed as necessary to enable easier manual carving with a knife. Figure 3.8 shows the finished red prepreg fiberglass wings.

(a) (b)

Figure 3.8: Red pre-preg fiberglass wing models after immersion in chitosan nano-composite solutions; a) forewing, b) hindwing

3.5.5. Fabrication of polylactic acid (PLA) wing frames

The PLA wings were fabricated using a Maker Bot Replicator 2X 3D printer. PLA is chosen for its biodegradability, lightweight, flexibility and elasticity (Joong, 2013). The fabricated PLA wing models are shown in Figure 3.9.

(a) (b)

Figure 3.9: PLA wing models after immersion in chitosan nano-composite solutions; a) forewing, b) hindwing

3.5.6 Fabrication of acrylic wing frames

The acrylic wings were fabricated using micro laser machining. Acrylic or polyacrylate are generally known for their resistance to breakage, elasticity and flexibility (David, 2014). Fabricated acrylic wing models are as shown in Figure 3.10.

(a) **(b)**

Figure 3.10: Acrylic wing models after immersion in chitosan nano-composite solutions; a) forewing, b) hindwing

3.5.7 Fabrication of acrylonitrile butadiene styrene (ABS) wing frames

Models made out of ABS are constructed from a thermoplastic. ABS is very useful for functional applications because it matches 80% of the properties of the real injected production material. ABS models are very accurate and have intermediate level of printed details. You have a lot of freedom for the design of your model. However, the surface quality of the models is rougher compared to other materials. The ABS wings were fabricated using a Maker Bot Replicator 2X 3D printer. ABS is chosen due to its stress, flexibility, and machinability (Hwan, 2012). The fabricated ABS wings are shown in Figure 3.11.

(a) (b)

Figure 3.11: ABS wing models after immersion in chitosan nano-composite solutions; a) forewing, b) hindwing

3.5.8 Chitosan nano-composite solution (membrane)

The chitosan nano-composite suspension as mentioned earlier was made up of a chitosan suspension reinforced with nano-sized chitin whiskers and cross-linked using tannic acid. This nano-composite film was processed by our research team for this specific purpose and is featured in another article (Rubentheren et al, 2015). The suspension was transformed into a thin 3 mm film by the casting evaporation method. This film was chosen because it closely mimics the material properties of a dragonfly wing membrane. The mechanical properties and water resistivity of chitosan film can be controlled by the addition of chitin whiskers and tannic acid as a cross-linker. Utilizing nano-sized whiskers as a filler material elevates the composite film's mechanical property (rigidity). A crosslinking agent is also added to alter the mechanical properties of the film created. Tannic acid is fully biodegradable and less expensive to produce, compared to the other chemical derivatives. Tannic acid also has a high antioxidant capacity and can interact with other biological macro-molecules. Addition of tannic acid as a cross-linking agent reduces the swelling behavior, solubility and the rigidity of the nano-composite film. In order to ensure that the immersion is uniform, the structure was submerged in the solution. This also ensures that both sides of the frame structure are evenly coated with the solution. Once cured, the film created a shiny, transparent film layer that adheres firmly to the frame structure.

(a) (b)

Figure 3.12: Wing structure immersed in chitosan nanocomposite solution; (a) fore wing, (b) hind wing

3.6 Numerical Bend-Twist Coupling and Static Stress Simulation Analysis

3.6.1 Numerical bend-twist coupling analysis

The bend-twist coupling is one of the most relevant analyses for a wing cross section. The effect of the bend-twist coupling appears in a wing structure as a link between its two deformation states – bending and torsion. A static bend-twist coupling analysis was performed for further validation of the models created. As previously described, the analysis was set up with a constraint fixed at the base to mimic an actual dragonfly flapping mode. Figure 3.13 shows the placement of constraints for a natural frequency analysis

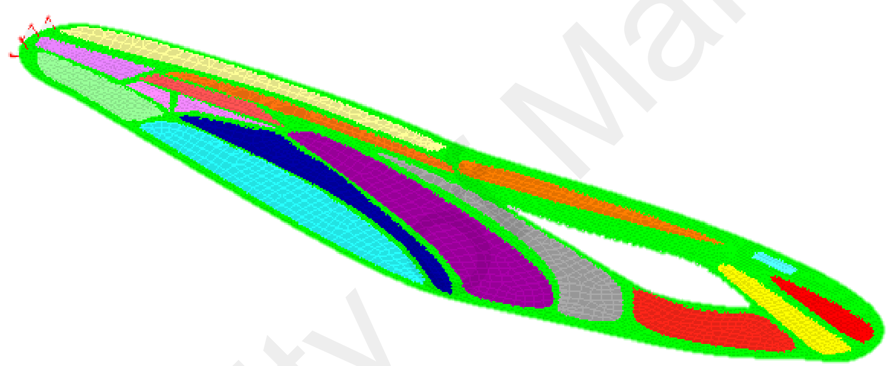

Figure 3.13: Placement of constraints fixed in a natural frequency analysis

3.6.2 Static stress simulation analysis

A fixed constraint was placed at the base of the wing tip to mimic the hinge of an actual dragonfly wing. Nodal forces were applied at the tip of the wing to mimic the tensile and bending test experiments. Simulations were done for all eight wings (forewing and hindwing fabricated from all four materials). In addition, simulated bending and tensile tests were done for the frame structures without the membrane to record the effects of the chitosan nano-composite film on the frame structure. The stresses computed in the static analysis are used to form the stress-dependent contribution to the tangent-stiffness matrix. Static stress analysis, enables the study of stress, strain, displacement, and shear and axial forces that result from static loading. Figure 3.14 shows the static stress simulation model for a static stress analysis. Numerical analysis was not constructed until failure due to the fact that dragonfly wings do not flap until they fail. Hence, a linear model was used.

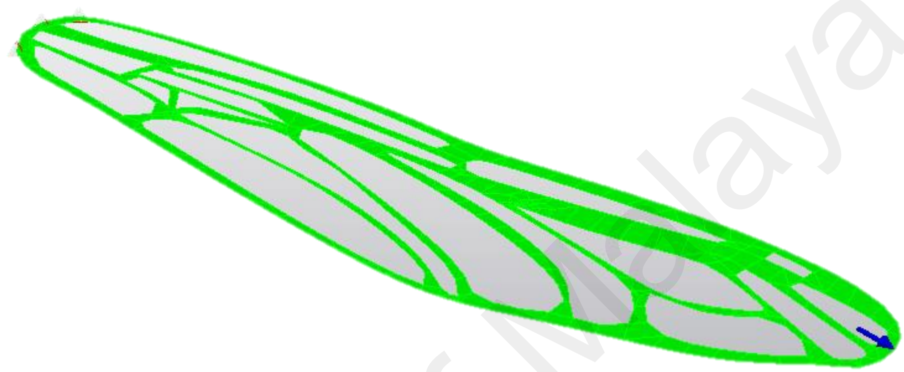

Figure 3.14: Constraints for a static stress analysis

3.7 Experimental Set Up

Tensile and bending experimental tests were done on the physical models using the Instron Universal Testing Machine (Model 5569). Increasing loads were incrementally applied to the wings until they failed. The data was compiled and integrated by Instron MERLIN software. A specific jig was designed for both bending and tensile test to clamp the fabricated models, whereby the slots were used to clamp the thin structures firmly. All testing was repeated three times for each wing type, necessitating the fabrication of three identical copies of each wing type. Since the wing frame test specimen is a sheet-like structure, the same ratio of width-to-gage length (18:18 for forewing and 20:20 for hindwing) was maintained in order to compensate for the elongation that occurs during diffuse necking. ASTM test specifications were followed throughout the experiment. Each base of the wing models were clamped at a fixed point and the tips were clamped at the moving point. The load was then increased gradually with a speed rate of 0.013 m/s. The rate of extension and the stress-strain curve was observed until the wing model experienced a structural failure. This point can be observed in the collected data as a sudden decrease in the load. Data obtained in RAW file (not processed) was then converted to Microsoft Excel for further analysis. The high speed camera imaging technique was then employed after close observation of all these seven materials, and three best materials were chosen based on performances. The main criteria of selection were the ability to withstand high tensile stress and possess a high compression stress vs strain. Due to the complexity of an actual dragonfly wing (due to the corrugations and veins) it was impossible to conduct tensile testing on an actual wing. However, previous research has provided sufficient values to aid in setting a benchmark for the criteria of the suitable material. Referring to previous research, the value of tensile and compression stress for an actual dragonfly wing was found to be 285 MPa and 16.87 GPa, respectively (Rupan et al, 2013). As mentioned earlier, in order to test the aero-elastic properties of the dragonfly wings, the final step of the research was two test it on an actual flapping mechanism. This is a static mechanism which is able to produce a flapping motion frequency up to 250 Hz.

Previous researchers have conducted studies using high speed camera. Gui et al. (2010) applied simple optical modifications to replace an expensive two-camera system for taking stereo videos of fire ant alate wingbeat motion. Many have utilized the high speed camera technique to capture wing motion of birds and insect flights. (Norris 2001; Sudo et al. 2001, 2005; Dalton 2002; Gorman 2003). Recent advances in high-speed imaging technique make it possible to capture insect wing motion not only at high phase resolution but also at high digital resolution, e.g. the Photron Ultima APX high-speed camera used in our lab is capable of capturing partial frames of 1024256 pixels at 8,000 frames per second (fps). High digital resolution and high phase resolution together enable a precise analysis of the wing motion within a wingbeat period. However, at least two images from different view angles, e.g. provided by a stereo imaging system, are necessary to determine the three dimensional shape and orientation of the wing surface. A stereo imaging system requires at least two cameras that view an object from two different directions, and in an ideal situation, these two view directions should be perpendicular to each other, (Sudo et al. 2001, 2005).

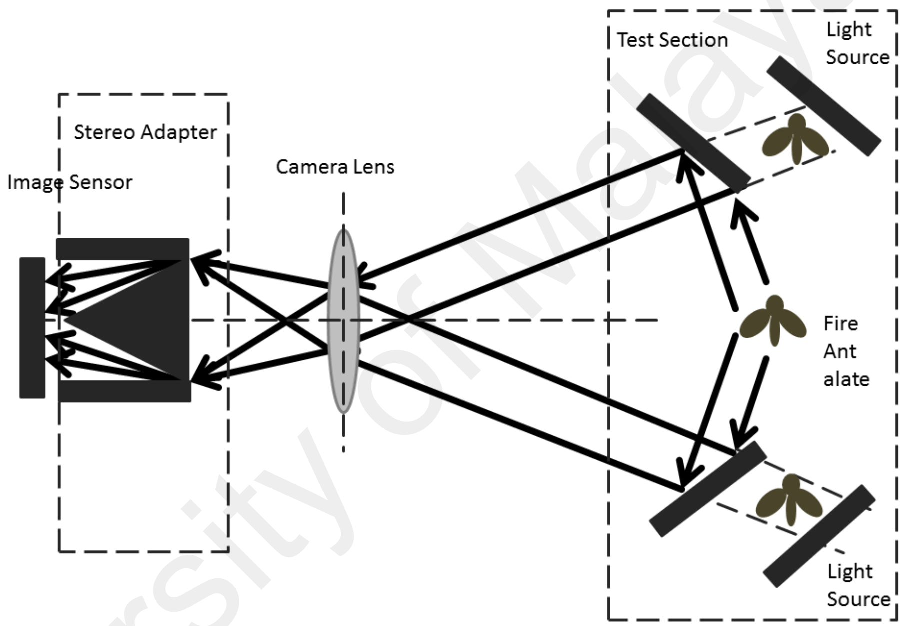

Figure 3.15: Schematic diagram of Gui et al (2010) of fire ant alate wing motion

In order to capture the motion of the wing motion of the wings, two Phantom Miro 310 (Vision Research) high frame rate cameras were used to view the flapping wings from two different directions in Figure 3.15. The camera's high frame rate enables a precise sequence of images to be captured of the flapping wing motion within a single wing beat. Two cameras were necessary in order to determine the three-dimensional shape and orientation of the wing surface (Figure 3.16 (a) and (b)). The cameras were placed perpendicular to one another following the procedures established by Gui et al. (2010).

Both cameras were equipped with a Nikon F lens. A multiple LED lighting system was used to provide sufficient illumination. Imagery was recorded at a resolution of 320 x 240 pixels and a frame rate of 35000 per second, which allowed the wing beat motion to be precisely captured. The motion video was stored in a computer via two high speed Ethernet cables. It was played-back and analyzed using the Vision Research Phantom Camera Control Software (version 2.6.749.0).

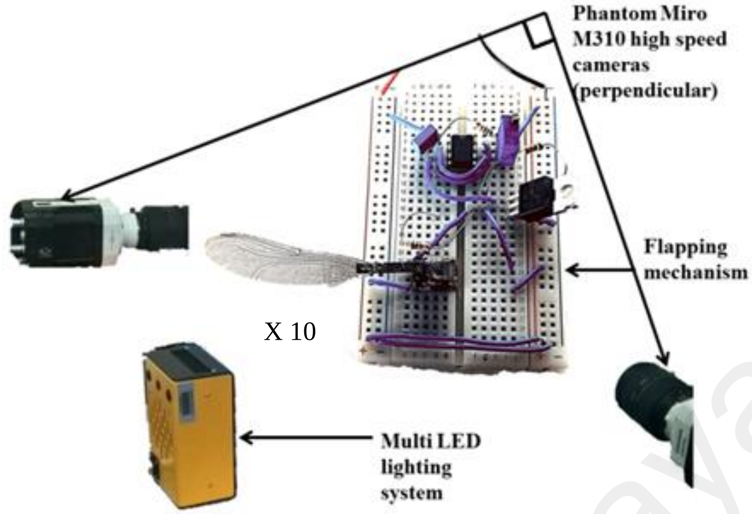

(a)

Figure 3.16: (a) Actual experimental set up of the high speed camera imaging technique, (b) Schematic diagram of the experimental set up

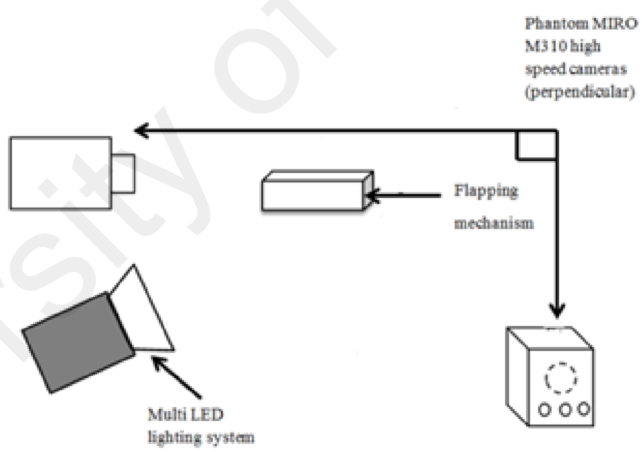

(b)

Figure 3.16: (continued) (a) Actual experimental set up of the high speed camera imaging technique, (b) schematic diagram of the experimental set up

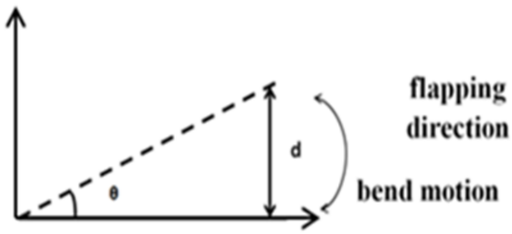

(a)

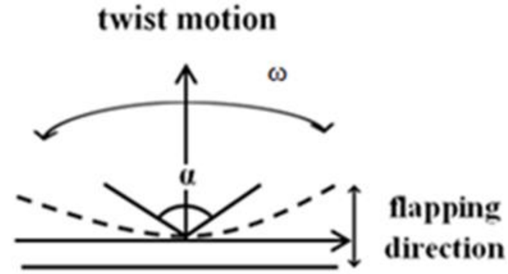

(b)

Figure 3.17: Front view (a) and side view (b) of the wing motion captured and measurement axes.

Measurements were taken using each of the three wings while flapping at varying frequencies: 10, 20, 30, 70, 120, 200 and 250 Hz. Figure 3.17 shows the front and side view of the wing motions that were measured and recorded from captured imagery. Figure 3.17(a) illustrates the bending angle (θ) and displaced distance or deflection (d). Figure 3.17 (b) defines the wing tip angle (α) and the wing tip rotational twist speed (ω).

3.8 Flapping mechanism

The wing flapping mechanism used in this study is an electromagnetic flapping wing actuator. The power supply used in this flapping wing drive is 9 volts DC. A LM555 crystal clock oscillator integrated circuit (shown in Figure 3.18) is used to generate a stable oscillation. The free running frequency and duty cycle are accurately controlled with two resistors and one capacitor. The generated oscillation is fed to a Power MOSFET fast switch. The output of the Power MOSFET is used to actuate the miniature PC Board Relay. The frequency of the switch (corresponding to the wing beat frequency) can be adjusted by a 22 kW potentiometer. Each of the different wings is attached to a flat iron plate (2 mm long and 2.75 mm thick) using super glue. This plate (wing platform) is oscillated by an electromagnetic actuator (3 x 3 mm). Figure 3.18 shows the wing structures attached to the actuator. The plates are attached to the hinge of the wing to mimic the joint of an actual dragonfly. This flapping mechanism is able to create a linear up-down stroke motion at variable wing beat frequencies, up to a maximum frequency of 250 Hz. The flapping degree was set to be 60° which corresponds with an actual dragonfly wing flapping angle during hovering flight (Jane, 2004 and Xinyan, 2008).

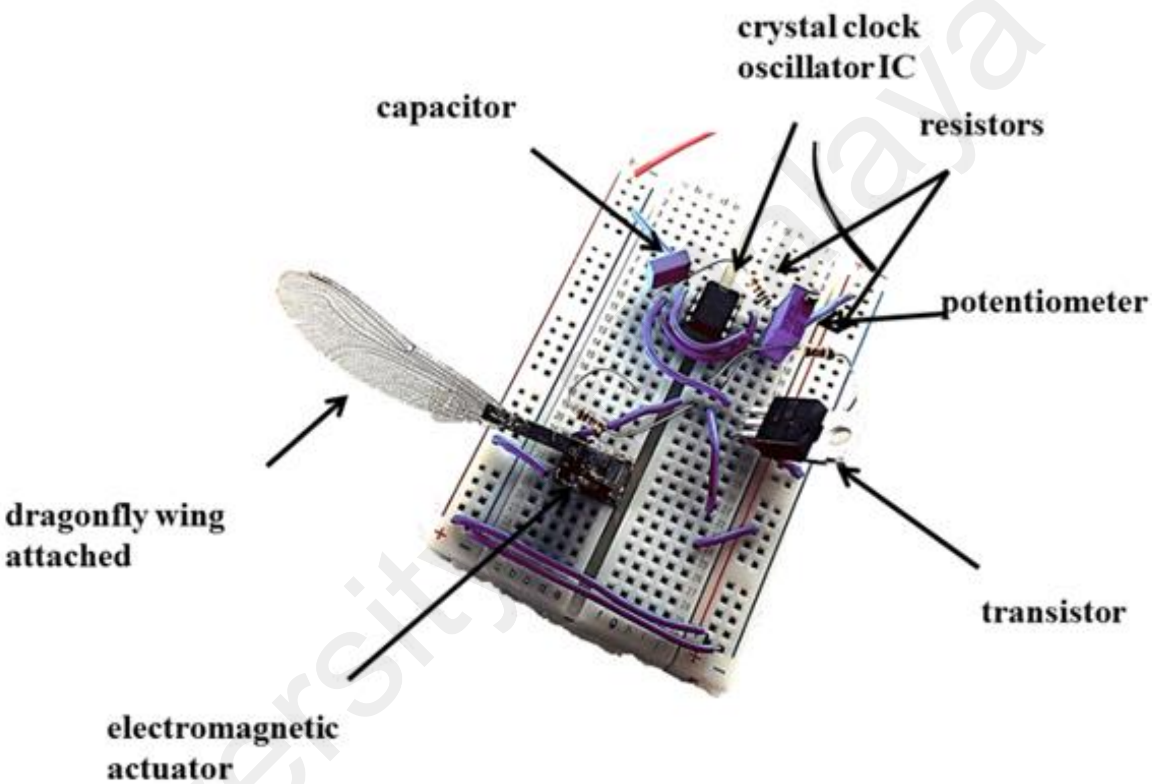

Figure 3.18: Flapping mechanism used in this research

CHAPTER 4: RESULTS AND DISCUSSION

4.1 Introduction

This chapter includes discussion pertaining to the results obtained. It includes the simulation results, the experimental results, application of the chosen wings in a flapping mechanism and the images of this application.

4.2 Simplified model creation

Two models were created for each wing. The first model (or detailed model shown in Figure 3.3) closely approximates the fine detailed structure of an actual dragonfly wing. This was built using the Canny edge detection algorithm previously described in Section 3.3.1. Due to its small size and complexity, this model proved to be too difficult to fabricate using laser micro machining. Therefore a second model (or simplified model) was created that simplifies the structure into its major constituents, by grouping dense patterns and vein structures into single regions. Fabricated simplified model examples are shown (Figure 4.1). These samples were laser cut from thin (1 mm thickness) stainless steel sheet metal. Careful consideration was taken into keeping within machining tolerance, with the objective of fabricating a wing for a BMAV design in the near future. The ratio of the quadrilateral, pentagons and hexagons are 10:30:60 based on observation. Therefore, although the hindwing has a larger area than the forewing, the number of regions created is justified by considering the ratio of patterns. Examples of dragonfly wing patterns can be seen in Figures 4.2 (a) and (b). The costal part of the wing consists of several uniformally-arranged rectangular membrane patterns. These were grouped together in different regions (consisting of 10 to 15 rectangles per region). There are many small, hexagonal membrane patterns at the anal margin and wing tip. These were grouped into several regions (consisting of 30 to 50 patterns per region). Table 4.1 shows a summary comparing the pattern densities of the detailed and simplified models.

(a) (b)

Figure 4.1: Fabricated simplified model (a) Forewing; (b) Hindwing

Table 4.1: Model specifications in terms of number of membranes, density and patterns

CAD model	**Properties**					
	No. membrane regions		**Area (m^2)**		**Average pattern density (region/m^2)**	
	Forewing	Hindwing	Forewing	Hindwing	Forewing	Hindwing
Detailed Model	787	900	0.00055	0.000577	14309	15517
Simplified Model	17	16	0.00055	0.000577	30900	27586

The spatial network analysis method was implemented by dividing the wing model into circles with diameters of 0.00025m and 0.0005 m, for smaller and larger regions respectively. The size of regions correspond to the pattern density in that particular area. Smaller regions are used in higher density areas. The center of the circle was determined by looking at the starting point of a branch of the main vein. Previous research was used as a reference to determine the center of the circle (HuaiHui et al. 2013).

(a) (b)

Figure 4.2: Typical dragonfly wing membrane pattern arrangement

Figures 4.2 (a) and (b) shows membrane patterns that are typical of dragonfly wings. A number of proximate cells are located between two main veins and arranged in one row to form quadrilateral shapes. Sometimes there are two rows of cells, intercalated between a pair of main veins. As shown in Figure. 4.2 (b) in this case, one row will fit into another at an angle of 120° as a result of coequal tension, but both cells are at right angles when it meets the main vein as in the former case. For numerous rows of cells, all the angles between them tend to be co-equal angles of 120°, and hence the cells resolve into a hexagonal or polygonal meshwork. The cell arrangement in dragonfly wings was explained through soap bubble experiment (Arcy,1961). When four soap bubbles meet in a plane, they arrange in symmetrical ways either with four or five partition-walls intersecting at right angles. Five partition walls are known to be unstable. The point where the patterns branch into four to five patterns was determined to be the center of the circle. The hindwing of a dragonfly is slightly broader in size compared to the forewing, but the pattern it comprises remains the same (e.g. quadrilateral, pentagons and hexagons). The number of patterns that make a region is therefore drawn by observation with the appropriate ratio (10:30:60) applied to it.

Figure 3.2 in the previous section, shows how the circles were placed on the detailed model in order to formulate what will become the simplified model. The nodes (that determine the center of each proximity circle) were placed at branching points, according to the soap bubble theory. A past article reports that a good index value should be close to 1.0 (de Smith, 2007). This value indicates the compactness of the geometric pattern enclosed by the circle. If the index is within an acceptable range, this validates the creation of a polygonal region within the selected area. The proximity index for the circles were found (from Equation 10) to be between 0.66 to 0.83.

It is difficult to fit circles into regions near edges of the wing that are highly cambered (Figure 4.3). Trying to do so will either create large gaps or lap over the edge. Because of this, point clouds were used instead of circles in these regions. The Canny edge detection algorithm played a pivotal role in determining the shape of a region by highlighting the vein with the strongest edge from the orientation of point clouds. The shape of the bounded region was drawn by connecting these strong edges (Figure 4.3).

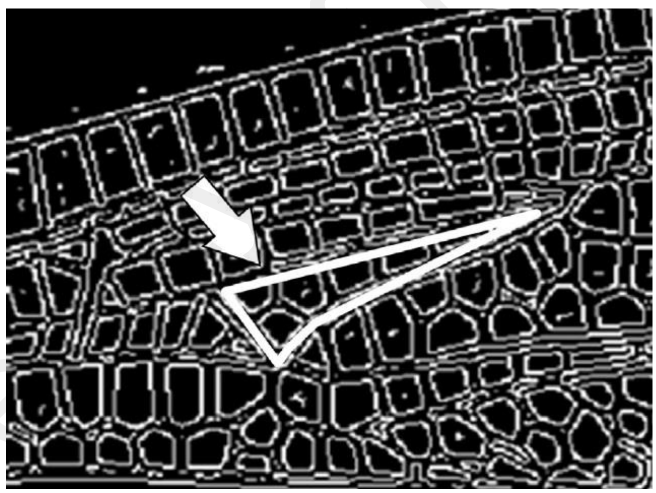

Figure 4.3: Example of connecting strong edges using cloud points

Figures 4.4 (a) and (b) shows the resulting simplified model of the forewing and hindwing, respectively. The overall shape and size of the detailed and simplified model are the same, only the internal vein and membrane pattern was redesigned.

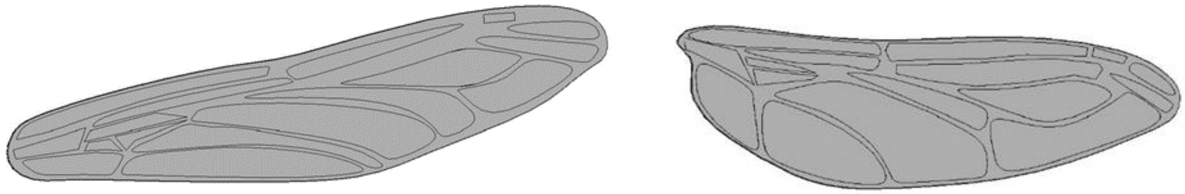

(a) (b)

Figure 4.4: Simplified models, (a) forewing, (b) hindwing

4.3 Mode shape analysis and MAC

The mode shape similarities are shown in Figures 4.5 and 4.6. Out of ten mode shapes computed, the five best matching mode shapes were selected and compared between these two models. The modes were distinguished by the deflection shape of the structure. Higher mode shapes were included because these mode shapes will be able to determine the flutter speed in future work. Therefore Figures 4.5 and 4.6 also include the higher mode shape comparison. The natural modal frequencies were also listed in Figures 4.5 and 4.6. It is known from the structural dynamics that natural frequency is directly proportional to the square root of the stiffness and inversely proportional to square root of the mass. Due to the minimization of patterns (reduction of number of regions), the overall mass has been minimized with the detailed model having a mass of 0.0216 kg and the simplified model having a mass of 0.0182 kg. This reduction has been achieved by utilizing spatial network analysis. Minimization of mass and reduction in stiffness will result in an increase of natural frequency and the results shows a good agreement with this. The increase in natural frequency was in the range of 3-10% for all simplified models.

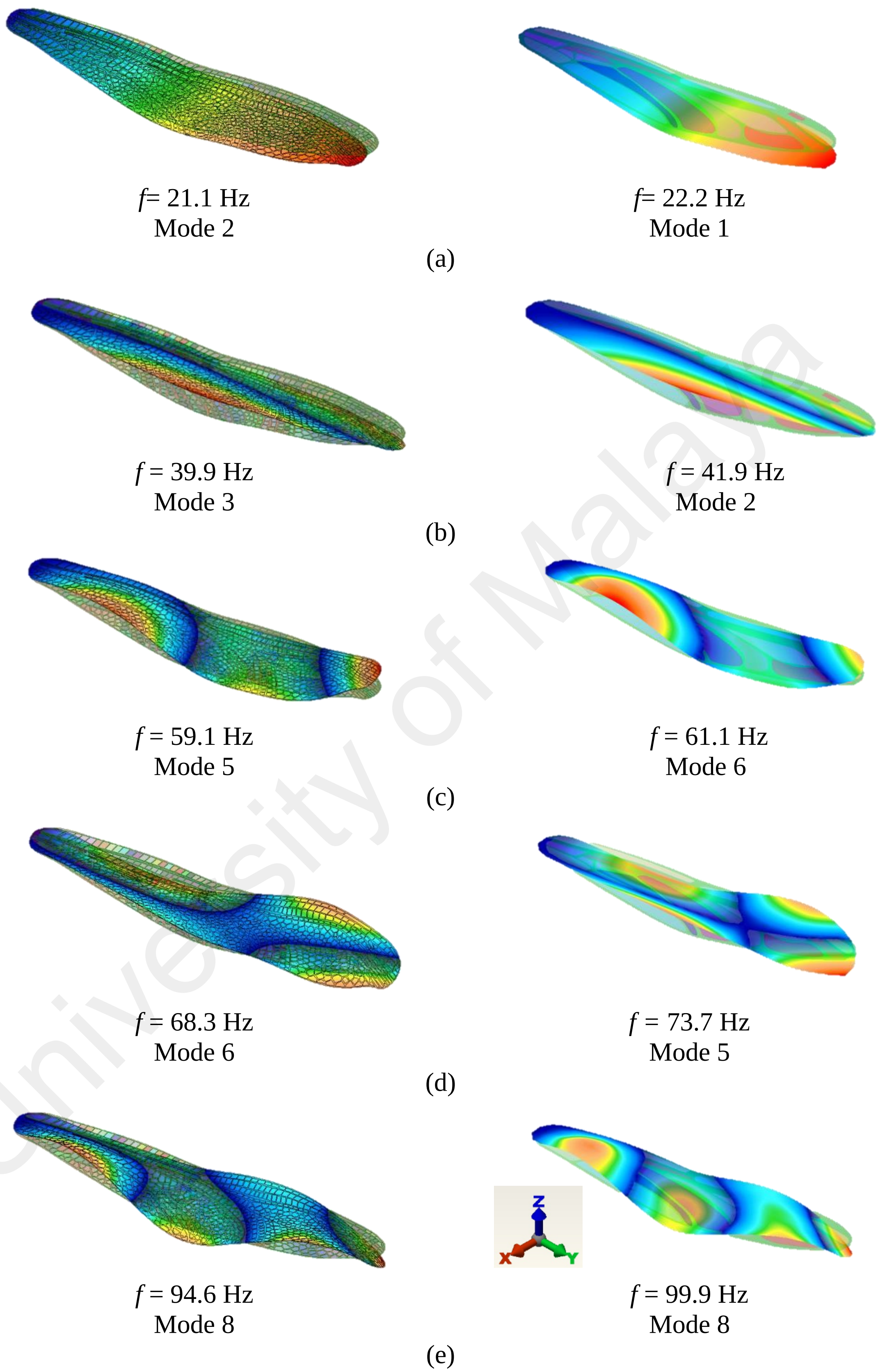

Figure 4.5: Mode shapes and corresponding natural frequencies for both detailed (left) and simplified models (right) : forewing

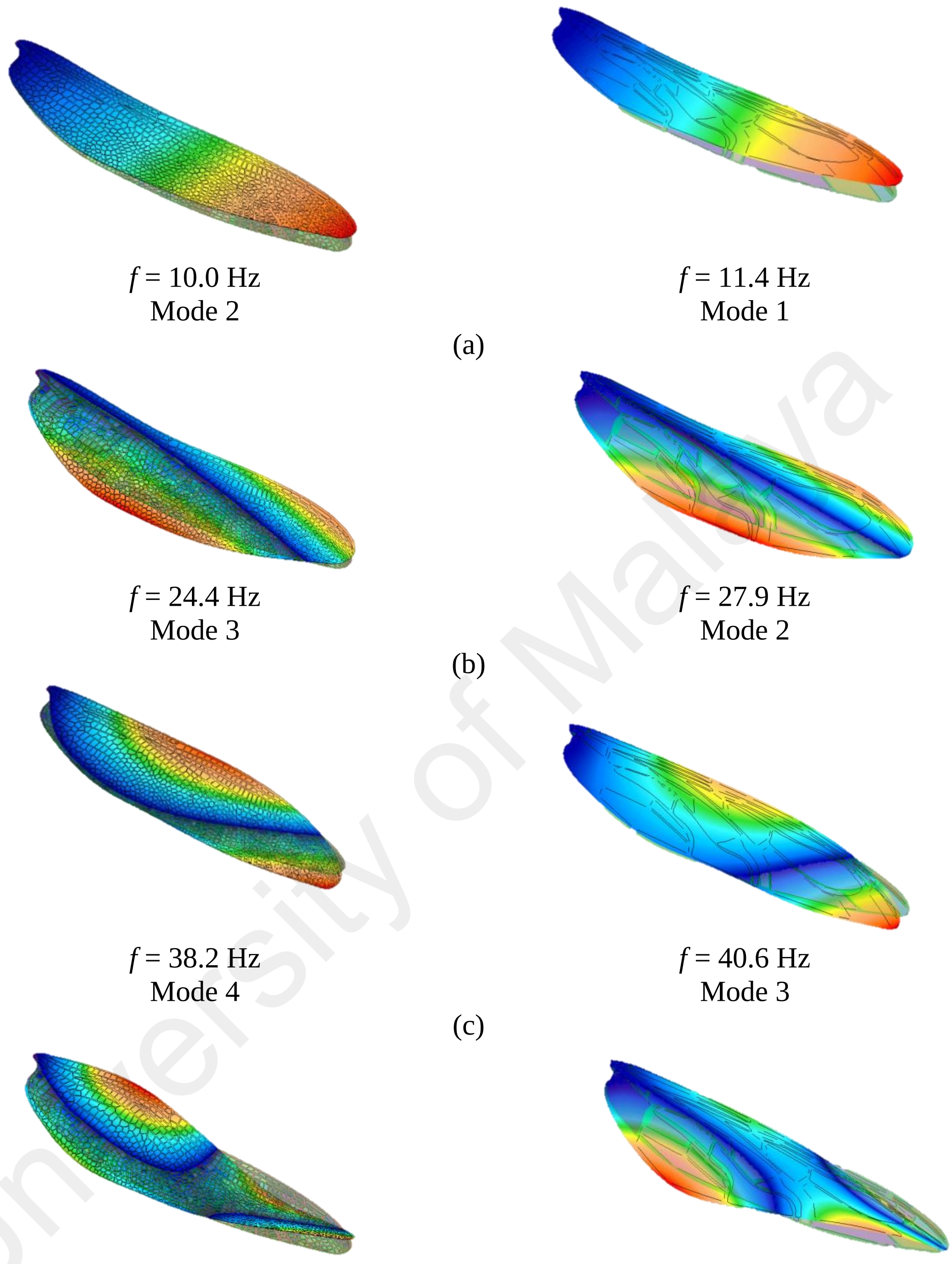

Figure 4.6: Similar mode shapes and corresponding natural frequencies for both detailed (left) and simplified models (right) : hindwing

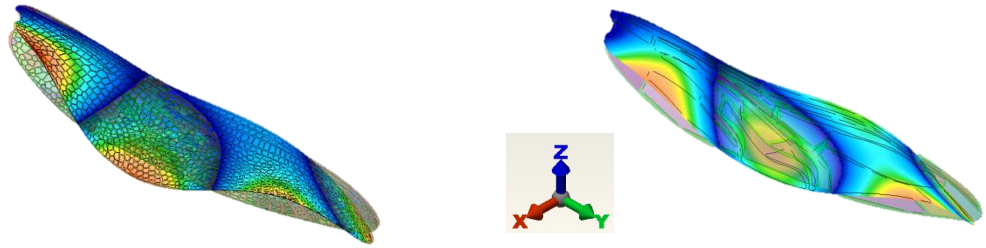

f = 62.9 Hz
Mode 7

f = 65.6 Hz
Mode 7

(e)

Figure 4.6: (continued) Similar mode shapes and corresponding natural frequencies for both detailed (left) and simplified models (right) : hindwing

The slight difference in natural frequency between the models is due to the fact that there are fewer membranes in the simplified models, which reduces the torsional rigidity of the wing (HuaiHui, 2013). The calculated natural frequency and deformed modals are in accord with previous vibration test experiments that have been conducted (Ching, 2009, Rajabi, 2011). The mode shapes of the wings are defined as: up-down flapping, bending, and twisting (Rajabi, 2011). Figures 4.5 (a) and 4.6 (a), shows the detailed wing model with a prominent up-down flapping mode; a bend upwards at the posterior main vein; and a twist at the group of transverse vein at the wing base. Similarly, Figures 4.5 (c), (d) and 4.6 (c), (d) shows the detailed wing model with up-down flapping and a significant bending and twisting along the anterior and posterior of the group of main veins. Figures 4.5 (e) and 4.6 (e) shows that the simplified models exhibit a slight up-down flapping with a clear bend at the wing tip. This agrees with previous research conclusions that the membranes increase wing component rigidity (Du Mont, 2009, Combes, 2003, Tanaka and Shyy, 2010).

The MAC values from Equation (23) obtained for the five compared mode shapes are shown in Table 4.2. A MAC value indicates that a unique mode shape should ideally be 1 and it reduces to 0 with reducing degree of correlation.

Table 4.2: MAC values for all five compared mode shapes for both forewing and hindwing

*n*th mode shape	1	2	3	4	5
Forewing	0.709	0.987	0.944	0.664	0.909
Hindwing	0.935	0.948	0.768	0.622	0.602

The values shown in Table 4.2 prove that both the detailed and simplified models have a close degree of correlation which further validates the simplifed model (Rahman, 2012). The range of accepted values would be from 0.65 - 0.9 (values which are closer to 1). It can be noted that there is a slight difference in mode no 4 which is negligible (0.622) since the percentage difference is 4.6%.

4.4 Numerical bend-twist coupling analysis

Anisotropic materials have elastic couplings related to shear and in-plane/out plane/out-of-plane behavior. Most often undesired behavior include warping. Some of the elastic couplings include bending that induces twist. (bend-twist coupling). Elastic coupling in structures is a direct effect of having different laminate modulus in different directions, known as anisotropy. The bend-twist couplings in laminates are created by a variation in thickness (plane modulus) which is not balanced by an opposing coupling effect of another ply. Dragonfly wings are anisotropic in nature which means that there is a significant amount of bend-twist effect in them. In order to be structurally correct the simplified wing model has to possess the same equivalent axial and bending stiffness as the detailed (original) wing in order to properly predict wing deflections and stresses. Ideally, the wing tip deflection of the simplified model should match the deflection of the real wing, for any given applied load.

By graphically comparing the detailed and simplified model plots (Figures 4.7 and 4.8) it could be observed that the twist angles for the simplified models are higher (approximately 3-5%) than those of the detailed model. Moreover, the trend of deflection (bending) is the same in all plots confirming the observation. The basal leading edge of dragonfly wings are highly corrugated structures, which improves its flexural and bending stiffness (Combes, 2003 and Tanaka, 2010). This prevents chord-wise flattening especially at the main veins. None of our models includes this complexity. The lack of corrugated edges will generally not be an issue for a BMAV wing if rigid, metallic structures are used, rather than the chitin-based structures in actual dragonfly wings. Studies have shown that the corrugation has only a slight effect on the wing's aerodynamics, because the scale of corrugation is small compared to the separated flow region and size of the leading edge vortex (Xue Li, 2009). Therefore, corrugated wings will provide structural benefits without significant effect on aerodynamic lift production.

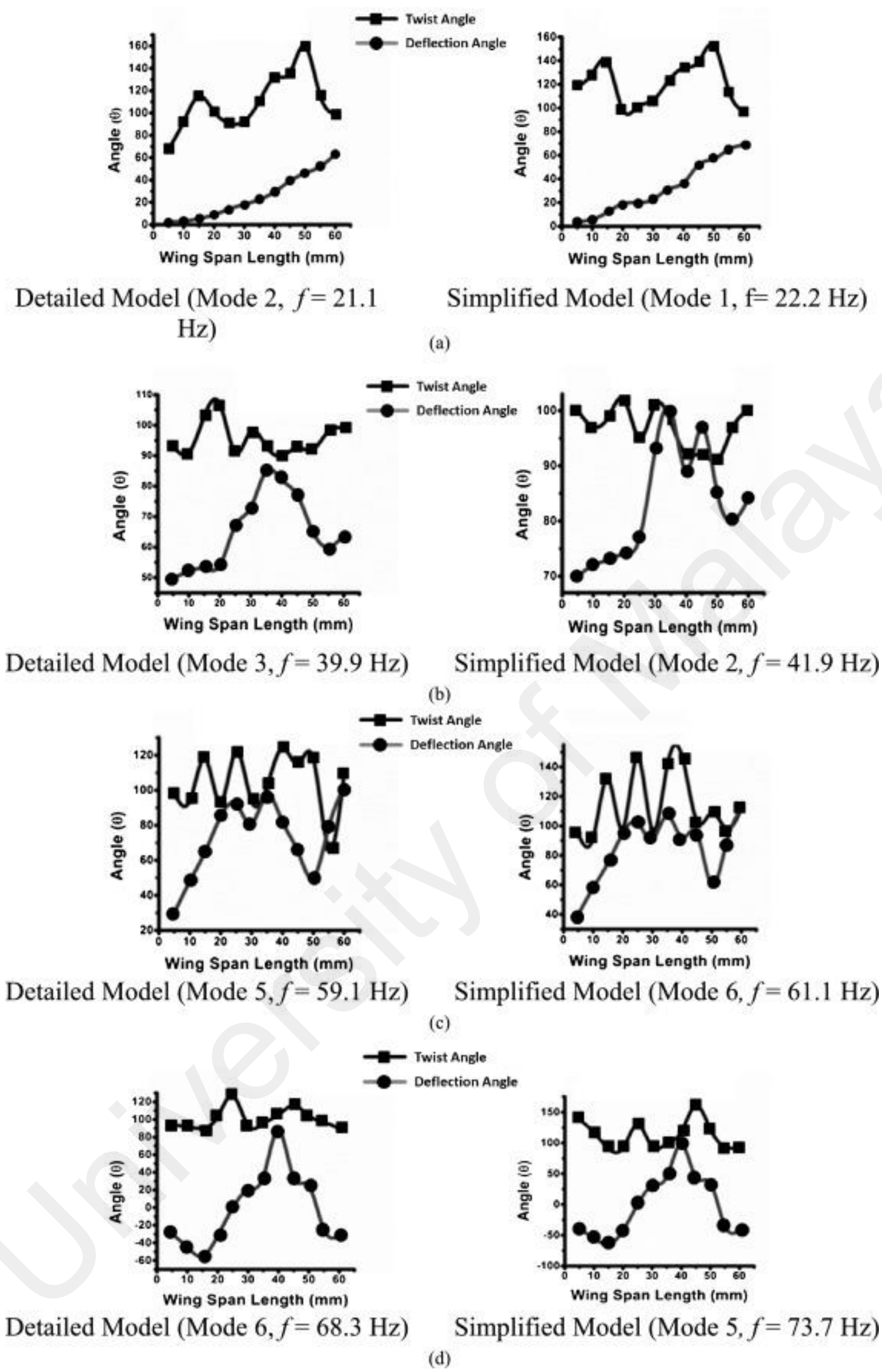

Figure 4.7: The static bend-twist coupling graph of both detailed and simplified models; forewing

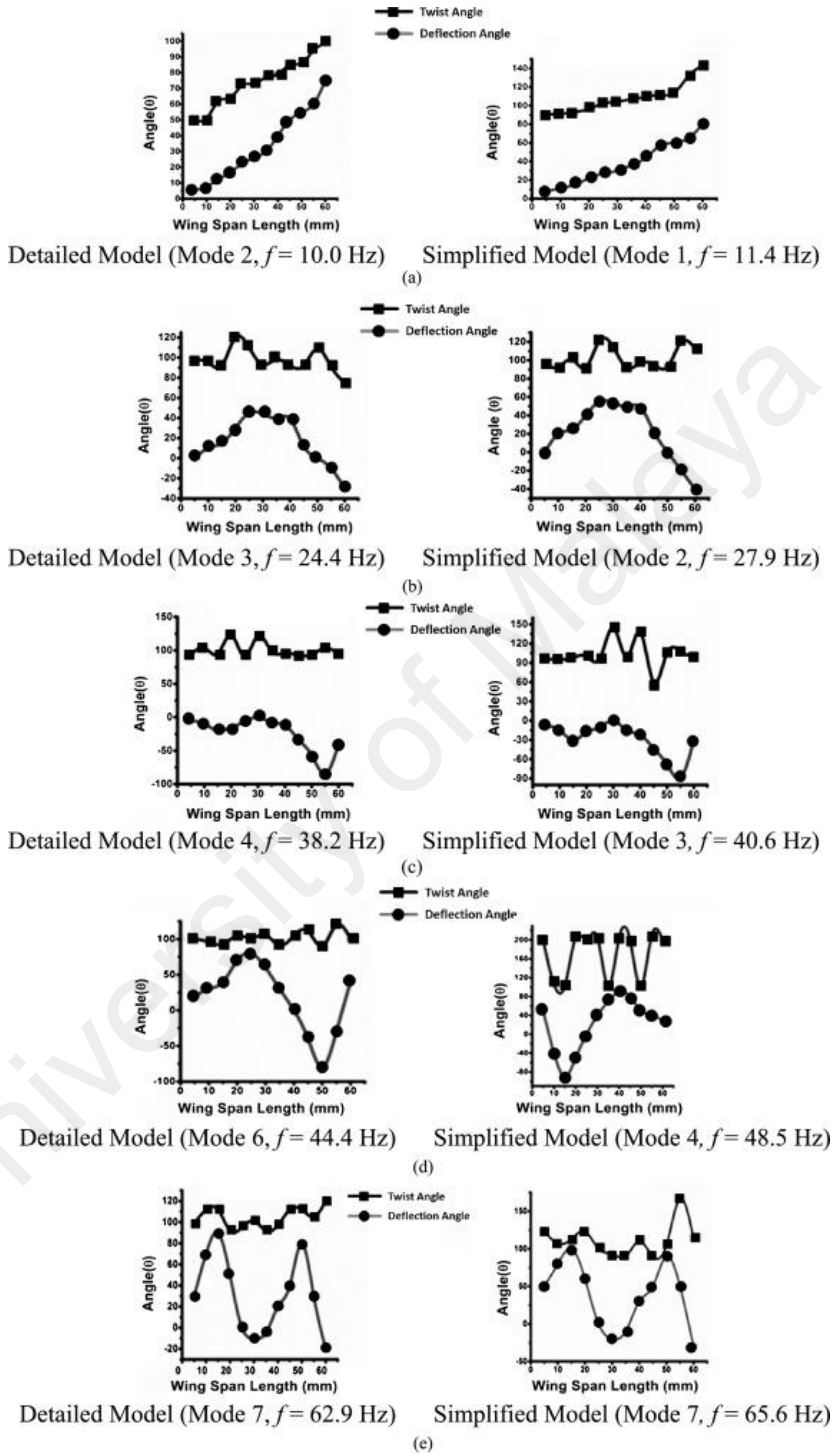

Figure 4.8: The static bend-twist coupling graph of both detailed and simplified models; hindwing

4.5 Tensile test simulation results

Simulation results were obtained before the experiments were conducted. Both tensile and bending experiment results were analyzed and the stress distribution was observed. Simulation tensile test results were observed and critical or high stress areas were marked as points of fractures. These results helped in identifying the weak areas (regions) of the wing models of different materials and the maximum stress that the models could withstand.

4.5.1 Tensile test simulation results (wing frames without membrane)

The first experimental tests involved the wing frame structures without their membranes. (The material specifications for these models are stated in Table 3.2.) Figure 4.9 shows the von Mises stress results of all the seven different frame structures. The 'max' (maximum) and 'min' (minimum) pointers indicate the area where the stress is the highest. The highest stress in the forewing recorded for stainless steel (Type 321), balsa wood, black graphite carbon fiber,red prepreg fiberglass, PLA, acrylic and ABS is: 2.54N/mm^2, 0.04N/mm^2, 2.03 N/mm^2, 0.03 N/mm^2, 13 N/mm^2, 17 N/mm^2, 23 N/mm^2 respectively. A close observation from the results shows that the high stress point for all seven materials, except for balsa wood and acrylic, occurs in the same region. This region is located where the surface-to-area ratio is at its minimum value. The maximum stress on the balsa wood wing occurred at the grip point. Based on previous studies (Da Silva, 2007), balsa wood, and acrylic to a certain extent, under compression in the axial direction exhibits a linearly elastic regime that terminates by the initiation of failure in the form of localized kinking.

Geometric imperfections in the form of fiber waviness, and failure was found to lead to kink bands with distinct orientations and widths (Kyriakides, 1995). Subsequently, under displacement-controlled compression, a stress plateau is traced that is associated with the gradual spreading of crushing of the cells through the material. The material is less stiff (i.e. weaker) in the tangential and radial directions. Compression in these directions crushes the tracheids (phloem of the wood) laterally. Figure 4.10 shows the results for the hindwing. The maximum stress occurs in approximately the same location for all the wing frame structures. This region corresponds with the minimum surface-to-area ratio. The minimum stress also occurs in a similar location for all of the wing frames, except for the balsa wood and acrylic frame. The readings are 2.31 N/mm^2, 0.08 N/mm^2, 1.39 N/mm^2, 0.02 N/mm^2, 12 N/mm^2, 17 N/mm^2 and 24 N/mm^2 for stainless steel (Type 321), balsa wood, black graphite carbon fiber and red prepreg fiberglass, PLA, acrylic and ABS respectively. The minimum stress for the balsa wood and acrylic frame occurs in the cambered edge, because it experiences the lowest compression stress. This has been observed for balsa wood in past studies (Borrega, 2015, Osei, 2013 and 2014)

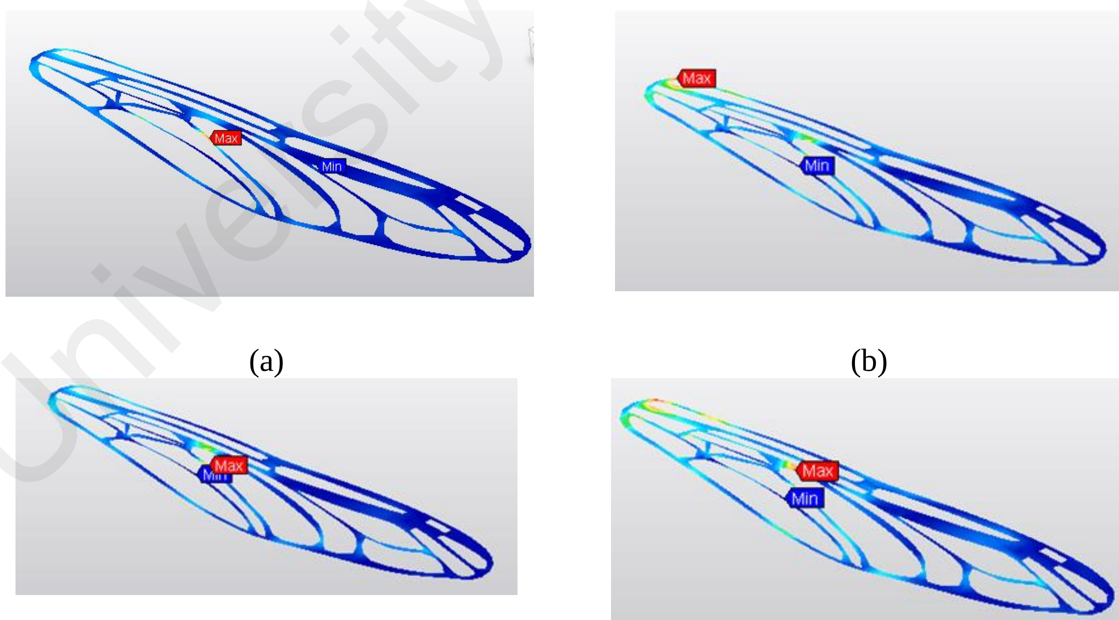

(a) (b)

(c) (d)

Figure 4.9: Von Mises stress simulation results of different forewing frame structures; (a) stainless steel (Type 321), (b) balsa wood, (c) black graphite carbon fiber, (d) red prepreg fiberglass e) PLA, f) acrylic, g) ABS

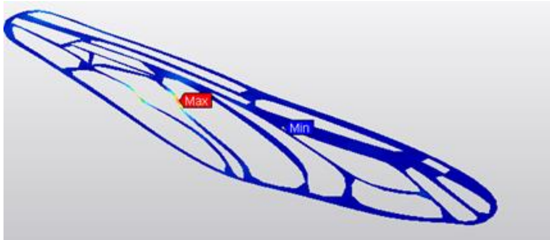

(e)

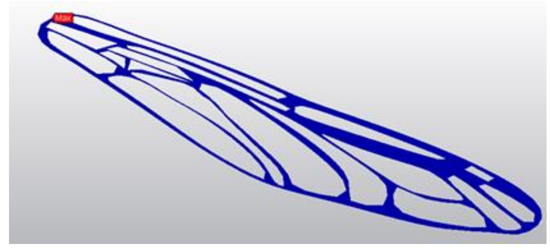

(f)

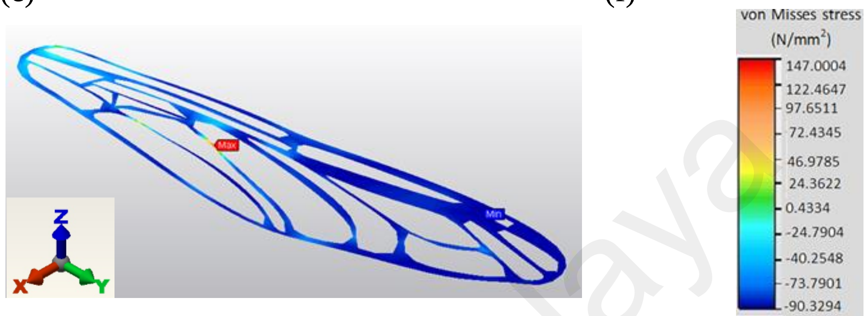

(g)

Figure 4.9 (continued): Von Mises stress simulation results of different forewing frame structures; (a) stainless steel (Type 321), (b) balsa wood, (c) black graphite carbon fiber, (d) red prepreg fiberglass e) PLA, f) acrylic, g) ABS

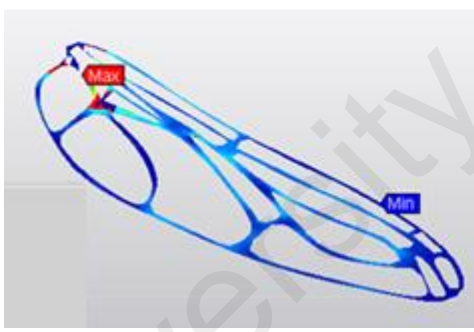

(a)

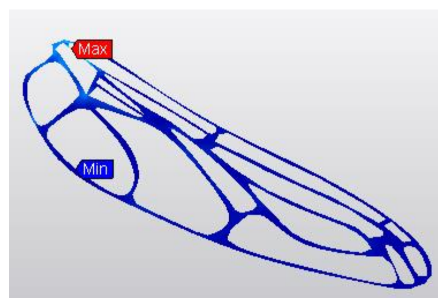

(b)

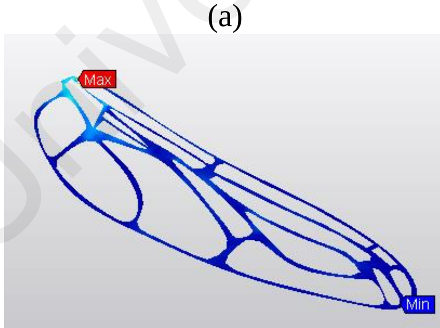

(c)

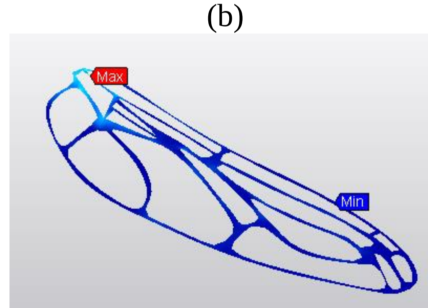

(d)

Figure 4.10: Von Mises stress simulation results of different forewing frame structures; (a) stainless steel (Type 321), (b) balsa wood, (c) black graphite carbon fiber, (d) red prepreg fiberglass, e) PLA, f) acrylic, g) ABS

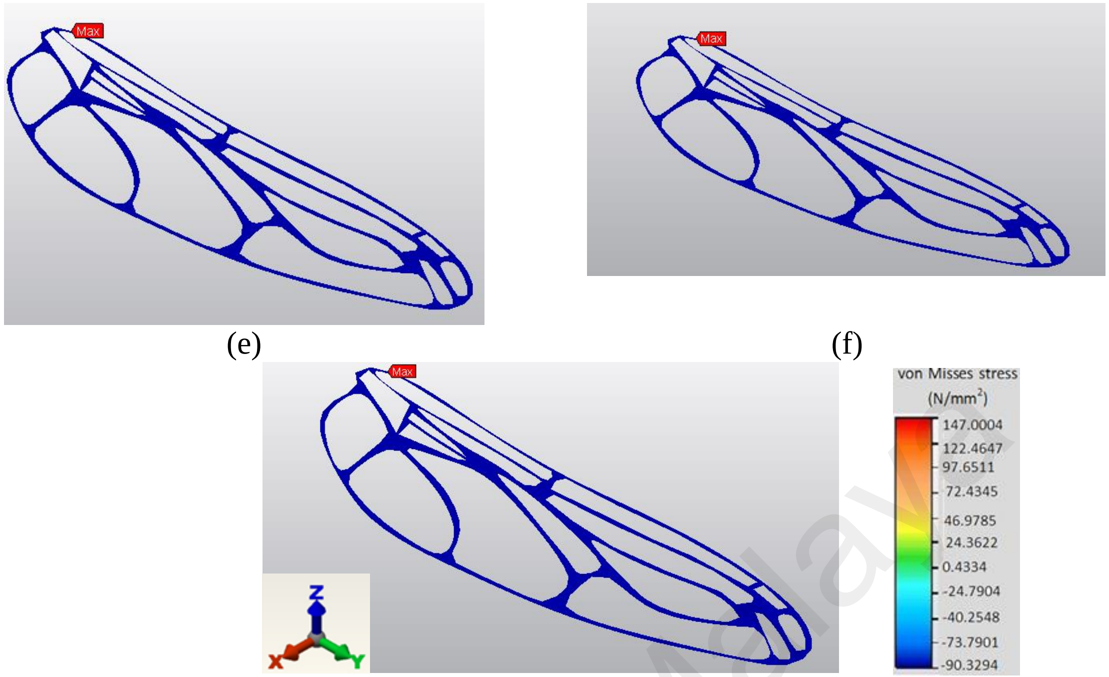

(g)

Figure 4.10 (continued): Von Mises stress simulation results of different forewing frame structures; (a) stainless steel (Type 321), (b) balsa wood, (c) black graphite carbon fiber, (d) red prepreg fiberglass, e) PLA, f) acrylic, g) ABS

4.5.2 Tensile test simulation results (wing frames with membrane)

Simulation results were also obtained for the wing frames with their membranes. Figure 4.11 shows the forewing models of all four materials. Based on Figure 4.11, the maximum von Mises stress occurs at approximately the same location for all seven materials. This location is different from the models without membranes (Figure 4.9). However, the highest stresses occur again in regions where the surface-to-area ratio is minimum. An exception is seen in the wing frame made of black graphite carbon fiber laminate, where the maximum stress occurs in the cambered edge of the wing. This is due to the fact that carbon fiber undergoes delamination at areas where the kinks and curves are located. (Tamilarasan, 2015). The region where maximum stress occurs shows a potential area of delamination. The maximum stress recorded is: 2.05 N/mm^2, 0.097 N/mm^2, 49.3 $N/mm^{2,}$ 2.10 N/mm^2, 14.77 N/mm^2, 17.29 N/mm^2, and 24.23 N/mm^2 for stainless steel (Type 321), balsa wood, black graphite carbon fiber, red prepreg fiberglass, PLA, acrylic and ABS, respectively.

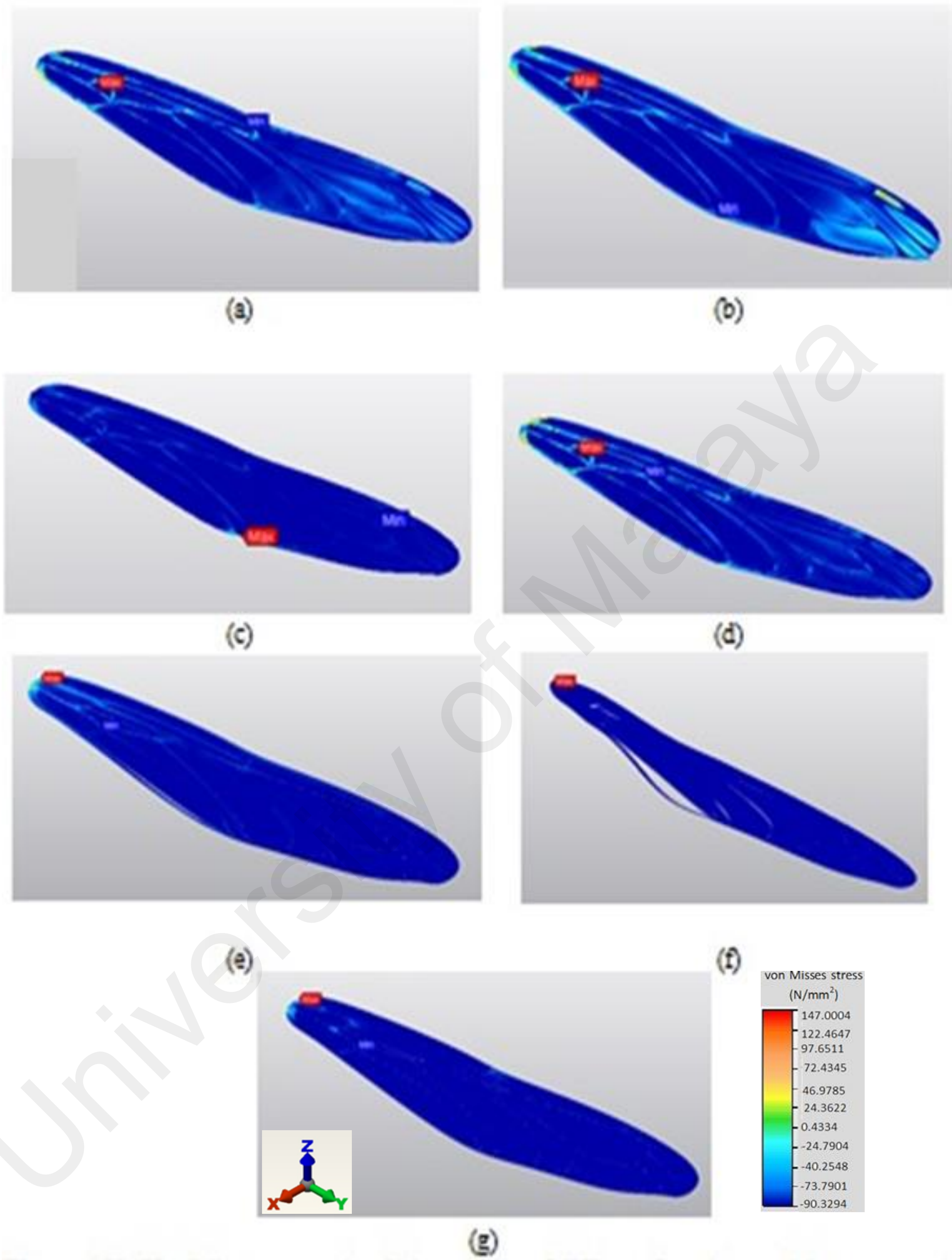

Figure 4.11: von Mises stress simulation results of different forewing model structures; (a) stainless steel (type 321), (b) balsa wood, (c) black graphite carbon fiber, (d) red prepreg fiberglass, (e) PLA, (f) acrylic, (g) ABS

The stress distribution of the hindwings with their membranes (shown in Figure 4.12) is also different than the wings without their membranes (shown in Figure 4.10). The maximum stresses for all of these wing models occurs on the membrane and not the frame. This is due to compression of the membrane in that region. This indicates that there is a high probability that the membrane in this region will be damaged. The maximum stress recorded is: 3.28 N/mm^2, 1.04 N/mm^2, 41.05 N/mm^2, 3.09 N/mm^2, 13.87 N/mm^2, 16.96 N/mm^2, 23.46 N/mm^2 for stainless steel (Type 321), balsa wood, black graphite carbon.

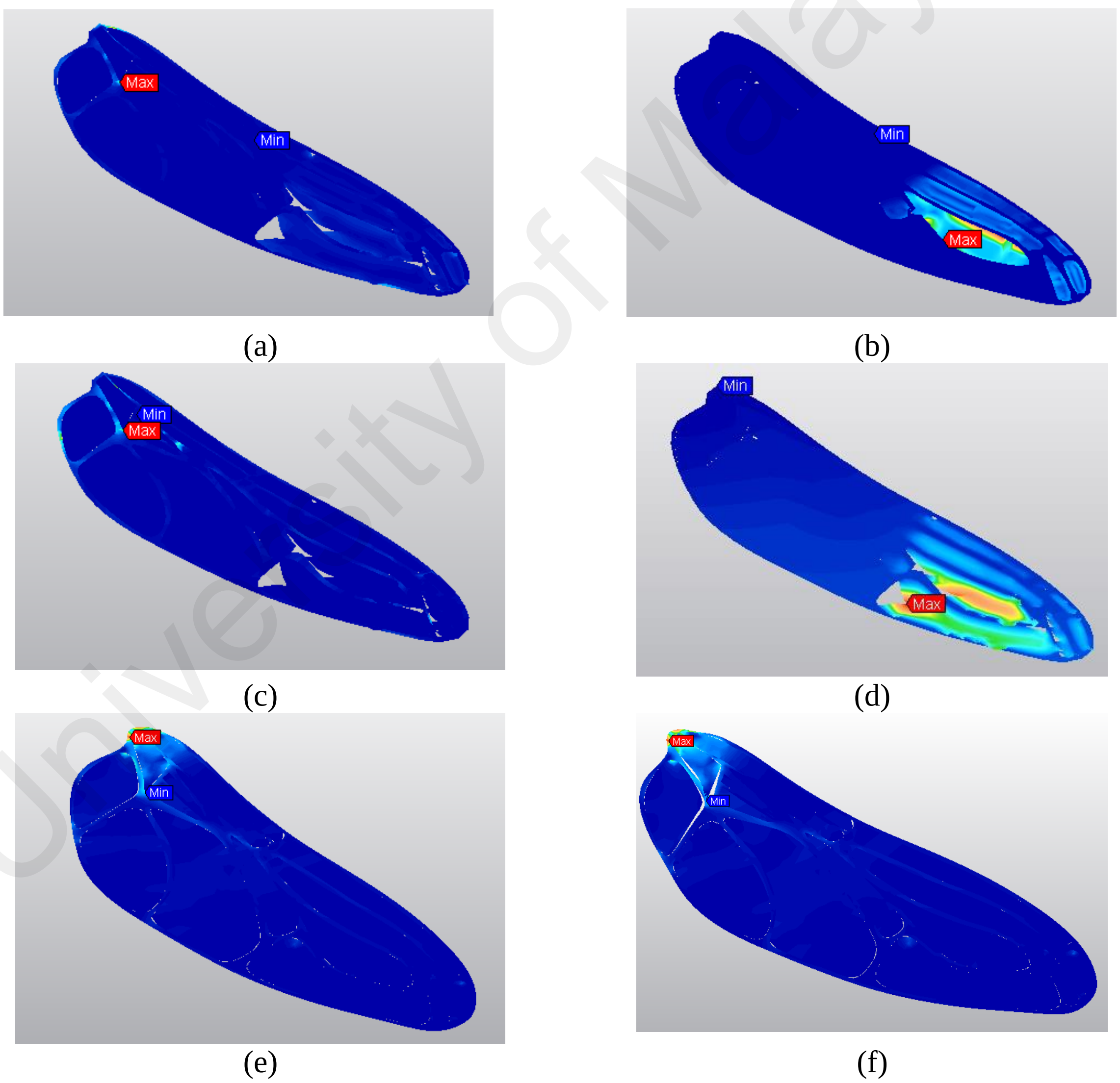

Figure 4.12: von Mises stress simulation results of different hindwing model structures; (a) stainless steel (Type 321),(b) balsa wood, (c) black graphite carbon fiber, (d) red prepreg fiberglass, (e) PLA, (f) acrylic, (g) ABS

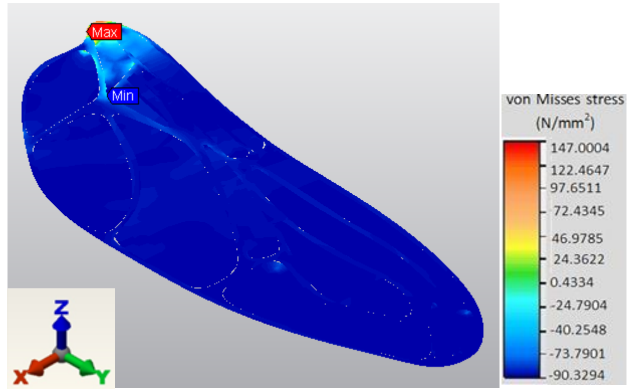

(g)

Figure 4.12: (continued) von Mises stress simulation results of different hindwing model structures; (a) stainless steel (Type 321),(b) balsa wood, (c) black graphite carbon fiber, (d) red prepreg fiberglass, (e) PLA, (f) acrylic, (g) ABS

4.5.3 Bending test simulation results (wing frames without membrane)

Some of the wing frames without membrane were subjected to bending tests. Only the steel and balsa wood frame structures were subjected to this bending test. Attempts to conduct bending tests on the red prepreg fiberglass, black graphite carbon fiber laminates, PLA, acrylic and ABS wing frame structures gave trivial results. These materials do not fail when subjected to bending test experiments (Babukiran et al, 2014). Therefore, the simulation results for black graphite carbon fiber, red prepreg fiberglass laminates, PLA, acrylic and ABS were not included.

Figures 4.13 and 4.14, shows the von Mises stress simulation results for the forewing and hindwing structures. The bending simulation results show uniformity in the stress distribution of all four frame structures for both forewing and hindwing. The maximum stress occurred in the same relative region for all four different frame structures, regardless of the wing type. This shows that bending creates a localized stress in both of the materials used. Combes et al. 2003 found that the flexural stiffness across the wing base line is maximum when it is subjected to bending (Combes, 2003). The hinge of a dragonfly wing must be able to withstand different types of loads, including forces subjected to rotational and translational motion. Hence the maximum stress occurred at the region near the wing base (where the pivot point is located), as highlighted in the simulation results. The maximum bending stresses for the forewings of stainless steel and balsa wood are: 0.80 N/mm^2 and 0.11 N/mm^2, respectively. The hindwing maximum stress was: 0.64 N/mm^2 and 0.05 N/mm^2 for stainless steel and balsa wood, respectively.

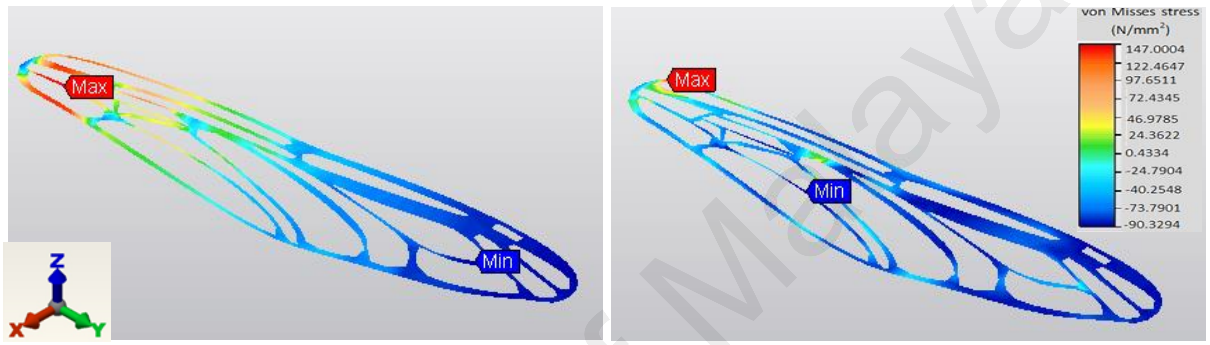

(a) (b)

Figure 4.13: von Mises stress simulation results of different forewing model structures; (a) stainless steel (Type 321), and (b) balsa wood

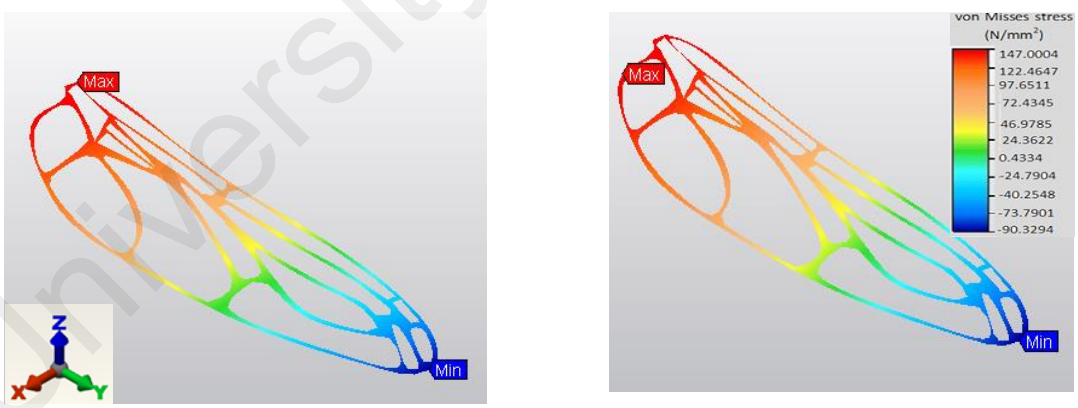

(a) (b)

Figure 4.14: von Mises stress simulation results of different hindwing model structures; (a) stainless steel (Type 321), and (b) balsa wood

4.5.4 Bending test simulation results (wing frames with membrane)

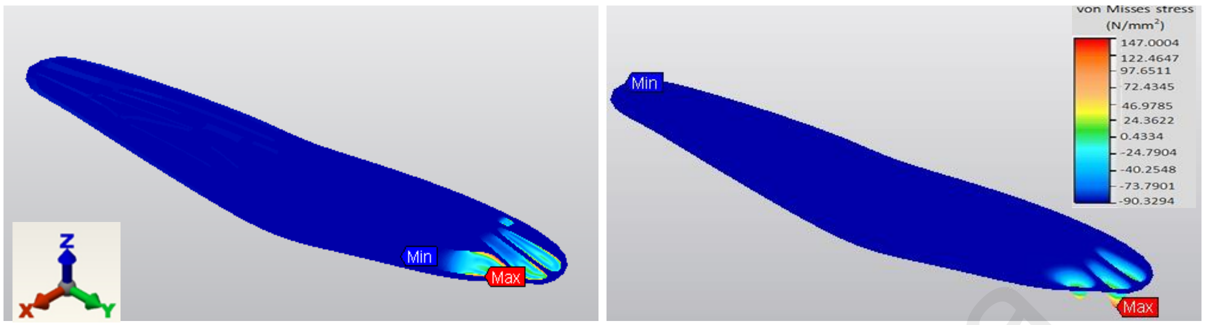

(a) (b)

Figure 4.15: von Mises stress simulation results of different forewing model structures; (a) stainless steel (Type 321), and (b) balsa wood

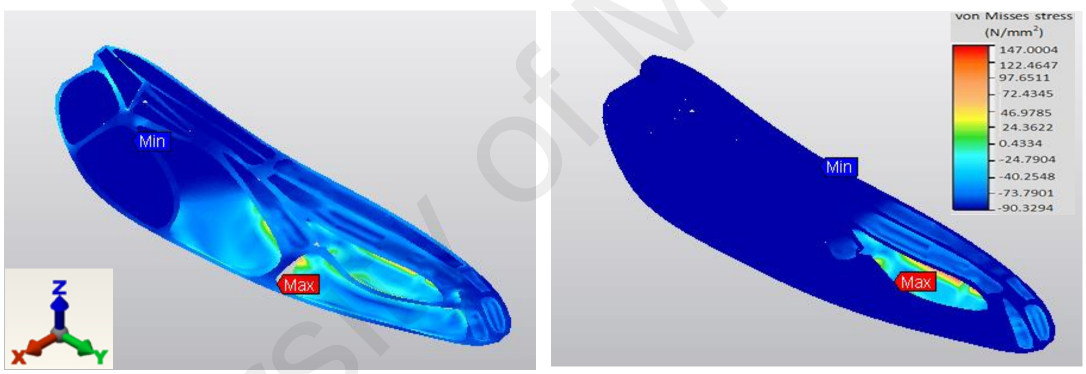

(a) (b)

Figure 4.16. Von Mises stress simulation results of different hindwing model structures; (a) stainless steel (Type 321), and (b) balsa wood

Figures 4.15 and 4.16 shows the bending stress created on the wing frames with their membrane. The results show that the tips of the wings undergo damage faster than the base of the wing. The figures also indicate that there is a greater probability of the membrane undergoing damage than the frame structure. The region where the tip of the wing undergoes bending deformation matches previous studies that have been conducted (HuaiHui, 2012 and 2013, Wakelling, 1997, Jiyu Sun, 2012 and Jongerius, 2010). The von Mises stress for the hindwing is 2.09 and 0.09 N/mm^2 for stainless steel and balsa wood, respectively. However, only the results obtained here clearly show the effects of the bending load on the membrane of an artificial dragonfly wing.

4.5.5 Tensile test experimental results

Figures 4.17 and 4.18 compare the forewing and hindwing for all seven different frame structure materials. They also compare the results of models with and without membranes, allowing the effects of the chitosan film on the frame structures to be observed. All four materials (without membrane) exhibit their original properties under tensile stress, which agrees with previous studies (David, 2014, Borrega, 2015, da Silva, 2007, Osei 2013 and 2014, Wang, 2013, Warren, 2015, and Tamilarasan, 2015). Both figures show a sudden decline in tensile stress, which indicates failure (fracture) has occurred (destructive testing). Figure 4.17(a) compares the steel forewing with and without membrane. The ultimate strength of the steel forewing with its membrane is 2.10 MPa and without membrane is 2.48 MPa. These values are 2.20 MPa with membrane and 2.45 MPa without membrane for the hindwing. These results show that the addition of the film membrane causes an 8% reduction of strength for the steel wing. The chitin nano-composite membrane solution oxidizes the stainless steel wing frame. We observed aggressive oxidation in our samples, even though precautions were taken to avoid it. Therefore, it can be concluded that adhesion of the film membrane to the stainless steel reduces its overall stress resistance and increases its oxidation. Therefore, stainless steel is a poor choice of material for the wing frame, when desiring to use a chitin nano-composite film wing membrane. Referring to Figures 4.11(a) and 4.12(a), the percent difference between the simulation and experiments are approximately 4.0% and 3.52%, with and without membranes, respectively. The simulation results do not take into count the decrease of strength caused by chemical degradation. The percentage results shows a good agreement between the experiment conducted and the simulation analysis obtained.

Figures 4.17(b) and 4.18(b) shows a comparison of balsa wood with and without membrane for both fore and hindwings. In contrast to stainless steel, the membrane reduces the stress acting on the balsa wood wing frame. The ultimate strength of the balsa wood forewing, with and without membrane, is 0.09 MPa and 0.03 MPa, respectively. The results of the hindwing, with and without membrane, were: 0.09 MPa and 0.04 MPa, respectively. This equates to an increase in ultimate strength that ranges from 125% to 200%. Therefore it can be concluded that adhesion of the chitosan nano-composite film to the balsa wood increases its strength tremendously. Referring to Figures 4.11(b) and 4.12(b), the percent difference between the simulation and experiments are approximately 6.23% and 4.56%, with and without membranes, respectively.

Figures 4.17(c) and 4.18(c) shows a comparison of carbon fiber wings, with and without film membranes. The adhesion of chitosan nano-composite film yields an immense increase in strength. The peak tensile strength for the forewings, with and without membranes, are 48.07 MPa and 1.32 MPa, respectively. The results for the hindwings, with and without membranes, are 40.06 MPa and 1.34 MPa, respectively. This shows that the addition of film increases the ultimate strength by 3000% to 3600%. This shows that the adhesion of the film to these carbon fiber models greatly intensifies its ultimate strength. Referring to Figures 4.11(c) and 4.12(c), the percentage differences between the simulation and experiments are approximately 5.23% and 3.87%, with and without membranes, respectively.

Figures 4.17(d) and 4.18(d) shows the results obtained for red prepreg fiberglass model wings. These results also show an increase in ultimate strength after adhesion of the chitosan nano-composite film. The ultimate strength for the forewing, with and without membranes, are: 2.03 MPa and 0.01 MPa, respectively. The ultimate strength for the hindwings, with and without membranes, is 3.04 MPa and 0.01 MPa, respectively. However, the red fiberglass undergoes warping and shrinkage at a very early stage of the experiment (1 minute after starting the experiment). So this phenomenon must be taken under consideration when considering this material for fabrication purpose. Referring to Figures 4.11(d) and 4.12(d), the percent differences between the simulation and experiments are approximately 5.75% and 8.93%, with and without membranes, respectively.

Figures 4.17(e) and 4.18(e) shows a comparison of PLA wings, with and without film membranes. The adhesion of chitosan nano-composite film yields an increase in strength. The peak tensile strength for the forewings, with and without membranes, is 200.07 MPa and 175.46 MPa, respectively. The results for the hindwings, with and without membranes, are 197.33 MPa and 162.06 MPa, respectively. This shows that the addition of film increases the ultimate strength by 14% to 22%. This shows that the adhesion of the film to these PLA models moderately increases its ultimate strength. Referring to Figures 4.11(e) and 4.12(e), the percentage differences between the simulation and experiments are approximately 2.62% and 3.81%, with and without membranes, respectively.

Figures 4.17(f) and 4.18(f) shows a comparison of acrylic wings, with and without film membranes. The adhesion of chitosan nano-composite film yields noticeable amount of increase in strength. The peak tensile strength for the forewings, with and without membranes, is 173.27 MPa and 168.95 MPa, respectively. The results for the hindwings, with and without membranes, are 188.71 MPa and 179.16 MPa, respectively. This shows that the addition of film increases the ultimate strength by 2% to 5%. This shows that the adhesion of the film to these acrylic models slightly increases its ultimate strength. Referring to Figures 4.11(f) and 4.12(f), the percentage differences between the simulation and experiments are approximately 2.12% and 3.55%, with and without membranes, respectively.

Figures 4.17(g) and 4.18(g) shows a comparison of ABS wings, with and without film membranes. The adhesion of chitosan nano-composite film yields noticeable amount of increase in strength. The peak tensile strength for the forewings, with and without membranes, is 265.77 MPa and 275.23 MPa, respectively. The results for the hindwings, with and without membranes, are 244.88 MPa and 257.61 MPa, respectively. This shows that the addition of film increases the ultimate strength by approximately 5%. This shows that the adhesion of the film to these acrylic models slightly increases its ultimate strength. Referring to Figures 4.11(g) and 4.12(g), the percentage differences between the simulation and experiments are approximately 1.73% and 1.56%, with and without membranes, respectively.

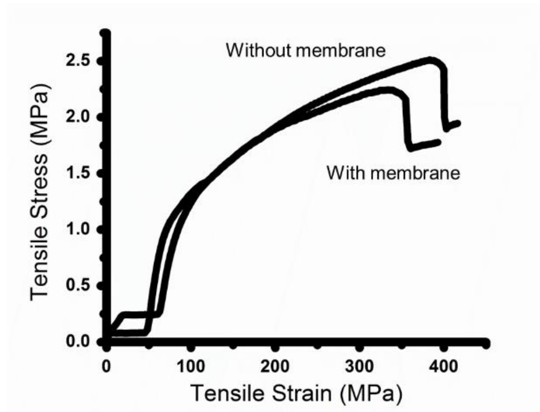

(a)

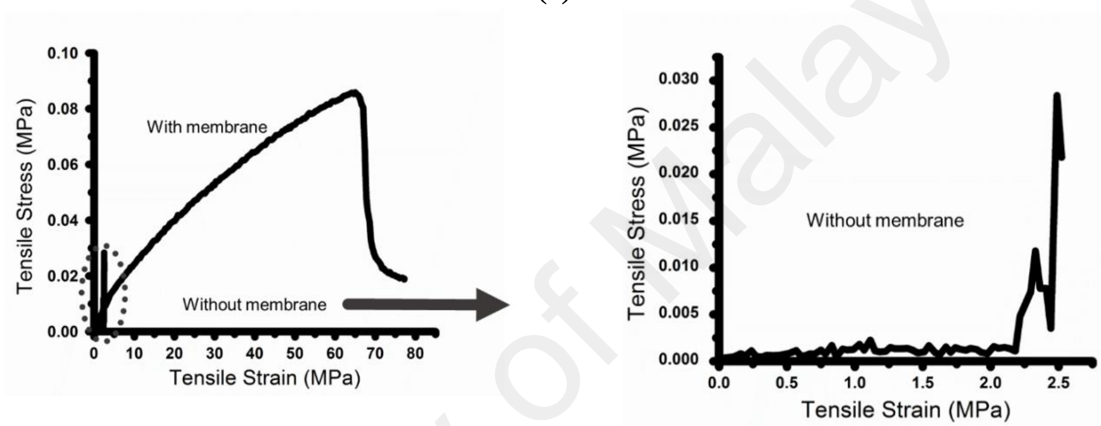

(b)

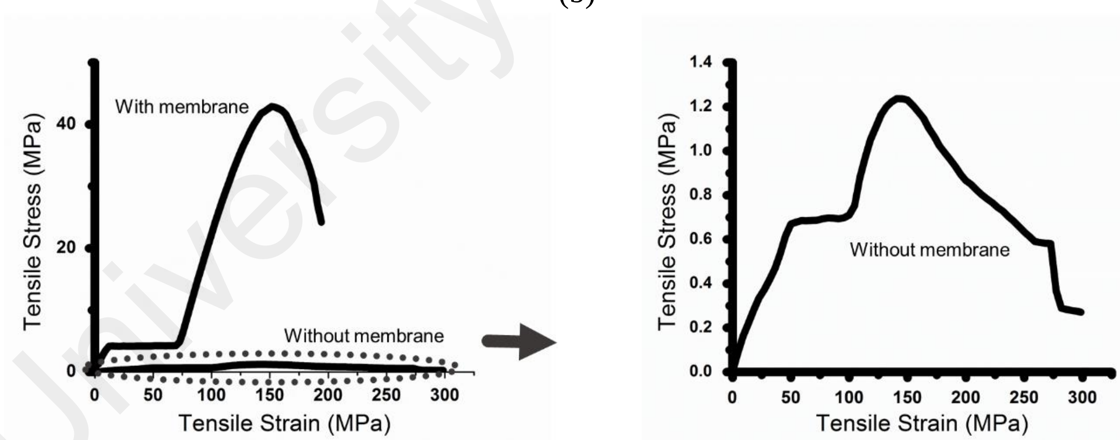

(c)

Figure 4.17: Tensile stress vs tensile strain (engineering) of all four forewing frame structures ; a) stainless steel (Type 321), b) balsa wood, c) black graphite carbon fiber, d) red prepreg fiberglass, e) PLA, f) acrylic and g) ABS

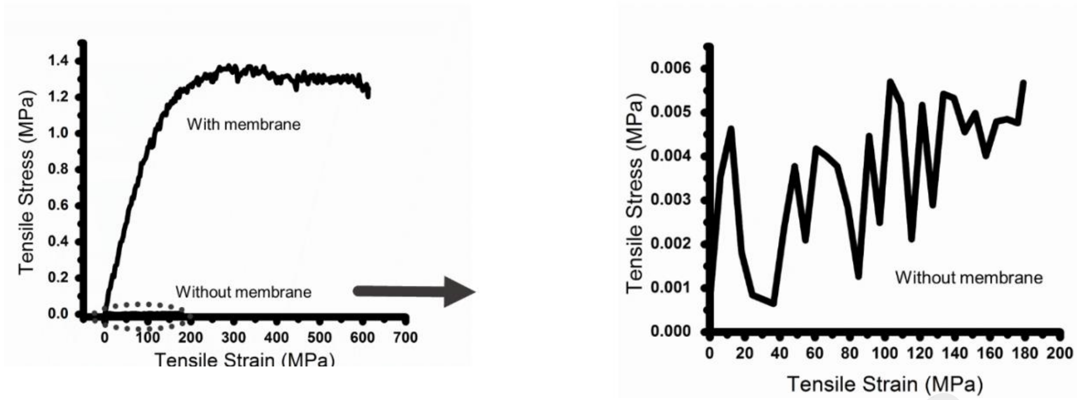

(d)

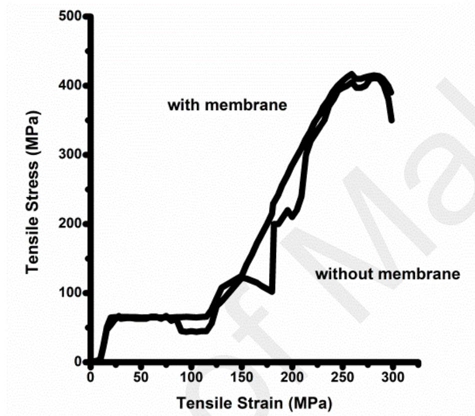

(e)

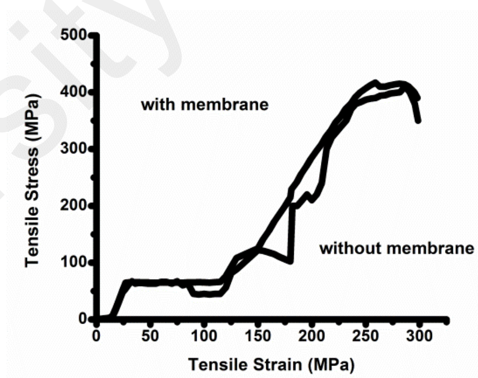

(f)

Figure 4.17: (continued) Tensile stress vs tensile strain (engineering) of all four forewing frame structures ; a) stainless steel (Type 321), b) balsa wood, c) black graphite carbon fiber, d) red prepreg fiberglass, e) PLA, f) acrylic and g) ABS

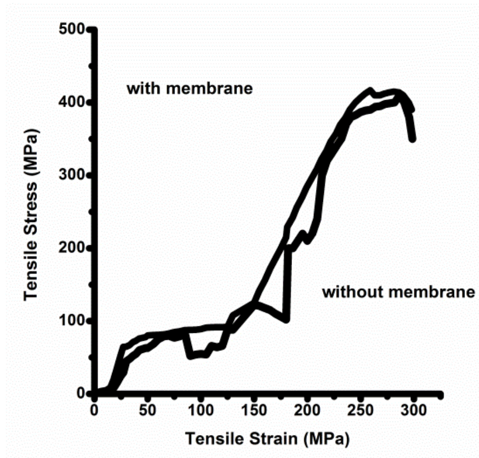

(g)

Figure 4.17: (continued) Tensile stress vs tensile strain (engineering) of all four forewing frame structures ; a) stainless steel (Type 321), b) balsa wood, c) black graphite carbon fiber, d) red prepreg fiberglass, e) PLA, f) acrylic and g) ABS

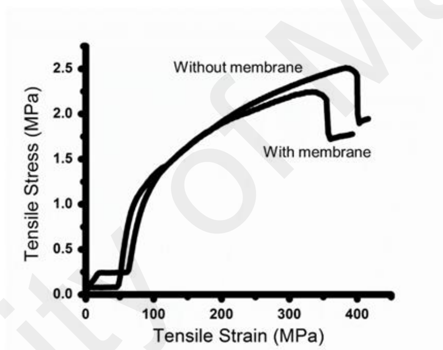

(a)

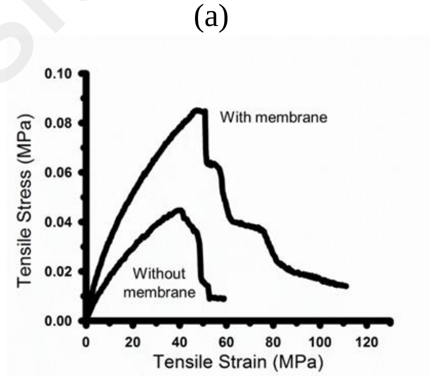

(b)

Figure 4.18: Tensile stress vs tensile strain (engineering) of all four hindwing frame structures; a) stainless steel (Type 321), b) balsa wood, c) black graphite carbon fiber, d) red prepreg fiberglass

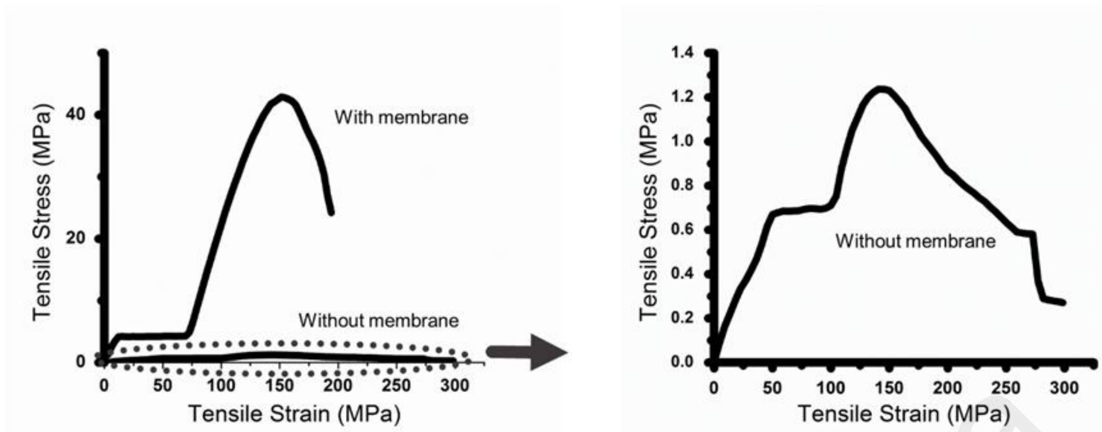

(c)

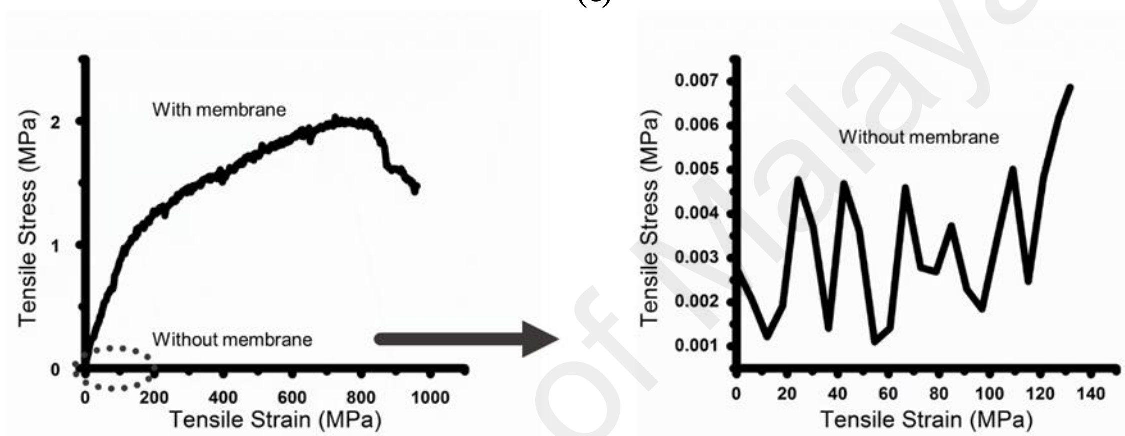

(d)

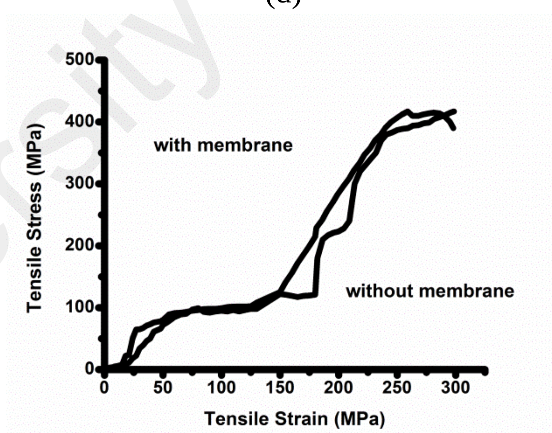

(e)

Figure 4.18: (continued) Tensile stress vs tensile strain (engineering) of all four hindwing frame structures; a) stainless steel (Type 321), b) balsa wood, c) black graphite carbon fiber, d) red prepreg fiberglass

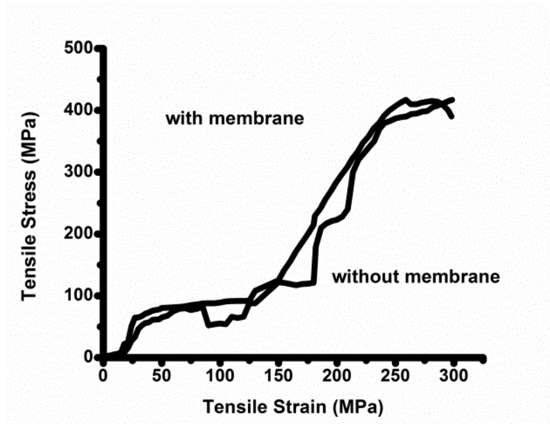

(f)

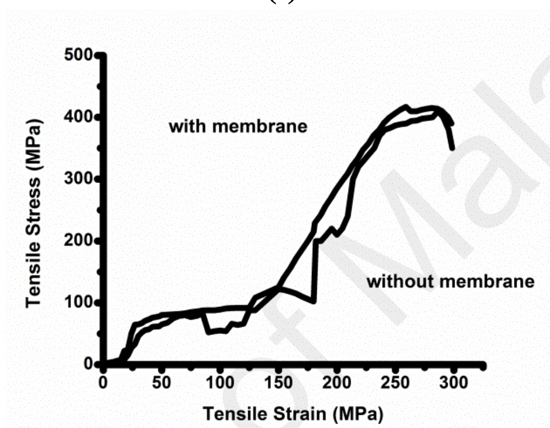

(g)

Figure 4.18: (continued**)** Tensile stress vs tensile strain (engineering) of all four hindwing frame structures; a) stainless steel (Type 321), b) balsa wood, c) black graphite carbon fiber, d) red prepreg fiberglass

4.5.6 Bending test experimental results

Figures 4.19 and 4.20 show the compression stress vs strain of the wing models made of stainless steel and balsa wood, respectively. Figures 4.17 and 4.18 showed a reduction in the ability of the wing frame to undergo tension when the film membrane is adhered to the stainless steel. However, this testing shows that its resistance to compression is higher in the wing models with film. Figures 4.19(a) and 4.20(a) show results for the stainless steel frames, both the fore and hindwings. The peak strength is 2.02 MPa with membrane and 0.75 MPa without membrane. This is an increase of 167%. The hindwings are 2.03 MPa and 0.63 MPa, with and without membrane, respectively. This is an increase of 140%. Referring to Figure 4.15 and 4.16, the percent difference between the simulation and experiments are approximately 9.97% and 8.74%, with and without membranes, respectively.

Figures 4.19(b) and 4.20(b) show results for the balsa wood frame structures. The peak strength for the forewing structure, with and without membrane, is 0.08 MPa and 0.04 MPa, respectively. The hindwings are 0.08 MPa and 0.04 MPa, with and without membrane, respectively. This is an increase of approximately 200% for both balsa wood fore and hindwings. Referring to Figure 4.16, the percent difference between the simulation and experiments are approximately 6.49% and 7.77%, with and without membranes, respectively.

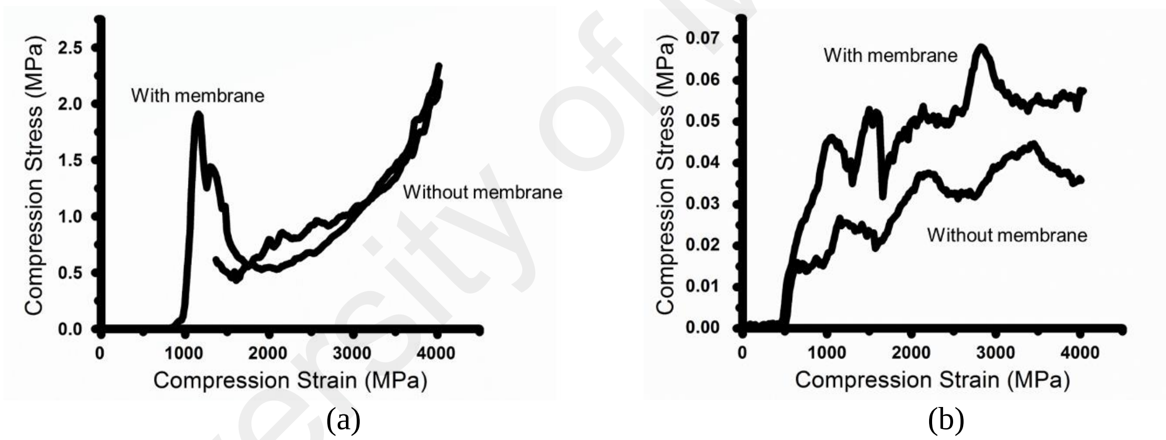

Figure 4.19: Compression stress versus compression strain graphs of forewing wing models. (a) stainless steel (Type 321), (b) balsa wood

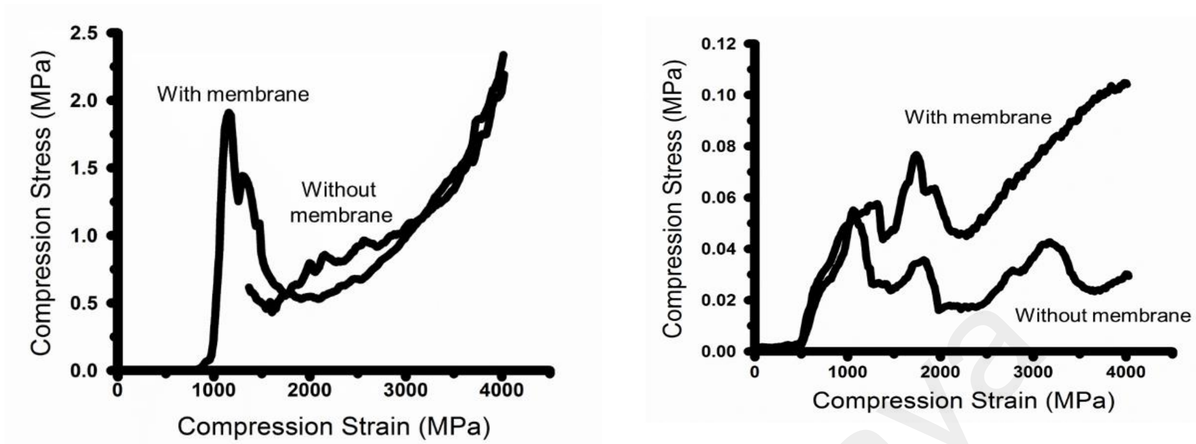

Figure 4.20: Compression stress vs compression strain for hindwing models. (a) Stainless steel (Type 321), (b) Balsa wood

4.6 High speed camera image results analysis

The high speed camera imaging experiment was conducted on each of the three types of wings; PLA, acrylic and ABS (both with and without the chitosan membranes). This was done to study the flexibility of each wing frame material and to determine the best material for use in a BMAV. An actual dragonfly wing (*Diplacodes Bipunctata*) was also tested to study its motion during passive flapping at different frequencies and compare it with the fabricated wings. The nomenclature for wing rotation about different axis is shown in Figure 4.21. This figure shows the types of rotation that an insect wing undergoes. Figures 4.22 and 4.23 shows a sequence of images, illustrating the wing motion of an actual flapping dragonfly wing during one complete flapping cycle. The wing beat frequency for these images is 30 Hz, which is the nominal wing beat frequency of this species of dragonfly. These figures show the common mode of flapping of an actual insect wing (dragonfly). At all frequencies from 10-250 Hz, the flapping motion is similar. As for the fabricated wings (all seven materials), the models only exhibit an up-down flapping motion. They lack the twist and bend motion exhibited in an actual insect wing.. The twisting motion of an actual dragonfly wing can be seen clearly in Figures 4.22 (b), (c), (d), (e) and 4.23(b), (c), (d), and (e). This twisting motion cannot be achieved by our fabricated wing models. This will affect the aerodynamics performance of the wing. However, the wing exhibits shown by these (PLA, acrylic and ABS) wings. Based on our previous simulation and experimental analysis mentioned in Section 4.5 and 4.6, it has been concluded that out of the seven materials, the three best materials were PLA, acrylic and ABS. These materials were chosen for following reasons:

- The thickness of the material was much thinner compared to steel, balsa, carbon fiber and red prepreg (less than 2mm). This matches the criteria of a dragonfly wing whereby the wings are supposed to be thin.
- These materials were much more flexible than the first four materials mentioned above (steel, balsa, carbon fiber and red prepreg)
- The simulation and experimental results shows a better agreement of when compared to an actual dragonfly wing. The percentage difference of strength between the actual dragonfly wing (based on previous literature) and the three materials (PLA, acrylic and ABS) ranged about 2%-5% which further strengthens the rationale of selecting these materials

Furthermore, in the flapping mechanism experiment, only the forewings were chosen to be tested. The difference between the forewing and hindwings tested previously (as mentioned in Section 4.5 and 4.6) yields strength results that were similar (with a percentage difference of 1%-2%) for both forewing and hindwing (with and without membrane). Also, according to previous literature, the hindwings act as a wing that generates lift during the flapping motion (Zheng Hu, 2009) Our experiments were based on a non-vacuum environment, (open air), hence the larger surface area of the hindwing shall affect the measurement parameters greatly. (bend angle, displaced distance and twist angle)

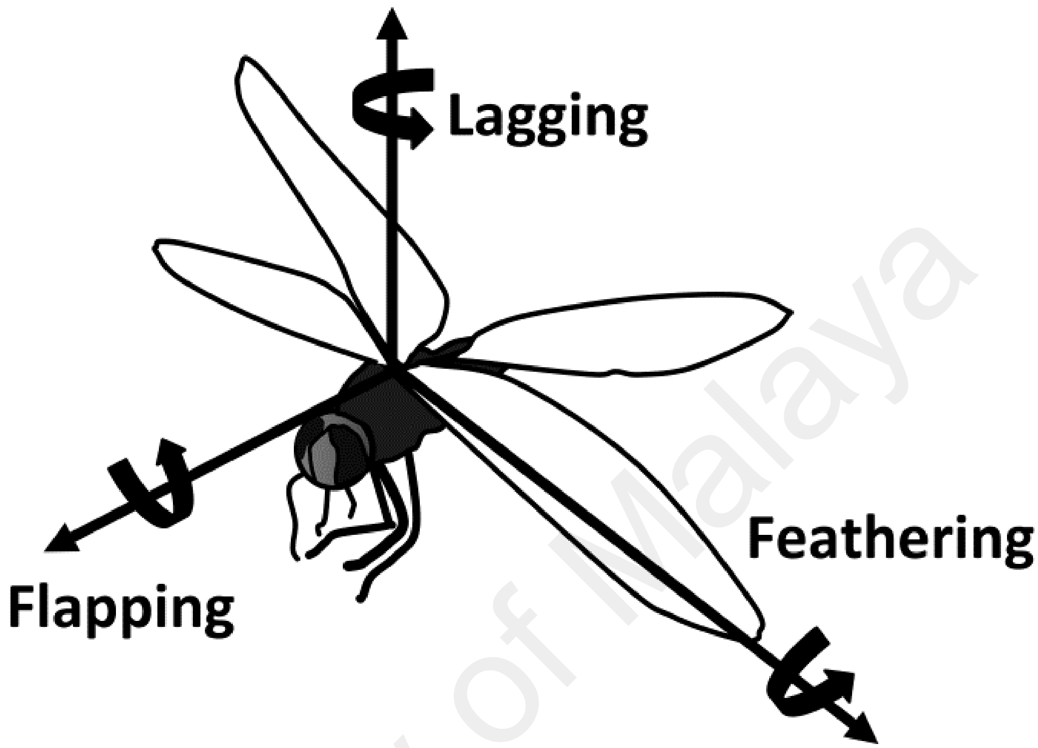

Figure 4.21: Degrees of freedom for the wings of flying insects

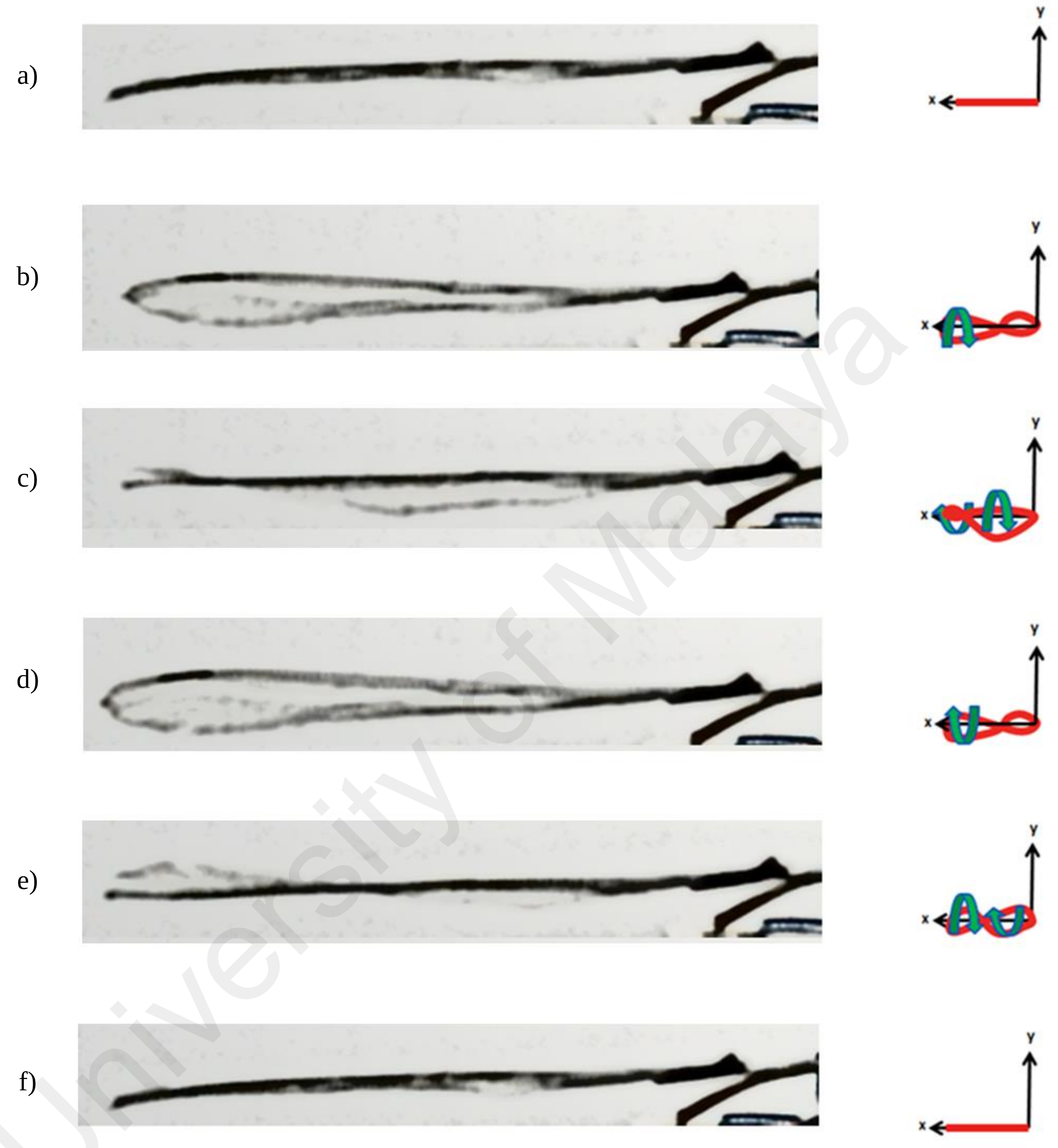

Figure 4.22: Side view of the actual dragonfly flapping wing (gray scale) captured by the high speed camera during one flapping cycle at 30Hz. a) start of downstroke, b) mid-downstroke, c) end of downstroke, d) start of upstroke, e) mid-upstroke, f) end of upstroke

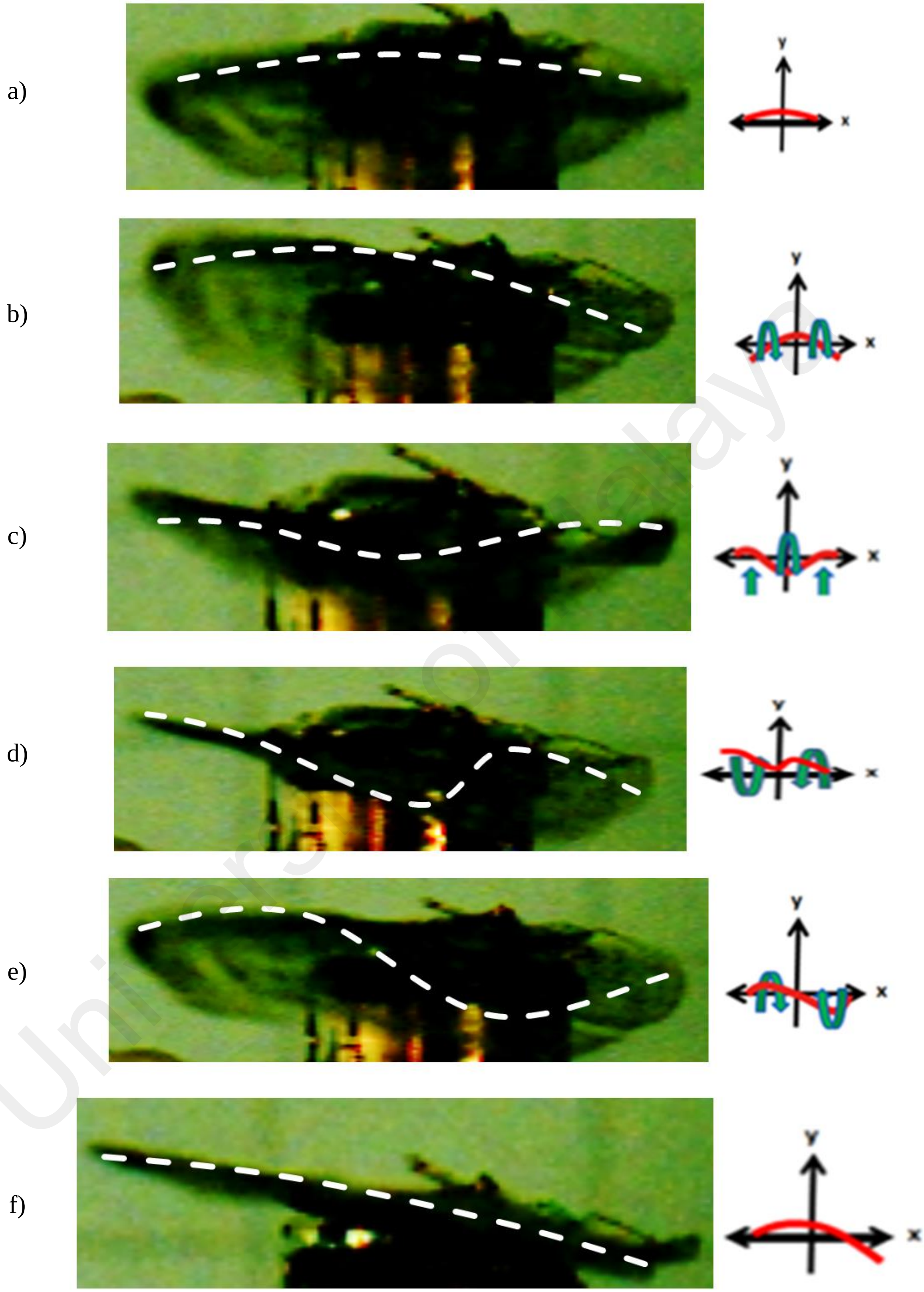

Figure 4.23: Front view of the actual dragonfly flapping wing captured by the high speed camera (gray scale) during one flapping cycle at 30 Hz. a) start of downstroke, b) mid-downstroke, c) end of downstroke, d) start of upstroke, e) mid-upstroke, f) end of upstroke

Dragonfly wings greatly deform during flight. This was observed in our experiment as well as others (Hisayoshi, 2014). Despite having a certain degree of rigidity, dragonfly wings undergo a considerable amount of bending, twisting and rotational motions. Figure 4.22 and 4.23 shows the motion of flapping wing in one complete cycle at 30 Hz (side and front view). It was observed that at both directions (chord and spanwise) an asymmetric twist-bend motion was observed. Figures 4.22(d), 4.22 (f), and 4.23(d) clearly show these asymmetric motions mentioned. At the end of an upstroke (observed in Figure 4.22(e), the wing momentarily exhibited a symmetrical twisting motion. A large feathering rotation range of 154° to 179° of the entire wing was observed during the beginning of the down stroke and end of the upstroke (for all frequencies) (Figure 4.23(a) and 4.23(e). Even during the steady phase (passive moment occurring when the flapping angle is zero), the wing is observed to undergo internal torsion. This corresponds well to previous studies made by Wootton et al. (Wooton, 1981 and 1993)

Besides the nominal 30 Hz wing beat frequency, the dragonfly wing was also flapped at frequencies of: 10, 20, 70, 120, 200, and 250 Hz. The pattern of deformations was similar for all of the frequencies observed. The measured bending angle, wing tip deflection, wing tip twist angle and speed for the different wing frames (without and with a membrane) were plotted for comparison to the results obtained from an actual dragonfly wing in Figures 4.24-4.27.

4.6.1 Bending angle versus flapping frequency

The bending angle is directly proportional to the flexibility of the wing. Previous studies have shown that wing flexibility has a significant influence on the aerodynamic forces (e.g. lift and thrust) generated by the flapping wing (Zhao, 2009). However, this study focuses only on the chordwise flexibility of a passive flapping wing. Bending angles were measured along the chordwise direction. Chang et al.(2013) also investigated chordwise flexibility, but for simple, non-anisotropic wing structures. They presented a detailed assessment of the effects of structural flexibility on the aerodynamic performance of flapping wings. The Reynolds number (*Re* =100) considered in this study is relevant to small insect flyers, such as fruit flies. However, this study only includes the role of chordwise flexibility and passive pitch in two dimensional plunging motions.

Our study involves a much more complex wing design than this past study by Chang, 2013.. Figure 4.24 shows the bending angles as the wing beat frequency is varied for the three fabricated wing frames (without and with a membrane) in comparison to an actual dragonfly wing. These figures show that the maximum bending angle (θ_{max}) for all the wings occurs during the upstroke. This was observed for both frames (without and with a membrane). This agrees with previous research done by Jongerius et al. (2010) in which this asymmetry (difference in bending angle between the upstroke and down stroke) was attributed to the directional bending stiffness in the wing structure (e.g. one-way hinge or a pre-existing camber in the wing surface)

The maximum bending angle of dragonfly wings at 30 Hz is recorded to be about 6°. The wings were observed to have a maximum bending angle of 10.7° at 120 Hz (natural frequency of an actual dragonfly). This is an increase of 78.3% from 30 Hz. ABS shows a high level of flexibility compared to the other two materials used. Figure 4.24 shows that the bending angle curves of the fabricated ABS wings are more similar to the actual dragonfly wing than the other two types. Figure 4.24(a) shows that the bending angle of ABS wing (without membrane) at 30 Hz is 8.5° and 5.9° at 120 Hz. At 30 Hz, the percentage difference between an ABS wing (without membrane) and an actual dragonfly wing is about 41.7%. The PLA and acrylic wings each recording a percentage difference (reduction) of 70%. In Figure 4.24(b), ABS exhibits much larger bending angles at 30 Hz when the membrane is added. The value of the ABS wing (with membrane) is 20.1° at 30 Hz and 34.9° at 120 Hz. This angle is much larger than the actual dragonfly wing. The percentage increase between the ABS and an actual dragonfly wing is 233.3%. The other two materials (PLA and acrylic) exhibited much lower bending angles than the actual dragonfly wing. The percentage reduction in PLA and acrylic (in comparison to an actual dragonfly wing) is 83.3% and 75%, respectively.

These observations confirm that the overall flexibility of the wing decreases after the membrane is attached, except for ABS. At a frequency of 120 to 170 Hz, the dragonfly wing bends at a very high angle. Previous research shows that dragonflies do not flap at their natural frequency (120 to 170 Hz) (Maria, 2011). So this result is likely due to a resonance effect caused by the wing beat frequency being proximate to the natural frequency of the wing. This result confirms that dragonflies have a maximum wing beat frequency limitation in this range. The ABS wing frame shows a similar trend at 120 Hz. The bending angle is reduced at frequencies greater than 120 Hz for both the actual dragonfly wing and the three fabricated wings.

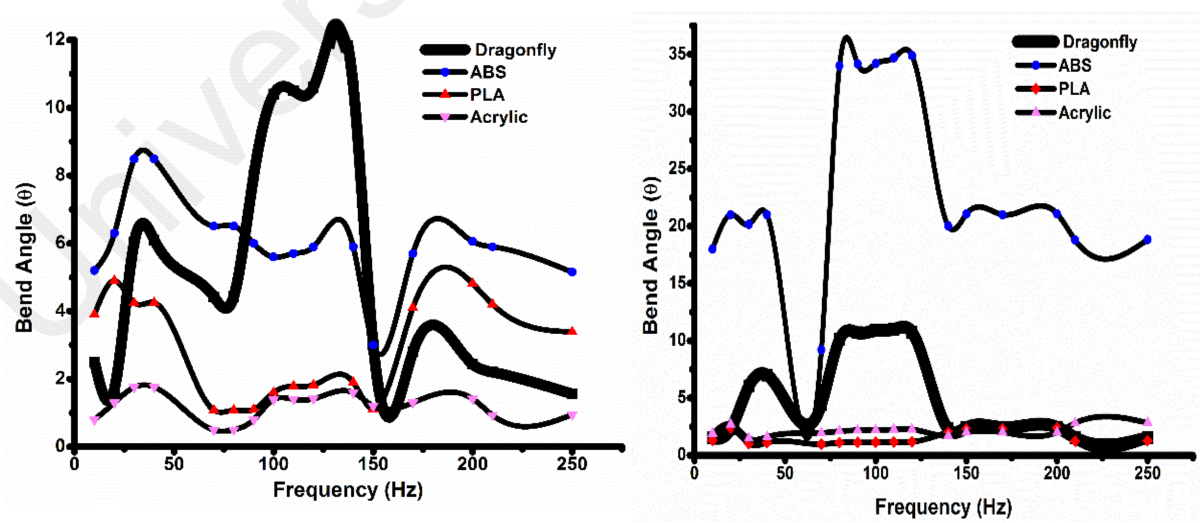

(a) (b)

Figure 4.24: Bending angle of different wing frames; (a) without membrane and (b) with membrane.

4.6.2 Wing tip deflection versus flapping frequency

Figures 4.25(a) and (b) show the wing tip deflection for varying wing beat frequencies of the three fabricated wing frames (without and with membranes) in comparison to an actual dragonfly wing. Similar to bending angle, deflection is another measurement that can be used to assess a flapping wing's flexibility. As mentioned earlier, past studies have shown that wing flexibility has a significant effect on the wing's ability to generate a suitable time-averaged lift or thrust (Zhao, 2009). Similar to θ_{max} in Figure 4.24, Figure 4.25 shows that the maximum deflection (d_{max}) occurs during the upstroke. This again was observed for both frames (without and with a membrane). This agrees with previous research done by Luo et al (2012).

Figure 4.25 (a) shows that all of the fabricated wing frames (without membrane) deflect at magnitudes that are similar (only slightly reduced) to the actual dragonfly wing at 30 Hz which is about 7.1 mm. At 30 Hz, ABS has a percentage increase of 23.94%. PLA and acrylic both have a percentage reduction of 47.71% and 62% respectively. However Figure 4.25 (b) shows that the fabricated wing frames (with membranes) have very different deflections than the actual dragonfly wing. Only the ABS wing showed a comparable level of deflection, however the dragonfly wing is 40.85% lower than the ABS wing. The PLA and acrylic wings have percentage reduction of 94.37% and 66.2%, respectively compared to the dragonfly wing. The actual dragonfly wing is able to undergo a large deflection at the tip region. This supports previous studies which explain that the difference between the deflection at the tip and the surface is created by differences of the rigidity (due to the vein and corrugations) along the wing surfaces (Charles, 2011).

The difference in deflection between wing frames without a membrane and with a membrane shows that the attachment of a membrane causes an increase in rigidity. This increase in rigidity is observed to be the highest in the PLA wing. Only the ABS wing shows a similar curvature trend with the actual dragonfly wing around 120 Hz. At 120 Hz, an increase in percentage of 81.7% (without membrane) and decrease in percentage of 69.7% (with membrane) is seen in ABS wing frame. Compared to the PLA wing there is a percentage reduction of 82.6% (without membrane) and 64.2% (with membrane). The acrylic wing has a percentage reduction of 85.3%, both without and with the membrane attached. The trend of the graph again shows that there is a decrease in flexibility after the membrane has been attached. Two high peaks were observed for an actual dragonfly wing (30 and 120 Hz). As already stated, the natural frequency of dragonfly wings has been reported to be between 120 to 170 Hz (Maria, 2011). The extreme fluctuation observed in this range confirms the observation.

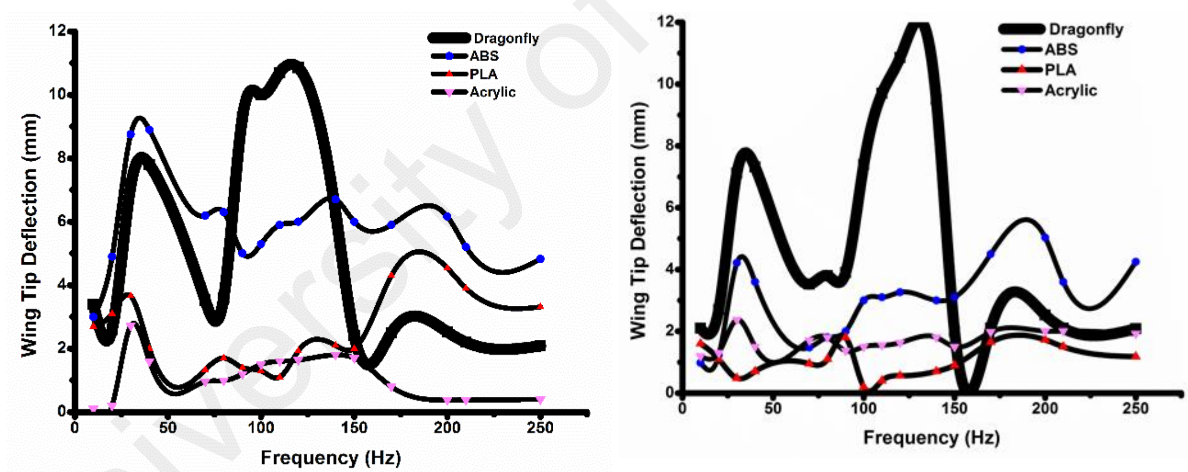

(a) (b)

Figure 4.25: Wing tip deflection of different wing frames; (a) without membrane and (b) with membrane

4.6.3 Wing twist angle versus flapping frequency

Figure 4.26 shows the maximum wing tip twist angle of the three fabricated wing frames in comparison to an actual dragonfly wing. The maximum twist angle was recorded during the stroke reversal (transition from upstroke to down stroke). The twist angle for an actual dragonfly wing at 30 Hz is 154.58°. Untwisted wings have large; drag producing wing surfaces that are exposed to flow hence, the importance of twisting in wings is justified. Wing tip twist also plays an important role in enhancement of flight performance. The mid-stroke timing of wing deformation in the butterfly, examined by Lingxiao et al (2013), suggests that the deformation is not due to wing inertia, because the acceleration of the wing is small at this point in the stroke. They suggest that this is instead due to aeroelastic effects, since the aerodynamic forces are very large at mid-stroke.

Figures 4.26 (a) and (b) show that both the PLA and acrylic wing frames (both without and with membranes) closely match the performance of an actual dragonfly wing. At 30 Hz, the ABS (without and with membrane) has a percentage reduction of 19.8% and 1.10% respectively in comparison to the actual dragonfly wing. The PLA wing (without and with membrane) has a percentage increase of 5.2% and 9.7% respectively. The acrylic wing (without and with membrane) has a percentage increase of 7.1% and 11.7% respectively. At 120 Hz, the ABS and acrylic wings (without membrane) has a percentage reduction of 10.2% and 2.5%, respectively compared to the dragonfly wing. The PLA wing (without membrane) has a percentage increase of 2.9%. The ABS wing (with membrane) has a percentage reduction of 35.9% compared to the dragonfly wing. While the PLA and acrylic wings have a percentage increase of 5.3% and 3.6% respectively. Based on these results, the PLA and acrylic wings are more similar to the actual dragonfly wing than the ABS wing. The large fluctuation of the ABS wing across varying flapping frequencies (10 to 250 Hz) makes it a more complicated BMAV option. Another trend observed from Figure 4.26 is that the wing tip twist angle of the dragonfly wing does not vary significantly as the flapping frequency is varied. This matches a previous study by Zhao et al. (2009). (mentioned earlier) which shows that the flexibility of insect wings increases more chordwise than spanwise, due to the rigid leading edge vein. This is true for both categories of wing frames (with and without membrane).

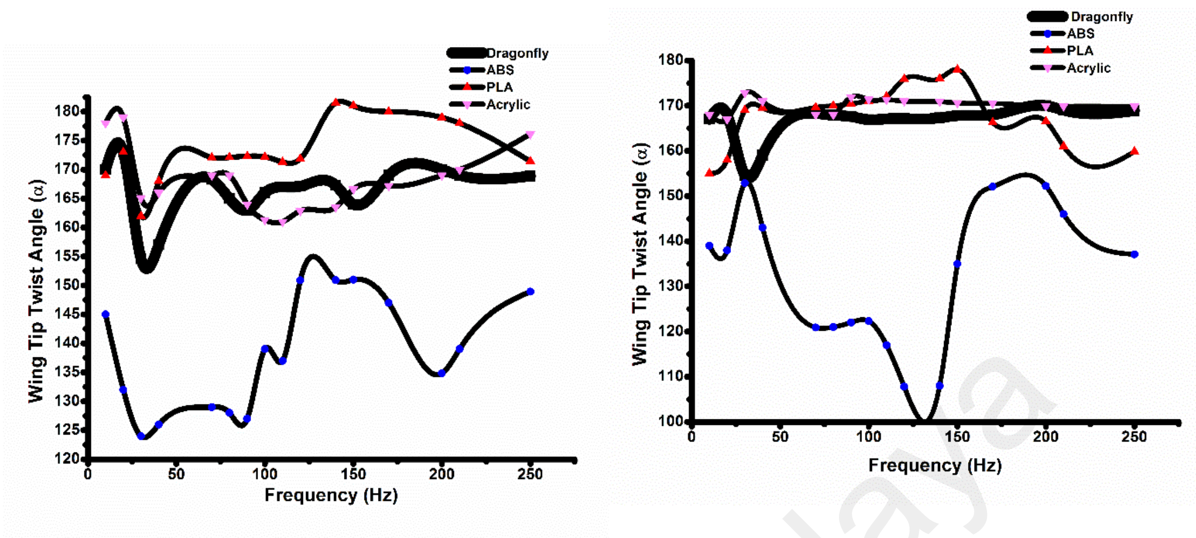

(a) (b)

Figure 4.26: Wing twist angle of different frames versus flapping frequency; (a) without membrane and (b) with membrane

4.6.4 Wing tip twist speed versus flapping frequency

Figure 4.27 shows the wing tip twist speed for the three wing frames (without and with membranes) in comparison to an actual dragonfly wing. Vogel (2013) stated that the wing tip twist speed varies according to size and must exceed a ratio with flight speed (wing tip twist speed: flight speed) by 3.7 or more to enable forward flight. Figure 4.27 shows that the PLA and acrylic wing frames (both without and with membranes) show a similar curvature trend with the actual dragonfly wing. The wing tip twist speed of an actual dragonfly wing at 30 Hz is 9.2 revolutions per second. At 30 Hz, the PLA wing shows a percentage increase of 33.3% (without membrane) and percentage reduction of 52.2% (with membrane) in comparison with the dragonfly wing. The acrylic wing shows a percentage increase of 30.4% (without membrane) and 44.4% (with membrane). The ABS wing shows a percentage reduction of 67.4% (without membrane) and 64.1% (with membrane). At 120 Hz, all of the fabricated wing frames without the membrane attached show a slight percentage increase in comparison to an actual dragonfly wing. The ABS, PLA, and acrylic wings show a percentage increase of 6.4%, 4% and 5%, respectively. While the ABS, PLA and acrylic wing frames without membrane have a percentage of 37.5%, 35.14% and 37.4%, respectively. The ABS wing frame shows a much different curvature trend than the others, both with and without membrane. Figure 4.27 shows that the wing tip twist speed is highly dependent on the flapping frequency and is less influenced by changes in the frame’s flexibility. This can be confirmed by observing the curves of the wing frames with membrane. The observed trend is the same across varying flapping frequencies (10-250 Hz) for both types of wing frames.

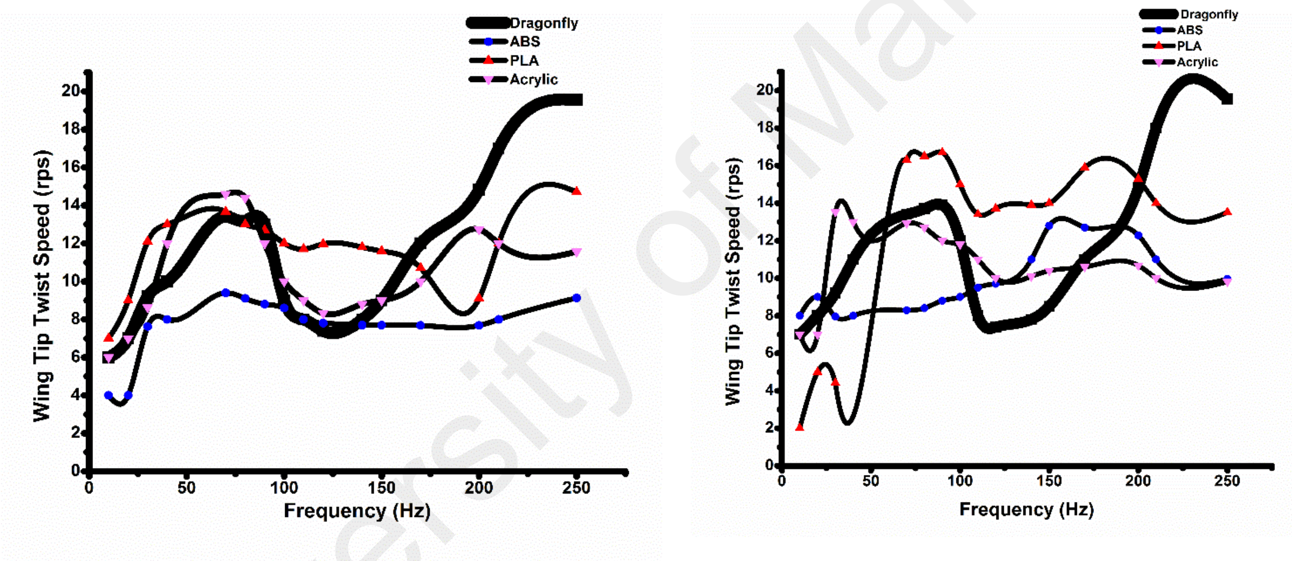

(a) (b)

Figure 4.27: Wing tip twist speed; a) without membrane and b) with membrane

As mentioned before, the study conducted by Yang et al (2012), concludes that the spanwise flexible deformation should be limited to a small range to achieve higher aerodynamic performance for a flapping MAV. Alternatively a larger chordwise deformation could serve to enhance the aerodynamic performance (e.g. lift and thrust generation). The results of our experiments in flapping an actual dragonfly wing support this observation, by showing that chordwise deformation is very significant (Figures 4.24-

4.27) compared to the spanwise deformation. These results suggest that BMAV wings should be designed with a stiff leading edge to limit the spanwise deformation and flexible ribs to keep chordwise deformation within a significant but suitable range. This indicates that the ABS wing design is better suited for use in a BMAV than the PLA and acrylic wing designs. The dragonfly wing was used as a comparison to test the effectiveness of the fabricated wings. No attempts were made to remove the membrane of an actual dragonfly wing since the idea was to test all the fabricated materials (with and without membrane) in comparison to an actual wing. From the graphs above, it could be noted that the fabricated wings were much more rigid in certain ranges of frequency (significantly from 200-250 Hz). These results show that the fabricated wings were not able to match the higher degree of flexibility exhibited by a dragonfly wing at larger frequencies. However, in the case of an actual dragonfly as stated earlier, the wing beat frequency is 30 Hz and the natural flapping frequency is 120 Hz. Hence, the rigidity of the fabricated wings beyond these frequencies is of least concern.

CHAPTER 5: CONCLUSION

5.1 Conclusions

The overall objective of this study was to produce a working simplified wing model based on a dragonfly wing. In order to achieve our objective, various methods were employed which resulted in our final product. Firstly, a methodology for producing accurate but simplified dragonfly wing models was described. The first step was to create a detailed model, using the Canny edge detection method on digital images of dragonfly fore and hind wings. The spatial network analysis method was then used to create simplified models from this detailed model. Both sets of models were used to calculate the natural flapping frequency, deformation, and displacement using Autodesk. It was shown that the simplified models produced very similar results (less than 13% difference for all calculations). Therefore, this shows that the spatial network analysis is a suitable approach to simplify a complicated insect wing structure (like a dragonfly). It is possible to fabricate this simplified model, because it is within available micro laser cutting and 3D printing allowances which enable its fabrication.

Secondly, a study that compares the mechanical properties of fourteen wing structures and analyzes the effect of adhering a chitosan nano-composite film membrane. Both FEA simulations and experiments were performed and all of the results showed good agreement (less than 10% difference). Each of the seven materials considered for the wing frame exhibited different characteristics. These seven materials were chosen because of their potential suitability for use as wing frames on a BMAV. Stainless steel (Type 321) has a high load bearing capacity, but experimental tests with steel wing frames showed that the addition of the film reduces its tensile resistance and causes aggressive oxidation. Steel is also relatively heavy making it a poor choice for this application. In contrast, film adhered to a balsa wood wing frame increased its tensile strength by 125% to 200%, while the peak bending strength was improved by about 200%. However, both steel and balsa wood is relatively inflexible compared to the other two materials. The black graphite carbon fiber shows a remarkable Results show an increase in ultimate strength after it is adhered with the chitosan nano-composite film membrane. The ultimate strength for the forewing, with and without membranes are: 2.03 and 0.01 MPa, respectively. The ultimate strength for the hindwings, with and without membranes, are 3.04 and 0.01 MPa, respectively. The primary drawbacks in using red pre-impregnated fiberglass is that it undergoes warping and rapid shrinkage. The load bearing capacity is also low compared to the other materials.

Use of PLA materials, fabricated using a 3D printer were also examined. The PLA wings showed a remarkable load bearing capacity. The peak tensile strength for the forewings, with and without membranes, is 200.07 MPa and 175.46 MPa, respectively. The results for the hindwings, with and without membranes, are 197.33 MPa and 162.06 MPa, respectively. This shows that the addition of film increases the ultimate strength by 14% to 22%. This shows that the adhesion of the film to these PLA models moderately increases addition of the film reduces its tensile resistance and causes aggressive oxidation. Steel is also relatively heavy making it a poor choice for this application. In contrast, film adhered to a balsa wood wing frame increased its tensile strength by 125% to 200%, while the peak bending strength was improved by about 200%. However, both steel and balsa wood are relatively inflexible compared to the other two materials. The black graphite carbon fiber shows a remarkable load bearing capacity and its lightweight property makes it suitable for BMAV applications. Its primary disadvantage is the practical difficulties involved in carving it into the simplified wing frame structure. Wing frames fabricated from the red pre-impregnated fiberglass mimics the elasticity and flexibility of an actual dragonfly wing structure, making it the most suitable material to be used. Results show an increase in ultimate strength after adhesion of the chitosan nano-composite film. The primary drawbacks in using red pre-impregnated fiberglass is that it undergoes warping and rapid shrinkage. The load bearing capacity is also low compared to the other materials. The PLA wings showed a remarkable load bearing capacity. The acrylic wings, exhibited similar results to PLA wings with the adhesion of chitosan nano-composite film significantly increased the strength. The adhesion of chitosan nano-composite film to ABS wing models yields noticeable amount of increase in strength. It shows that the adhesion of the film to these acrylic models slightly increases its ultimate strength. The percentage differences between the simulation and experiments are approximately 1.73% and 1.56%, with and without membranes, respectively.

One of the many challenges faced in constructing a working BMAV, involves the need to fabricate a highly deformable and flexible wing that has a large load bearing capacity. The third phase of the research was to conduct an experimental study to assess aero-elastic properties of flapping wings fabricated from the three chosen materials (PLA, acrylic, and ABS). These materials were chosen due to a number of criteria; the thickness of the material was much thinner compared to steel, balsa, carbon fiber and red prepreg (less than 2mm). This matches the criteria of a dragonfly wing whereby the wings are supposed to be thin. These materials were much more flexible than the first four materials mentioned above (steel, balsa, carbon fiber and red prepreg). The simulation and experimental shows a better agreement of mechanical strength when compared to an actual dragonfly wing compared to the first four materials. The percentage difference between the actual dragonfly wing (based on previous literature) and the three materials (PLA, acrylic and ABS) ranged about 2%-5% which further strengthens the decision of selecting these materials. The structural design of each of these wings is identical and based on biomimicry of an actual dragonfly wing. The experimental results were compared to the actual dragonfly wing, on which they are based, in order to assess their potential application to a BMAV design. A flapping mechanism that uses an electromagnetic actuator is used. This mechanism was used to flap the wings at various frequencies from 10 to 250 Hz. A high frame rate imaging system, that uses two cameras, was used to capture the three dimensional motion of the flapping wing. Several different aero-elastic parameters were measured: bending angle, wing tip deflection, wing tip twisting angle, and wing tip twisting speed. Analysis of wing bending angle and wing tip deflection indicates flexibility of the wing in the chordwise direction, while the wing tip twist angle and speed shows the flexibility of the wing in the spanwise direction. The ABS wing exhibited the highest chordwise flexibility (indicated by their large bending angles and wing tip deflections). Although the PLA and acrylic fabricated wings exhibited a much lower chordwise flexibility than the ABS fabricated wing and the dragonfly wing, their spanwise flexibility (indicated by their wing tip twist angles and speeds) closely matched the dragonfly wing.

These experimental results show that an actual dragonfly wing has a highly deformable structure despite its rigidity. Our materials, though possess a certain amount of flexibility, they were unable to match the twisting motions exhibited by an actual dragonfly wing. The materials examined in this study (PLA, acrylic and ABS) were selected due to their high flexibility, low density, and low fabrication costs. The ABS wing design gave better results in matching the chordwise flexibility of the actual dragonfly wing, while limiting the spanwise flexibility to much greater degree than the other two designs.

5.2 Future Work

The choice of materials available to model a wing frame is limitless. There are many other new emerging materials such as ultra-PLA, and nano-ceramics which can be explored to fabricate these wing frames. The basic idea of creating a simplified model has been given in this research. This model can be used for future studies. Despite its corrugated structure and brittle nature, an actual dragonfly wing can exhibit a high degree of flexibility. It is hoped that by exploring different wing frame materials, this degree of flexibility can be achieved. The idea of the simplified model can further be expanded to create a 3D model which encloses the tubules (hollow structures in the frame) if possible. It is hoped that this optimization (simplification) method will be further explored and will open up new possibilities to mimic various insect wings (for BMAV) application purposes.

REFERENCES

Ada Silva and Kyriakides S. (2007) Compressive response and failure of balsa wood. *International Journal of Solids and Structures*, 44, 8685-8717.

Aimy Wissa, Jared Grauer, Nelson Guerreiro, James Hubbard Jr, Cornelia Altenbuchner, Yashwanth Tummala, Mary Frecker, Richard Roberts. (2015). Free Flight Testing and Performance Evaluation of a Passively Morphing Ornithopter. *International Journal of Micro Air Vehicles.* 7(*1*), 21-40.

Akın D, Kasgoz A, and Durmus A. (2014). Quantifying microstructure, electrical and mechanical properties of carbon fiber and expanded graphite filled cyclic olefin copolymer composites. *Composites Part A: Applied Science and Manufacturing*, 60(*5*), 44-51.

Akira Azuma, Tadaaki Watanabe. (1988). Flight Performance of a Dragonfly. *Journal of Experimental Biology*. 137 (*1*) 221-252.

Angel S. J.P, Daniel L. Civco.(2010). Ten compactness properties of circles: measuring shape in geography. The Canadian Geographer, 4, 441-461.

Antonia B Kesel U.P, Wener Nachtigall. (1998). Biomechanical aspects of the insect wings: an analysis using the finite element method. *Computers and Biology in Medicine*, 28, 423-437.

Babukiran B.V and Harish G. (2014). Influence of Resin and thickness of Laminate on Flexural Properties of Laminated Composites. *International Journal of Engineering Science and Innovative Technology* (IJESIT) 3.

Bao X.Q, Dargent T, Grondel S, Paquet J.B, and Cattan E. (2011). Improved micromachining of all SU-8 3D structures for a biologically-inspired flying robot. Microelectronic Engineering, 88 (8), 2218-2224.

Boeing. (2000). Boeing Material Specification - Glass fabric reinforcements for laminated plastic products. Boeing

Boeing. (2003). Boeing Material Specification - Glass fabric preimpregnated epoxy resin low temperature curing. Boeing.

Boeing. (2004). Boeing Material Specification - Carbon fiber reinforcements, yarn and fabric (BMS 8-9J). Boeing.

Borrega M and Gibson L.J. (2015). Mechanics of balsa (Ochroma pyramidale) wood. Mechanics of Materials,84(5),75-90.

Bucalem M.L. (1997) Finite Element Analysis of Shell Structures. Archives of Computational Methods in Engineering. 4, 3-61.

Butler, Rhett. (2015). Biomimetics, technology that mimics nature. Retrieved from Mongabay website http://news.mongabay.com/2005/07/biomimetics-technology-that-mimcs-nature/

Chang-kwon, Kang WS.(2013). Scaling law and enhancement of lift generation of an insect-size hovering flexible wing. *Journal of The Royal Society Interface* 10:0361.

Charles Richter HL.(2011). Untethered hovering flapping flight of a 3D-printed mechanical insect. *Artificial Life*.17.73-86.

Ching Hsin Chang and Kuen Tsan Chen. (2009). Study on Nanomechanical Properties of Dragonfly Wing. Advanced Materials Research,79-82.1325-1328.

Combes S.A (2010). Encyclopedia of Aerospace Engineering. Materials, structure, and dynamics of insect wings as bioinspiration for MAVs. Department of Organismic and Evolutionary Biology, Harvard University, Cambridge, MA, USA: John Wiley & Sons.

Combes S.A. (2003a). Flexural stiffness in insect wings I. Scaling and the influence of wing venation. Journal of Experimental Biology, 206, 2979-2987.

Combes S.A. (2003b). Flexural stiffness in insect wings II. Spatial distribution and dynamic wing bending. Journal of Experimental Biology, 206, 2989-2997.

Combes S.A. (2003c). Into thin air: contributions of aerodynamic and inertial-elastic forces to wing bending in the hawkmoth Manduca sexta. Journal of Experimental Biology, 206, 2999-3006.

Cox A., Monopoli D., Goldfarb M., Garcia E. (1999, September) Development of piezoelectrically actuated micro-aerial vehicle. Paper presented at the SPIE Symposium on Microrobotics and Microassembly. 3834, 101–108.

Dalton R. (2002) High speed biomechanics: Caught on camera. *Nature*. 418.721–722.

D'Arcy Thompson (1961). On Growth and Form. Retrived from http://dx.doi.org/10.1017/CBO9781107325852

David Kumar MS, Mohite PM, Sudhir Kamle, (2014). Structural Dynamic Analysis of BioInspired Carbon Fiber/Polythene MAV Wings. Paper presented at the Recent Advances in Mechanical Engineering, 2014. India, IIT.

de Smith, Goodchild, and Longley P.A. (2007) Geospatial Analysis: A comprehensive Guide to Principles, Techniques and Software Tools. Retrieved from http://www.spatialanalysisonline.com/HTML/index.htm

Dickinson MH, Lighton JRB. (1995). Muscle efficiency and elastic storage in the flight motor of Drosophila. *Science.* 268. 87-89.

Draganfly Innovations Inc. (2015). An Introduction to Unmanned Aerial Vehicles. Retrieved from http://www.draganfly.com/news/2008/08/24/introduction-to-unmanned-aerial-vehicles-uavs/

Dumont E.R, I. R. Grosse, and Slater G.J. (2009). Requirements for comparing the performance of finite element models of biological structures. *Journal of Theoretical Biology*.256, 96-103.2009.

Ellington CP (1984a). The aerodynamics of insect flight. VI. Lift and power requirements. *Phil Trans Royal Society of London B*.305.145-181.

Ellington CP. (1984b). The aerodynamics of insect flight III. Kinematics. *Proc Royal Society of London B*. 305.41-78.

Ellington CP. (1985). Power and efficiency of insect flight muscle. *Journal of Experimental Biology*. 115.293-304.

Ellington CP. (1999). The novel aerodynamics of insect flight: application to micro-air vehicles. Journal of Experimental Biology.202.3439-3448.

Federal Aviation Administration. (2015). Unmanned Aircraft Systems. Retrieved from http:// www.faa.gov/uas/

Fenelon M.A.A., Furukawa T. Design of an Active Flapping Wing Mechanism and a Micro Aerial Vehicle Using a Rotary Actuator. (2009). Mechanism and Machine Theory 45 (2009): 137–46.

Forman. R.T.T. (1987). The ethics of isolation, the spread of disturbance. and landscape ecology. In: M.G. Turner (Editor). Landscape Heterogeneity and Disturbance. Springer-Verlag, New York. 2 13-229.

Francis EH Tay, van Kan JA, Watt F, Choong WO. (2001). A novel micro-machining method for the fabrication of thick-film SU-8 embedded micro-channels. Journal of Micromechanics and Microengineering.11.27-32.

Frolov YS. (1975). Measuring the shape of geographical penomena: A history of the issue. Soviet Geography Review and Translation. 16. 676-687.

Gardner, R.H., O'Neill, R.V., Turner, M.G. and Dale. V.H. (1989). Quantifying scale-dependent effects of animal movement with simple percolation models. Landscape Ecology. 3(2) 1l-227.

Gardner. R.H.. O'Neill. R.V. and Turner, M.G. (1993). Ecological implications of landscape fragmentation. In: S.T.4. Pickett and M.J. McDonnell (Editors), Humans as Components of Ecosystems: Subtle Human Effects and the Ecology of Populated

Areas. Springer-Vcrlag. New York. 208-226.

Gorman J. (2003, June) What really happens when fruit flies fly? The New York Times.

Grodnitsky DL. (1999). Form and function of insec twings: the evolution of biological structures. John Hopkins University Press. Baltimore.

Gui, L., Fink, T., Cao, Z., Sun, D., Seiner, J. M., & Streett, D. A. (2010). Fire Ant Alate Wing Motion Data and Numerical Reconstruction. Journal of Insect Science, 10, 19. http://doi.org/10.1673/031.010.1901.

Gustafson, E.J. and Parker, G.R., (1992). Relationship between landcover proportion and indices of landscape spatial pattern. Landscape Ecology. 7: 101-I 10.

Gustafson, E.J., Parker, G.R. and Backs, SE. (1994). Evaluating spatial pattern of wildlife habitat: a case study of the WildTurkey (Meleagrisgallopa~o). Am. Midl. Nat. 131. 4-33.

Harris. L. (1984). The Fragmented Forest: Island-biogeography Theory and the Preservation of Biotic Diversity. University of Chicago Press, Chicago, 211.

Herbert PGY R.C, Smith C.W, Wooton R.J, Evans K.E. (2000) The hindwing of the desert locust (Schistocerca Gregaria Forskal): Finite Element Analysis of a Deployable Structure. Journal of Experimental Biology. 203, 2945-2955.

Hisayoshi Naka YS, Hiromu Hashimoto.(2014, August 31 - September 3). Development of the Artificial Wing Suitable for Flapping Micro Air Vehicle Based on Dragonfly Wing. Paper presented at International Conference on Design Engineering and Science, ICDES 2014, Pilsen, Czech Republic, Tokai University.

HuaiHui Ren, Xishu W, XuDong L, Ying Long C. (2013) Effects of dragonfly wing structure on the dynamic performances. Journal of Bionic Engineering, 10, 28-38.

HuaiHui Ren, Xishu W, Ying Long C, Xu Dong L. (2012). Biomechanical behaviours of dragonfly wings: Relationship between configuration and deformation. Chinese

Physics B. (21).

Hwan Ko, Kim, J. Hong, Y.Yoo, Y. Lee, T.Lie Jin, H. Cheol Park, N. Seo Goo, D. Byun. (2012). Micro/nanofabrication for a realistic beetle wing with a superhydrophobic surface, Bioinspiration and Biomimetics, 7(1), 1748-3190

Jane Wang Z. (2004). The role of drag in insect hovering. Journal of Experimental Biology.207(23). 4147-4155.

Jerzy Lewitowicz G.K, Krzysztof Sibilski, Josef Zurek. (2008). Modeling and simulation of flapping wings micro-aerial vehicles flight dynamics. Paper presented at the International Congress of the Aeronautical Sciences. Alaska, USA.

Jianyang Z, Chaoying Z, Chao W, Lin J. (2014). Effect of flexibility on flapping wing characteristics under forward flight. Fluid Dynamics Research. 46(5), 055515.

Jiyu Sun and Bharath Bushan. (2012).The structure and mechanical properties of dragonfly wings and their role on flyability. Comptes Rendus Mecanique, 340, 3-17.

Jongerius S.R and Lentink D. (2010). Structural Analysis of a Dragonfly Wing Experimental Mechanics (50). 1323-1334.

Joong-Yeon Cho G.K, Sungwook Kim, Heon Lee.(2013).Replication of surface nano-structure of the wing of dragonfly (Pantala Flavescens) using nano-molding and UV nanoimprint lithography. Electronic Materials Letter. 9, 523-526.

Julian F.V Vincent, Olga A Bogatyreva, Nikolaj R Bogatyrev, Adrian Bowyer, Anja Karina Pahl, S. (2006). Biomimetics: its practice and theory. The Royal Society, 3(9), 1742-5662.

Knaapen. J.P., Scheffer. M. and Harms. B., (1992). Estimating habitat isolation in landscape planning. Landscape Urban Plann., 23: l-16.

Krohne. D.T.. Dubbs. B.A. and Baccus, R. (1984). An analysis of dispersal in an unmanipulated population of Peromyscus leucopus. Am. Midl. Nat., 112. 146-156.

Kutsch, W., Martz, H. and Gäde, G. (2002), Flight capability and flight motor pattern in a sedentary South African grasshopper, Phymateus morbillosus– a comparison with migratory species. Physiological Entomology, 27: 39–50. doi: 10.1046/j.1365-3032.2002.00267.x

Kyriakides S, Arseculeratne R, Perry E.J, Liechti K.M. (1995). On the compressive failure of fiber reinforced composites. International Journal of Solid Structures. 32. 685-738.

Leban M.B and Tisu R. (2013) The effect of TiN inclusions and deformation-induced martensite on the corrosion properties of AISI 321 stainless steel. Engineering Failure Analysis. 33(10),430-438.

Lehman F-O, Sane SP, Dickinson MH (2005). The aerodynamic effects of wing-wing interaction in flapping insect wings. Journal of Experimental Biology. 208.2075-3092.

Lillesand. T.M. and Kiefer. R.W., (1987). Remote Sensing and Image Interpretation. Wiley, New York, 721.

Lingxiao Zheng TL, Hedrick, Rajat Mittal.(2013). Time-varying wing twist improves aerodynamic efficiency of forward flight in butterflies. PLOS ONE. 8(1).005306

Lord. J.M. and Norton, D.A., 1990. Scale and the spatial concept of fragmentation. Conserv. Biol., 4. 197-202.

Luo H, Tian, Fangbao, Song, Jialei, Lu, Xi-Yun. (2012). Aerodynamic cause of the asymmetric wing deformation of insect wings. APS Division of Fluid Dynamics E32.003.

Luttges MW. 1989. Accomplished insect fliers. In: Gad-el –Hak M (ed). Frontiers in experimental fluid mechanics, Lecture noted in Engineering, Springer, Berlin, 429-456.

Marcin Luczak, S.M., Bart Peeters, Kim Branner, Peter Berring, Maciej Kahsin. (2011). Dynamic Investigation of Twist-Bend Coupling in a Wind Turbine Blade. Theoretical And Applied Mechanics (49). 765-789.

Maria Mingallon S.R. (2011).The Architecture of the Dragonfly Wing: A Study of the Structural and Fluid Dynamic Capabilities of the Anisoptera's Forewing. Paper presented at the International Mechanical Engineering Congress & Exposition, Denver, Colorado, USA.

Maybury WJ, Lehmann F.O. (2004). The fluid dynamics of flight control by kinematic phase lag variation between two robotic insect wings. Journal of Experimental Biology. 207.4707-4726.

McDonald M, Agrawal Sunil K. (2010). Design of a Bio-Inspired Spherical Four-Bar Mechanism for Flapping-Wing Micro Air-Vehicle Applications. Journal of Mechanisms and Robotics. 021012.

McMichael J.M. and Francis, M. (1997, July). Micro Air Vehicles-Towards a new dimension in flight. Federation of American Scientists. Retrieved from http://www.fas.org/irp/program/collect/docs/mav_auvsi.htm

Michelson, R.C. and Reece, S., (1998) March. Update on flapping wing micro air vehicle research-ongoing work to develop a flapping wing, crawling entomopter. In 13th Bristol International RPV/UAV Systems Conference Proceedings, Bristol England (Vol. 30, pp. 30-1).

Miller LA, Peskin CS. (2004). When vortices stick: an aerodynamic transition in tiny insect flight. Journal of Experimental Biology. 207. 3073-3088.

Mountcastle AM. (2009). Aerodynamic and functional consequences of wing compliance. Journal of Experimental Fluids. 46, 873-82.

Newman et al. (1986). An approach to the mechanics of pleating in dragonfly wings. Journal of Experimental Biology. 125, 361-72.

Ngoc San Ha and Nam Seo Goo. (2013 January). Flapping frequency and resonant frequency of insect wings. Paper presented at the 10th International Conference on Ubiquitous Robots and Ambient Intelligence (URAI), Konkuk University.

doi:10.1109/URAI.2013.6677463

Nguyen QV, Park H, Byun D, Goo N. (2010, September 19-23). Recent progress in developing a beetle-mimicking flapping-wing system. Paper presented at the World Automation Congress 2010, Kobe. US, IEEE.

Noms S (2001). Taking Flight. Oxford Today.14(1)

Norberg RA (1975). Hovering flight of the dragonfly Aeschna juncea. Wu TY-T,Brokaw CJ, Brennen C (eds) Kinematics and Aerodynamics.2 Plenum Press, New York. 763-781

Osei-Antwi M, J. de Castro, Vassilopoulos A.P, and Keller T. (2013). Shear mechanical characterization of balsa wood as core material of composite sandwich panels. Construction and Building Materials. 41(4). 231-238.

Osei-Antwi M, J. de Castro, Vassilopoulos A.P, and Keller T. (2014). Fracture in complex balsa cores of fiber-reinforced polymer sandwich structures. Construction and Building Materials. 71,194-201.

Rahman. (2012). Assessment of Bridge Service Life using Wireless Sensor Network. Youngstown State University, Department of Graduate Studies and Research.

Rajabi M.M.H and Darvizeh A. (2011). Investigation of microstructure, natural frequencies and vibration modes of dragonfly wing. Journal of Bionic Engineering. 8. 165-173.

Reavis MA, Luttges MW. (1988). Aerodynamic forces produced by a dragonfly. AIAA J. 88-0330. 1-13

Rieger N.F. (1999). The Relationship Between Finite Element Analysis and Modal Analysis. Stress Technology Incorporated. Retrieved from http://www.sti-tech.com/dl/feapaper.pdf

Rose E. Hutchins (n.d). Insects. Retrieved from Scholastic website http://teacher.scholastic.com/activities/explorations/bug/libraryarticle.asp?ItemID=1

12&SubjectID=110&categoryID=4

Rubentheren V, T. A. Ward, C. Y. Chee, and C. K. Tang. (2015). Processing and analysis of chitosan nanocomposites reinforced with chitin whiskers and tannic acid as a crosslinker. Carbohydrate Polymers.115.379-387.

Rupan Talucdher and Kunigal Shivakumar. (2013). Tensile Properties of Veins of Damselfly Wing. Journal of Biomaterials and Nanobiotechnology. 4. 247-255.

Rüppell G (1989). Kinematic analysis of symmetrical flight manoeuvres of Odonata. Journal of Experimental Biology. 144.13-42

Saharon D, Luttges MW. (1987). Three dimensional flow produced by a ptiching-plunging model dragonfly wing. AIAA J. 87-0121. 1-17

Shang J.K, Combes S, Finio B.M, Wood R.J. (2009). Artificial insect wings of diverse morphology for flapping-wing micro air vehicles. Bioinspiration and Biomimetics, 4(3), 1748-3190.

Shyy W, Aono H, Chimakurthi S.K, Trizila P, Kang C.K, Cesnik, et al. (2010) Recent progress in flapping wing aerodynamics and aeroelasticity. Progress in Aerospace Sciences,46, 284-327.

Shyy W., Berg M., Ljungqvist D. (1999). Flapping and flexible wings for biological and micro air vehicles. Progress in Aerospace Sciences. 35. 455–505.

Smithsonian Institution (2010). Bug Info: Insect Flight. Encyclopedia Smithsonian Online Retrieved from http://www.si.edu/Encyclopedia_SI/nmnh/buginfo/insflght.htm

Sudo S, Tsuyuki K, Ito Y, Tani J. (2001) The wing apparatus and flapping behavior of hymenoptera. JSME International Journal, Series C. 44. 1103–1110.

Sudo S, Tsuyuki K, Kanno K. (2005). Wing characteristics and flapping behavior of flying Insects.Experimental Mechanics. 45.550–555.

Sun M, Tang J (2002). Unsteady aerodynamics force generation by a model fruit fly wing flapping motion. Journal of Experimental Biology. 205. 55-70.

Tamilarasan, Uthirapathy, Karunamoorthy, Loganathan, & Palanikumar, Kayaroganam. (2015). Mechanical Properties Evaluation of the Carbon Fibre Reinforced Aluminium Sandwich Composites. Materials Research, 18(5), 1029-1037.https://dx.doi.org/10.1590/1516-1439.017215

Tanaka H. and Wood R.J. (2010). Fabrication of corrugated artificial insect wings using laser micromachined molds. Journal of Micromechanics and Microengineering. 20075008.

The UAV. (2015). The UAV. Retrieved from http://www.theuav.com/#31

Tobalske B.W. (2000). Physiology and Biomechanics of Gait Selection in Flying Birds. Physiol Biochem Zoology. 73(6):736–750.

Tobalske B.W., Dial K.P. (1996). Flight kinematics of Black-billed Magpies and pigeons over a wide range of speeds. Journal of Experimental Biology. 99: 263–280.

Tu Delft University of Technology. (2013). Robot Dragonfly DelFly Explorer avoids obstacles by itself. Retrieved from http://www. tudelft.nl/en/current/latestnews/article/detail/robotlibelle-delfly-explorer-ontwijkt-zelf-obstakels/

Usherwood JR, Ellington CP. (2002). The aerodynamics of revolving wings I. Model hawkmoth wings. Journal of Experimental Biology. 205. 1547-1564.

Vanderberghe N, Zhang J, Childress S. (2004). Symmetry breaking leads to forward flapping flight. Journal of Fluid Mechanics. 506.147-155.

Vogel S. (2013) Comparative Biomechanics: Life's Physical World (2nd Edition). Princeton University Press.

Wakeling J.M and Ellington C.P. (1997). Dragonfly Flight: Velocities, Accelerations and

Kinematics of Flapping Flights. Journal of Experimental Biology.200, (3) 557-582.

Ward, T. A., Rezadad, M., Fearday, C. J., & Viyapuri, R. (2015). A Review of Biomimetic Air Vehicle Research: 1984-2014. International Journal of Micro Air Vehicles, 7(3), 375-394.

Warren A.D, Harniman R.L, Collins A.M, Davis S.A, Younes C.M, Flewitt P.E.J, et al. (2015). Comparison between magnetic force microscopy and electron back-scatter diffraction for ferrite quantification in Type 321 stainless steel. Ultramicroscopy, 148 (1), 1-9.

Weis-Fogh T (1972). Energetics of hovering flight in hummingbirds and Drosophila. Journal of Experimental Biology. 56.79-104.

Wootton RJ.(1981). Support and deformability in insect wings. Journal of Zoology 193:447-68.

Wootton RJ.(1993) Leading edge section and asymmetric twisting in the wings of flying butterflies (Insecta Papilionoidea). Journal of Experimental Biology. 180. 105-17.

Xinyan Deng and Zheng Hu. (2008). Wing-wing interactions in dragonfly flight. The Neuromorphic Engineer. 10.2417/1200811.1269.

Xue Li Z, W. Shen, G. Shu Tong, Jia-meng T, Loc VQ. (2009). On the vein stiffening membrane structure of a dragonfly hindwing. Journal of Zheijang University. 10, 72-81.

Yang W Q, Song W P. (2012). The effects of span-wise and chord-wise flexibility on the aerodynamic performance of micro flapping-wing. Chinese Science Bulletin. 57. 2887-97.

Yirka, Bob. (2013, April) Festo builds BionicOpter-fully functional robot dragonfly. Phys.Org. Retrieved from http://phys.org/news/2013-04-festo-bionicopterfully-functional-robot-dragonfly.html

Young J WS, Bomphrey RJ, Taylor GK, Thomas ALR. (2009). Details of insect wing design and deformation enhance aerodynamic function and flight efficiency.

Science 325, 1549–52.

Zhao L, Huang Q, Deng X, Sane SP.(2009). Aerodynamic effects of flexibility in flapping wings. Journal of The Royal Society Interface. 12(113)1742-5662.

Zheng Hu and Xinyan Deng (2009). A Flight Strategy for Intelligent Aerial Vehicles Learned from Dragonfly, Aerial Vehicles, Retrieved from: http://www.intechopen.com/books/aerial_vehicles/a_flight_strategy_for_intelligent_aerial_vehicles_learned_from_dragonfly.

LIST OF PUBLICATIONS

Journal articles

[1] Praveena N. Sivasankaran, Thomas A. Ward (2015). Spatial network analysis to construct simplified wing structural models for Biomimetic Micro Air Vehicles. *Aerospace Science and Technology*.(Q1 Journal:1.000 IF)

[2] Nair, P., Ward, T., Rubentheren, V., Mohd Rafie J. (2015). Static Strength Analysis of Dragonfly Inspired wing for Biomimetic Micro Air Vehicles. *Chinese Journal of Aeronautics.* (Accepted for publication) (Q1 Journal:1.070 IF)

[3] Praveena N. Sivasankaran, Thomas A. Ward, Erfan Salami, Rubentheren Viyapuri, Christopher Fearday. (2015). An experimental study of the aeroelastic properties of dragonfly-like flapping wings for use in Biomimetic Micro Air Vehicles (BMAV). *Chinese Journal of Aeronautics* (Accepted for publication) (Q1 Journal: 1.070 IF)

[4] Rubentheren, V., Ward, T. A., Chee, C. Y., & Tang, C. K. (2015). Processing and analysis of chitosan nanocomposites reinforced with chitin whiskers and tannic acid as a crosslinker. *Carbohydrate Polymers*, *115*, 379-387. (Q1 Journal: 4.074 IF)

[5] Rubentheren, V., Ward, T., Chee, C., & Nair, P. (2015). Physical and chemical reinforcement of chitosan film using nanocrystalline cellulose and tannic acid. *Cellulose, 22(4),* 2529-2541. (Q1 Journal:3.573 IF)

[6] Rubentheren, V., Ward, T., Chee, C., Nair, P., Salami, E., & Fearday, C. (2015). Effects of heat treatment on chitosan nanocomposite film reinforced with nanocrystalline cellulose and tannic acid. *Carbohydrate Polymers.* (Accepted with minor revision) (Q1 Journal: 4.074 IF)

Conferences

[1] Nair, P., Ward, T., Rubentheren, V., Johan, M., R. (2015). Experimental analysis of artificial dragonfly wings using black graphite and fibreglass for use in Biomimetic Micro Air Vehicles (BMAV). *MATEC Web of Conferences 30,03001*.

[2] Rubentheren, V., Ward, T., Chee, C., Nair, P., Erfan, S., (2015). Development of heat treated chitosan nano-composite film for the wing membrane of biomimetic micro air vehicle (BMAV). *European conference on organized film ECOF 14*.

APPENDICES

Appendix A: High speed camera images of PLA wing frame models

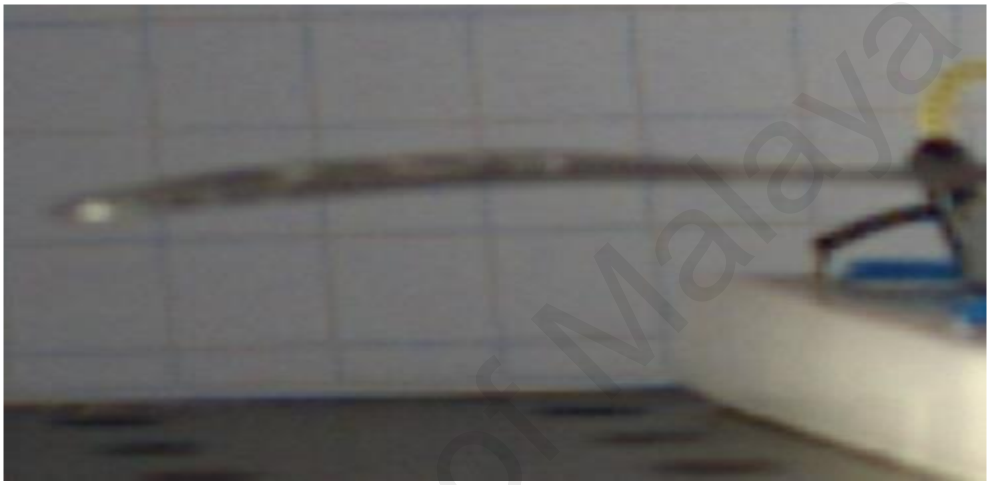

(a) Side view of PLA wing frame

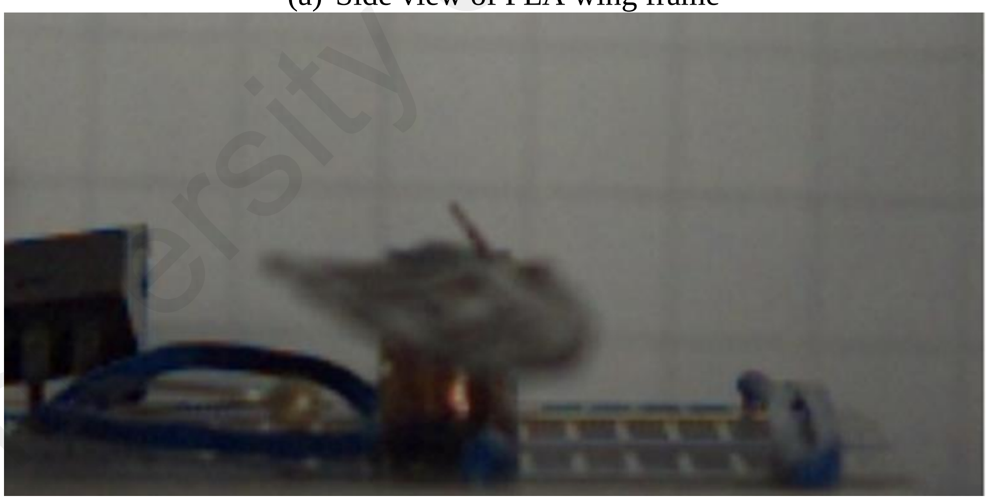

(b) Front view of PLA wing frame

Appendix B: High speed camera images of acrylic wing frame models

(a) Side view of acrylic wing frame

(b) Front view of acrylic wing frame

Appendix C: High speed camera images of ABS wing frame models

(a) Side view of ABS wing frame

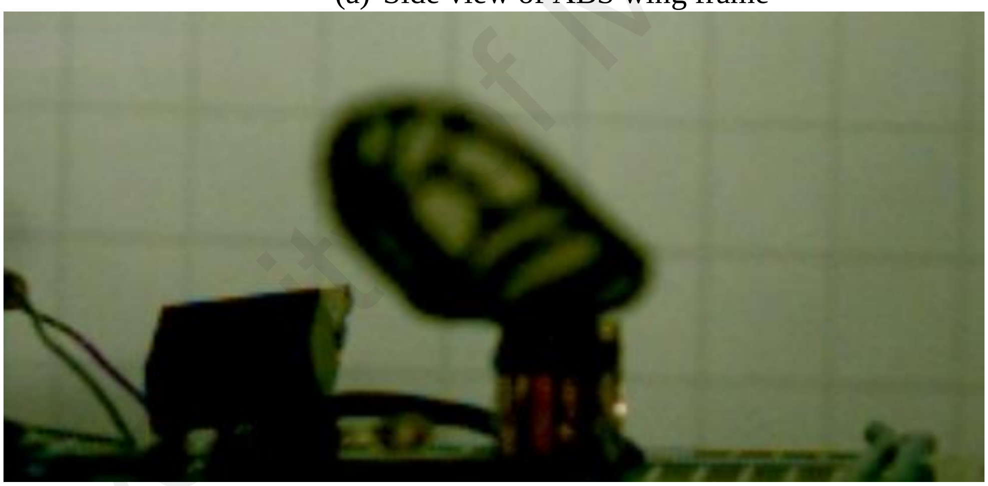

(b) Front view of ABS wing frame